Univeristeit van Amsterdam
Technische Universität München

# A Precision Optical Calibration Module for IceCube-Gen2

*Author:*
Joost Pieter VEENKAMP

*Supervisors:*
Prof. Patrick DECOWSKI
Prof. Elisa RESCONI
Dr. Dorothea SAMTLEBEN

GRAVITATION AND ASTROPARTICLE PHYSICS AMSTERDAM

MASTER THESIS

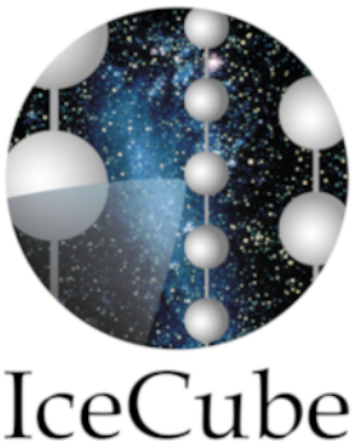


January 7, 2016

Master of Science

**A Precision Optical Calibration Module for IceCube-Gen2**

# *Abstract*

by Joost Pieter VEENKAMP

IceCube is a cubic kilometer neutrino detector in the Antarctic ice. With the detection of high energy neutrinos many scientific goals are being pursued. The Precision IceCube Next Generation Upgrade, with an energy threshold of a few GeV, will detect atmospheric neutrinos with high statistics. With this detector, the Neutrino Mass hierarchy can be determined, among other goals. Building on experience gathered with the successful IceCube detector, improvements are made to all elements of the PINGU design with respect to IceCube. Among these is the calibration system, in which the Precision Optical CAlibration Module (POCAM) will be implemented. The POCAM illuminates all PINGU optical modules isotropically with short pulses of light. This enables verification of the energy scale and energy resolution of PINGU, and enhancement of the ice models. To introduce the POCAM, this thesis starts with a discussion of (atmospheric) neutrino physics, the IceCube and PINGU detectors and the respective calibration systems, after which the design study of the POCAM is discussed. An inverted integrating sphere isotropizes photons emitted from an internal, appropriately placed matrix of LEDs. The resulting emission from the POCAM consist of short, isotropic light pulses. A diode on the integrating sphere enables in-situ monitoring of the emission. The emission characteristics have been optimized by studying the geometry in a Geant4 simulation. Simulations of configurations varying the properties in the design are presented. With the acquired knowledge a baseline geometry is proposed. As a next step the functionality of the POCAM inside PINGU and IceCube is tested with ray tracing simulation, of which the first promising results are discussed.

# Contents

# List of Figures

# Introduction

Since the proposal of the neutrino, to conserve energy momentum and spin in $\beta$-decay, by Wolfgang Pauli in 1930, a large amount of knowledge has been gathered on neutrinos. One of the recent developments in the field of neutrino physics is the discovery that neutrinos are massive and mixed. The neutrino mass, and many aspects of their mixing, are as yet unknown. The scientific pursue of understanding neutrinos is a difficult task that pushes physics forwards on multiple fronts.

Standard Model (SM) as a $SU(3) \times SU(2) \times U(1)$ gauge theory has been a functional theoretical framework, but appears to be incomplete. In this framework neutrinos, for a number of reasons, do not have mass. Therefore, the discovery of neutrino mass and mixing is a first discovery of beyond the standard model physics. Apart from the SM, neutrino research is connected to many open questions in cosmology. Neutrinos could, for example, offer insight in the nature of Dark Matter, probe early universe theories, and explain high energy cosmic rays.

IceCube is the first cubic kilometre neutrino detector, with optical modules covering a cubic kilometre of antarctic ice at depths of $1500\,\mathrm{m}$ to $2500\,\mathrm{m}$. The mainvolume of IceCube, with an energy threshold of $100\,\mathrm{GeV}$ detects high energy neutrinos. With the dense infill array DeepCore, IceCubes threshold energy is pushed down to $10\,\mathrm{GeV}$. With this energy range, atmospheric neutrinos can be studied. IceTop, on the surface of IceCube, is a cosmic ray detector. IceCube is, therefore, a multi-purpose detector. A further extension of IceCube is planned, called IceCube-Gen2. This extension consists of the Precision IceCube Next Generation Upgrade (PINGU) and the High Energy Array (HEX), pushing the energy threshold to a few GeV and increasing the sensitivity to high energy neutrinos, respectively.

With its low energy threshold, PINGU is intended to detect atmospheric neutrinos. Since the flux of atmospheric neutrinos is large and constant, PINGU is predicted to determine the nature of the Neutrino Mass hierarchy to $5\,\sigma$ within 5 years of deployment. To lower the energy threshold with PINGU, a volume of ice is instrumented more densely. Apart from the density of instrumentation, the precision of the detectors precision is improved with improved instrumentation. This thesis presents such an improvement, the Precision Optical Calibration Module (POCAM). This module is intended to illuminate PINGU with isotropic, short light pulses. With this addition to the calibration systematics, the precision of PINGU could be enhanced by, for example, verifying the energy scale, measuring the energy resolution and testing ice models.

This study starts by introducing the relevant basis of neutrino physics in chapter 1. This includes some standard model physics and a short introduction in neutrino oscillation and the neutrino mass hierarchy (NMH).

Chapter 2 introduces atmospheric neutrinos. The focus is on properties that are relevant for the PINGU detector, such as the atmospheric neutrino flux and the oscillation of atmospheric neutrinos.

Chapter 3 explains the detection of neutrinos with the IceCube detector. The important hardware is explained. A special focus is on the calibration hardware and techniques in IceCube, since this is of importance for the POCAM design. This, to some extent detailed, introduction in IceCube is needed to properly introduce PINGU.

In Chapter 4 the current design for PINGU is discussed. The focus is on the improvements with respect to IceCube.

Chapter 5 introduces the design study of the POCAM. It covers an explanation of the initial design, a introduction in the dedicated Geant4 simulation and an introduction to the IceCube photon tracking simulation in which the Geant4 simulation is implemented.

Chapter 6 presents the results, where the simulation efforts and resulting design optimizations are explained in detail.

Chapter 7 comprises a summary and a discussion of the results. To conclude, a current baseline design is presented and discussed. Future improvements and next steps in the ongoing design and prototyping study are given in the outlook.

# Chapter 1

# Neutrino Physics

As to introduce IceCube, IceCube-Gen2 and the design study of the POCAM, a description of the relevant theory is necessary. This chapter on neutrino theory commences with a description of the Standard Model neutrino theory. Followed by an introduction to neutrino oscillation and neutrino mass. The chapter finishes with the effects of matter on neutrino oscillations.

## 1.1 Neutrino Theory

#### Neutrinos in the Standard Model

The Standard Model of particle physics consists of three knwon generations of fermions, five gauge bosons corresponding to the fundamental interactions and the Higgs field. The Standard Model is mathematically described by the gauge group

$$G_{SM} = SU(3)_C \times SU(2)_L \times U(1)_Y. \tag{1.1}$$

Each generation in this Standard Model description consists of 2 quarks and 2 leptons, as shown in figure 1.1. Of the two leptons in each family, one carries electric charge $(e^{\pm}, \mu^{\pm}, \tau^{\pm})$ and the other is the corresponding neutrino $(\nu_e, \nu_\mu, \nu_\tau)$.

Neutrinos, unlike the other leptons, carry neither electromagnetic nor color charge. Therefore, neutrinos only interact with other matter through weak interactions. Weak interactions can be via the Neutral or charged currents (NC, CC), which are mediated by the $Z^0$ and $W^{\pm}$ bosons respectively. The $W^{\pm}$ and $Z^0$ bosons are massive, with $m_{Z_0}$=91.1876(21) $\mathrm{GeV/c^2}$ and $m_{W^{\pm}}$=80.385(15) $\mathrm{GeV/c^2}$) [63], resulting in suppression of the interaction. Figure 1.2 shows Feynman diagrams of the CC and NC interactions of neutrinos. A more elaborate description of neutrino interaction in the context of detection techniques follows in section 3.1.1.

The part of the Standard Model Lagrangian describing the weak charged current between neutrinos and corresponding charged leptons $(\alpha = e, \mu, \tau)$ is given by

$$-\mathcal{L}_{CC} = \frac{g}{2\sqrt{2}} \sum_{\alpha} \left[ W_\mu^+ \bar{\nu}_\alpha \gamma^\mu (1-\gamma^5) \ell_\alpha^- + W_\mu^- \ell_\alpha^+ \gamma^\mu (1-\gamma^5) \nu_\alpha \right] \tag{1.2}$$

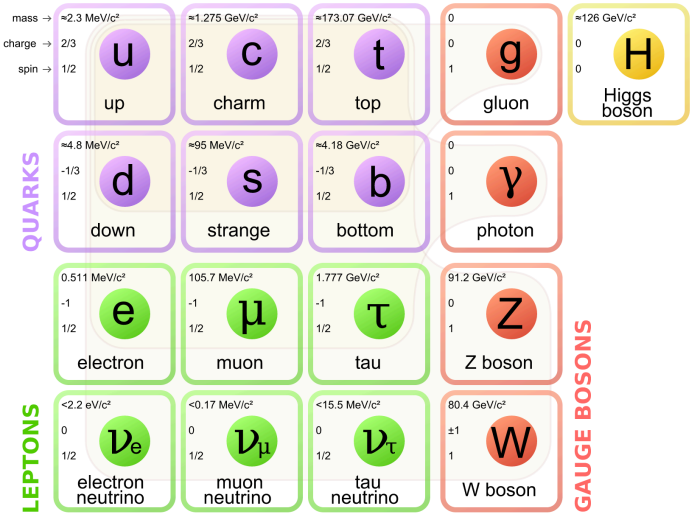


**Figure 1.1:** *A depiction of the fundamental particles in the standard model. The particles can be divided in the categories quarks (purple), leptons (green) and gauge bosons (red). Additionally, the mass charge and spin of each particle is listed. Figure taken from [68].*

The neutral current Lagrangian is

$$-\mathcal{L}_{NC} = \frac{g}{2\cos(\theta_W)} \sum_{\alpha} \bar{\nu}_\alpha \gamma^\mu (g_V - g_A \gamma^5) \nu_\alpha Z^0_\mu \tag{1.3}$$

Here, $g$ is the coupling constant and $\gamma^\mu$ are the gamma matrices and $\gamma^5 = \gamma^0\gamma^1\gamma^2\gamma^3\gamma^4$. The Einstein summation convention is applied with $(\mu = 0, 1, 2, 3)$ and metric $\eta = (1, -1, -1, -1)$.

From equation (1.2) it is evident that, in the Standard Model, CC interactions only occur with neutrinos with left handed chirality $\nu_{\ell L} = P_L \nu_l$ and, naturally, right handed antineutrinos $\bar{\nu}_{\ell R} = \bar{\nu}_\ell P_L$, with the left-handed projection opertator $P_L = \frac{1-\gamma^5}{2}$. From equation (1.3) it is clear that neutral current interaction does occur with right handed neutrinos . However, an interaction of right handed neutrinos has never been observed [63].

Every massive particle can be both left handed or right handed, since a Lorentz boost of the frame of reference can always reverse the direction of momentum, changing the chirality with it. This does not hold for massless particles though, since right handed neutrinos have never been observed, neutrinos were assumed to be massless and move at the speed of light $c$ [38].

However, neutrino mixing has been observed [14], implying that neutrinos do have a mass. However, the way to add a neutrino mass term to the SM is yet to be defined. This question is directly related to whether neutrinos are $Dirac$ or $Majorana$ particles.

The Dirac equation describes the evolution of a Dirac particle and its anti-particle [38]. This is the theoretically simplest solution in which the neutrinos have a Dirac mass, just like the other leptons in the SM [54]. If the neutrino is a majorana particle however, it is its own anti-particle [60].

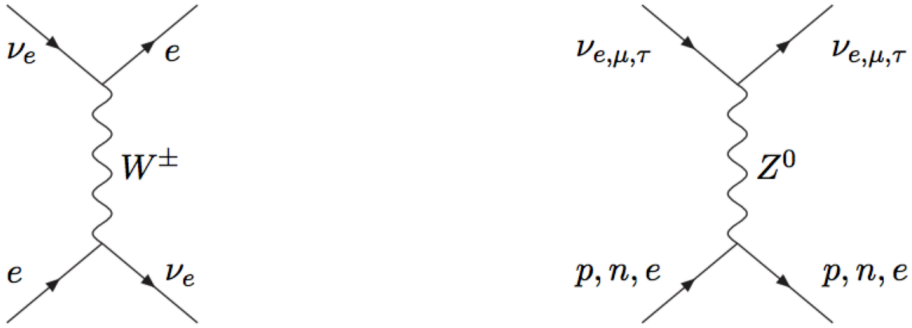


**Figure 1.2:** *Diagrams of the known neutrino interactions. CC interaction between electron neutrinos and electrons (left) and NC interaction between neutrinos and electrons or nucleons (right).*

There are several theoretical explanations possible for either Majorana or Dirac neutrino mass. These include the See-saw mechanisms [34], R-parity [64], TeV scale loop mechanisms [59], extra dimensions [20] and string theory [62]. Discussions of these theoretical descriptions are not in the scope of this thesis. Here, the focus will be on the theory most relevant for PINGU, the low energy extension of IceCube, which will target the nature of the NMH by measuring the oscillations of atmospheric neutrinos.

### 1.1.1 Neutrino Oscillation in Vacuum

Recently, the nobel prize has been awarded to the researches that proofed that neutrinos oscillate, and have nonzero mass [14]. Apart from the theory being well in agreement with current measured neutrino fluxes, recently direct appearance of an oscillating neutrino has been observed [66].

In this theory of neutrino oscillations, a neutrino of a certain flavor state $\nu_\alpha$ , with $\alpha = e, \mu, \tau$, is a linear combination of mass eigenstates $\nu_k$ $(k = 1, 2, 3)$. In this section the description is limited to 3 mass eigenstates, when sterile neutrinos are incorporated more eigenstates $k$ are possible.

$$|\nu_\alpha\rangle = \sum_k U^*_{\alpha k} |\nu_k\rangle \tag{1.4}$$

In the case of 3 mass eigenstates, unitary matrix U is the Pontecorvo-Maki-Nakagawa-Sakata (PMNS) leptonic mixing matrix. With three mixing angles, $\theta_{12}$, $\theta_{23}$ and $\theta_{13}$ and with the CP violating phase $\delta$, the PMNS matrix is most commonly defined as:

$$U^* = \begin{pmatrix} c_{12}c_{13} & c_{13}c_{12} & s_{13}e^{-i\delta} \\ -s_{12}c_{23} - c_{12}s_{13}s_{23}e^{i\delta} & c_{12}c_{23} - s_{13}s_{23}e^{i\delta} & c_{13}s_{23} \\ s_{12}s_{23} - c_{12}s_{23}s_{13}e^{i\delta} & s_{12}c_{23} - s_{12}s_{13}c_{23}e^{i\delta} & c_{13}c_{23} \end{pmatrix} \tag{1.5}$$

Here, $s_{ij} = \sin(\theta_{ij})$, $c_{ij} = \cos(\theta_{ij})$, with $\theta_{ij}$ the mixing angles relating states $i$ and $j$, plus a possible complex phase $\delta$.

The probability for a neutrino to oscillate from one flavor state to another is defined by this mixing matrix. Although a complete derivation of the transition probability requires Quantum Field Theory and needs to take into account dispersion relations $E(p)$, the results of the following ansatz is the same and found to be very illustrative. Therefore, it is comactly derived here.

### Oscillation Probability

The neutrinomass eigenstates $|\nu_k\rangle$ are eigenstates of the hamiltonian $H|\nu_k\rangle = E_k|\nu_k\rangle$. Here, the energy eigenvalues are

$$E_k = \sqrt{\vec{p}^2 + m_k^2}. \tag{1.6}$$

Consequently, the Schrödinger equation

$$i\frac{d}{dt}|\nu_k(t)\rangle = H|\nu_k(t)\rangle \tag{1.7}$$

implies that massive neutrino states propagate as plane waves in the mass eigenstates $|\nu_k\rangle$

$$|\nu_k(t)\rangle = e^{-iE_k t}|\nu_k\rangle. \tag{1.8}$$

Combining (1.4) and (1.8) results in a description of a neutrino in a definite flavor state at time $t$.

Using the unitarity of $U$ we can express the mass states as a linear combination of the flavor states by inverting (1.4)

$$|\nu_k\rangle = \sum_\alpha U_{\alpha k}^* |\nu_\alpha\rangle \tag{1.9}$$

combining (1.9) and (1.8) the flavor state $|\nu_\alpha\rangle$ can thus be expressed as a superposition of different flavor states

$$|\nu_\alpha(t)\rangle = \sum_\beta \left( \sum_k U_{\alpha k}^* e^{-iE_k t} U_{\beta k} \right) |\nu_\beta\rangle \tag{1.10}$$

In a mixed state, i.e. $t > 0$, the coefficient of $|\nu_\beta\rangle$ is the amplitude of $\nu_\alpha \to \nu_\beta$ transitions as a function of time. Squaring this amplitude gives us the probability of transition

$$P_{\nu_\alpha \to \nu_\beta}(t) = |A_{\nu_\alpha \to \nu_\beta}(t)|^2 = |\langle \nu_\beta | \nu_\alpha(t)\rangle|^2 = \sum_{k,j} U_{\alpha k}^* U_{\beta k} U_{\alpha j} U_{\beta j}^* e^{-i(E_k - E_j)t}. \tag{1.11}$$

Approximating $E_k - E_j \simeq \frac{\Delta m_{kj}^2}{2E}$ where $\Delta m_{kj}^2 \equiv m_k^2 - m_j^2 \ll E^2$, and rewriting the time component $t$ to a length component L which is the distance from the neutrino source

and the detector, i.e. $L = t$ for ultrarelativistic neutrinos, we get an expression for the oscillation probability

$$P_{\nu_\alpha \to \nu_\beta}(L, E) = \sum_{k,j} U^*_{\alpha k} U_{\beta k} U_{\alpha j} U^*_{\beta j} e^{\phi_{kj}}, \tag{1.12}$$

$$\tag{1.13}$$

with

$$\phi_{kj} = \left( -i \frac{\Delta m^2_{kj} L}{2E} \right). \tag{1.14}$$

This expression and its derivation show how neutrino experiments can prove the theory of neutrino oscillation. By measuring L and E in oscillation experiments it is possible to determine the squared mass differences $m^2_{kj}$ and the mixing angles. A more detailed derivation of (1.12) can be found in [38].

### Two Flavor Case Approximation

This same framework can be approximated to two flavor states. The two flavor oscillation probability here, as to describe matter effects in section 1.1.2. Furthermore, it strongly simplifies the interpretation of some oscillation properties.

$$|\nu_\alpha\rangle = \begin{pmatrix} \nu_e \\ \nu_\mu \end{pmatrix} \tag{1.15}$$

PMNS matrix $U_{2\nu}$ is defined with only one mixing angle $\theta$. $U$ is therefore orthogonal. The relation between flavor and mass neutrino eigenstates in the two flavor approximation can be described by

$$|\nu_\alpha\rangle = U|\nu_m\rangle, \tag{1.16}$$

where $\alpha = (e,\, \mu)$ and $m = (1, 2)$.

Mixing matrix $U$ is

$$U = \begin{pmatrix} \cos(\theta) & \sin(\theta) \\ -\sin(\theta) & \cos(\theta) \end{pmatrix} \tag{1.17}$$

Naturally, this can be rewritten to the relation between the flavor and mass states as

$$|\nu_e\rangle = \cos(\theta)|\nu_1\rangle + \sin(\theta)|\nu_2\rangle \qquad |\nu_\mu\rangle = -\sin(\theta)|\nu_1\rangle + \cos(\theta)|\nu_2\rangle \tag{1.18}$$

With the schrödinger equation and using $E_i = \sqrt{p^2 + m_i^2} \simeq p + \frac{m_i^2}{2E}$ the transition probability can be derived:

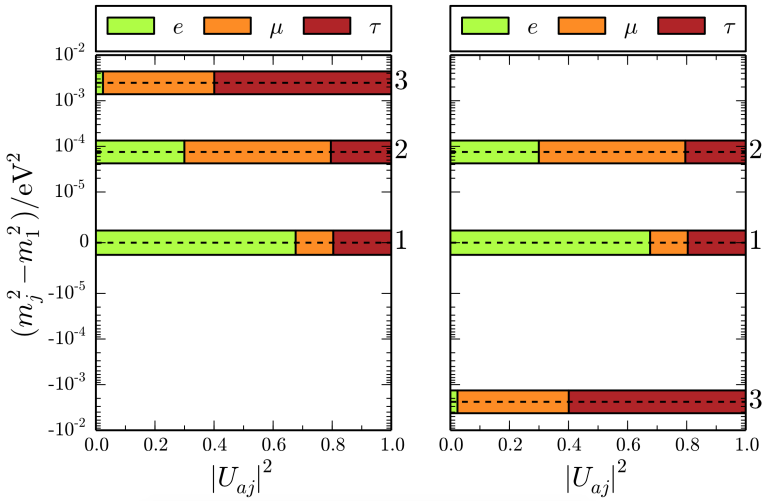


**Figure 1.3:** *The oscillation spectrum of the three neutrino mass and flavor eigenstates. The mass differences $\delta m^2$, $\Delta m^2$ and $\Delta m^2_{23}$ correspond to current best fit values as given in table 1.1, whereas whether the mass hierarchy is inverted or normal is to be determined. Here, the masses are normalized to the lightest neutrino, which is either $\nu_1$ (NH) or $\nu_3$ (IH). The colors denote the fractions $|U_{aj}|^2$ of flavor mixing for a specific mass eigenstate $j$. Figure taken from [57].*

$$P(\nu_e \to \nu_\mu; t) = \sin^2(2\theta) \sin^2\left(\frac{\Delta m^2}{4E}\right), \tag{1.19}$$

where $\Delta m^2 = m_2^2 - m_1^2$.

The transition probability can also be expressed in travelled distance $L$,

$$P(\nu_e \to \nu_\mu; L) = \sin^2(2\theta)\left(\pi \frac{L}{l_{osc}}\right). \tag{1.20}$$

Here, $l_{osc}$ is the oscillation length, defined as $l_{osc} = \frac{4\pi E}{\Delta m^2}$, distance $L$ is in m and energy E is in MeV. A more extensive derivation of (1.19) can be found in [17].

### 1.1.2 Neutrino Mass Hierarchy

As shown with equation (1.12) and (1.19), the mass difference $\Delta m^2_{ij}$ and mixing angles $\theta_{ij}$ are the properties that can be derived from oscillation experiments. In fact, some of these have been measured. We know that all mixing angles are non-zero. $\theta_{13}$ is the smallest, but definetly non-zero, $\theta_{12}$ and $\theta_{23}$ are significantly larger [25]. The known mass differences are visualized in 1.3.

What needs to be determined is wether the three neutrino mass eigenstates are either ordered in a Normal Hierarchy (NH) or Inverted Hierarcy (IH)

$$m_1 < m_2 < m_3 \qquad \text{(NH)} \tag{1.21}$$

$$m_3 < m_1 < m_2. \qquad \text{(IH)} \tag{1.22}$$

Oscillations in vacuum are independent of the sign of $\Delta m^2_{31}$ as can be seen in the even function (1.12). Consequently, determining the mass hierarchy can not be done by studying neutrino oscillation in vacuum.

### Matter Effects

Neutrinos oscillate in vacuum with a probability described with equation (1.12). Neutrinos propagating through matter can interact weakly through CC and NC interactions. As shown in the previous section, neutrino oscillation occur due to phase differences for different neutrinos. Since NC interactions are similar for all types of neutrinos in the Standard Model, oscillations are not affected by those and NC can be disregarded in the matter effects.

For CC currents the amplitudes differ. Due to the abundance of electrons, CC coherent forward scattering of $\nu_e$ on electrons is dominant in matter. Effectively, the scattering of $\nu_e$ changes the effective mass of $\nu_e$, consequently changing the squared mass difference. This influences the amplitude of electron neutrino oscillation in (1.12), which leaves its mark on the composition of neutrino flavors that travel through a block of changing matter density such as the earth.

With this information, the evolution of a neutrino in the flavor basis $\nu_f$ can be described with the Schrödinger equation

$$i\frac{d}{dt}|\nu_\alpha\rangle = \left(\frac{UM^2U^\dagger}{2E} + V\right)|\nu_\alpha\rangle \tag{1.23}$$

Where $M$ is a diagonal matrix with $m_1^2, m_2^2, m_3^2$ as elements, $U$ is the PMNS matrix as in (1.5) and $V$ is a diagonal matrix with elements $V_e, 0, 0$, which is the CC contribution to the neutrino potential [17].

For the two flavor case, the evolution equation in matter is

$$i\frac{d}{dt}\begin{pmatrix}\nu_e\\ \nu_\mu\end{pmatrix} = \begin{pmatrix} -\frac{\Delta m^2}{4E}\cos(2\theta_m) + V_e & \frac{\Delta m^2}{4E}\sin(2\theta_m) \\ \frac{\Delta m^2}{4E}\sin(2\theta_m) & \frac{\Delta m^2}{4E}\cos(2\theta_m)\end{pmatrix}\begin{pmatrix}\nu_e\\ \nu_\mu\end{pmatrix}, \tag{1.24}$$

with $V_e = \sqrt{2}G_F N_e$, where $G_F$ is the Fermi constant and $N_e$ is the electron number density.

This equation describes the $\nu_e \longleftrightarrow \nu_\mu$ oscillation. The evolution equation for $\nu_e \longleftrightarrow \nu_\tau$ is the same, replacing $\mu$ for $\tau$ and the appropriate squared mass difference. The two flavor approximation is appropriate in this case, because amplitudes $V_\mu$ and $V_\tau$ are equal [17].

Diagonalizing the effective Hamiltonian in the evolution equation (1.24) gives us the neutrino eigenstates in matter. From which the probability of $\nu_e \longleftrightarrow \nu_\mu$ can be derived. Important is that the resulting mixing angle $\theta$ is different in matter with respect to that in vacuum. The transition probability is therefore equation (1.20), with the matter effected mixing angle $\theta_m$ and oscillation length in matter $l_m$:

$$P(\nu_e \to \nu_\mu; L) = \sin^2(2\theta_m) \left( \pi \frac{L}{l_{osc}} \right). \tag{1.25}$$

The oscillation amplitude here is

$$\sin^2(2\theta) = \frac{\frac{\Delta m^2}{2E} \sin^2(2\theta_m)}{(\frac{\Delta m^2}{2E} \cos(2\theta_m) - \sqrt{2} G_F N_e)^2 + (\frac{\Delta m^2}{2E})^2 \sin^2(2\theta_m)} \tag{1.26}$$

From equation (1.26) follows that the maximum value $\sin^2(2\theta_m) = 1$ is reached with the condition

$$\frac{\Delta m^2}{2E} \cos(2\theta_0) = \sqrt{2} G_F N_e. \tag{1.27}$$

This is called the Mikheyev-Smirnov-Wolfenstein (MSW) resonance condition. When this is fulfilled, the mixing in matter is maximal, i.e. $\theta = 45°$. An important quality is that the mixing angle is maximal when the MSW condition is fulfilled, independent of the vacuum maxing angle. Therefore, even with a small vacuum mixing angle the flavour transition probability $P(\nu_\mu \longleftrightarrow \nu_e)$ can be large.

For the resonance enhancement in matter to be possible, the left hand side term in (1.27) must be positive, i.e.

$$\Delta m^2 \cos(2\theta_0) = (m_2^2 - m_1^2)(\cos^2(\theta_0) - \sin^2(\theta_0)) > 0. \tag{1.28}$$

Assuming that $\cos^2 \theta_0$ is positive, $\Delta m^2$ has to be positive. This would imply that the resonance condition for antineutrinos is $\Delta m^2 < 0$. We can conclude that depending on the NMH, either neutrino- or antineutrino oscillation is enhanced in the matter of the Earth [17].

This analytical derivation in the two flavor approximation shows that the possible hierarchy of the neutrino mass eigenstates results in different oscillation patterns, which can be tested with neutrino detectors.

Apart from MSW effect, $parametricenhancement$ is an important resonance effect for PINGU. Parametric resonance occurs for certain periodic density profiles of matter that is traversed by neutrinos. See [61] for an analytical discussion of parametric enhancement.

For certain mixing parameters and characteristics of the earths density, MSW and parametric resonance conditions are fulfilled. This significantly influences the atmospheric flux, which can be measured by PINGU. The next chapter will discuss these effects on the atmospheric neutrino flux in more detail.

The current best fitted values of the three flavor oscillation parameters from a global fit analysis of solar, atmospheric, reactor and accelerator neutrino data [39] are given in table 1.1. As discussed determining the sign of $\Delta m_1 3$ determines the NMH. How PINGU will be able to do this is discussed in the next chapter.

| | Normal Hierarchy | Inverted Hierarchy |
|---|---|---|
| | Best fit $\pm 1\sigma$ | Best fit $\pm 1\sigma$ |
| $\theta_{12}/^\circ$ | $33.48^{+0.78}_{-0.75}$ | $33.48^{+0.78}_{-0.75}$ |
| $\sin^2\theta_{12}$ | $0.304^{+0.013}_{-0.012}$ | $0.304^{+0.013}_{-0.012}$ |
| $\theta_{23}/^\circ$ | $42.3^{+3.0}_{-1.6}$ | $49.5^{+1.5}_{-2.2}$ |
| $\sin^2\theta_{23}$ | $0.452^{+0.052}_{-0.028}$ | $0.579^{+0.025}_{-0.037}$ |
| $\theta_{13}/^\circ$ | $8.50^{+0.20}_{-0.21}$ | $8.51^{+0.20}_{-0.21}$ |
| $\sin^2\theta_{13}$ | $0.0218^{+0.0010}_{-0.0010}$ | $0.0219^{+0.0011}_{-0.0010}$ |
| $\frac{\Delta m_{21}}{10^{-3}eV^2}$ | $7.50^{+0.19}_{-0.17}$ | $-7.50^{+0.19}_{-0.17}$ |
| $\frac{\Delta m_{3\ell}}{10^{-3}eV^2}$ | $+2.457^{+0.047}_{-0.047}$ | $-2.449^{+0.048}_{-0.047}$ |

**Table 1.1:** *Current Three-flavor oscillation parameters from a fit to global data for both NH and IH. Note that $\Delta m_{3\ell} = \Delta m^2_{31} > 0$ for NH and $\Delta m_{3\ell} = \Delta m^2_{32} < 0$ for Inverted Hierarchy. Values taken from [39]*

# Chapter 2

# Atmospheric neutrinos

Cosmic Rays (CR), which have been accelerated by astrophysical sources in galactic and intergalactic sources, interact within the earth's atmosphere, creating air showers, in which neutrinos are produced. Neutrinos originating from cascades in the atmosphere are called atmospheric neutrinos. Using this neutrino component, PINGU can determine the Neutrino Mass Hierarchy.

In this chapter, some important aspects of atmospheric neutrinos are summerized. The focus is on the properties that are relevant for PINGU and the POCAM design study.

## 2.1 Cosmic Ray Air Showers

Primary CRs are mainly charged nuclei hitting the Earths atmosphere. They interact at the top of the atmosphere, inducing hadronic cascades which result in air showers. The direct products of the CR interactions are called secondary Cosmic Rays. The primary interaction takes place at a height of approximately $20\,\mathrm{km}$, or higher for heavier Cosmic Rays. The air showers can be measured with ground based experiments such as IceCube's CR detector IceTop [71].

As in figure 2.1a, primary CRs consist primarily of hydrogen. The flux of other primary nuclei decreases with charge number $Z$. Due to the electromagnetic charge of the primary Cosmic Rays, one parameter that can not be derived from detection is the direction of the origin, since the path is influenced strongly by encountered magnetic fields. However, according to theory, high-energy astrophysical neutrinos originate from the same astrophysical high energy sources as the high energy Cosmic Rays. Therefore, the detection of high energy neutrinos with detectors such as IceCube could offer insight in the origin of high energy Cosmic Rays. Another way that CRs and neutrinos are connected is the atmospheric neutrino flux, which originates from CR induced air showers.

### 2.1.1 Cosmic Ray Spectrum

Naturally, the flux of atmospheric neutrinos is entirely dependent on the CR spectrum. This spectrum, as can be seen in 2.1b, covers over 31 orders of magnitude in flux and 11 orders of magnitude in energy. The spectrum shows two interesting transitions, named

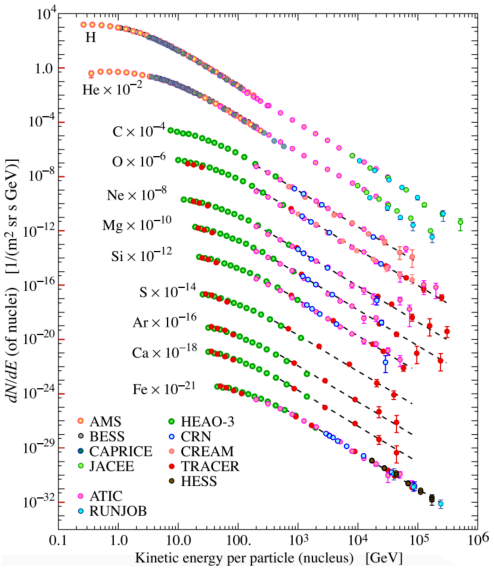


**(a)** *Cosmic Ray flux of the most abundant elements against energy per particle*

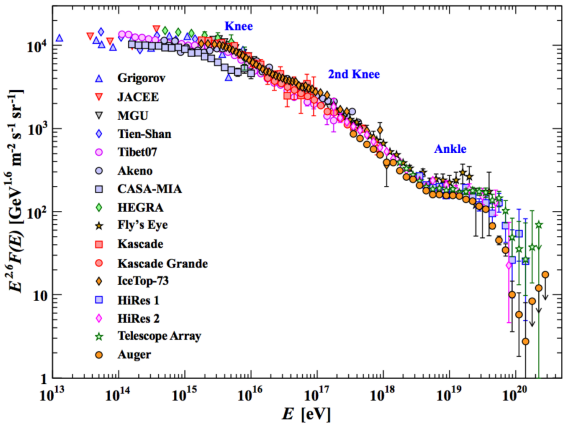


**(b)** *Cosmic Ray spectrum of all particles from several air shower measurements. [63].*

**Figure 2.1:** *Cosmic Ray spectrum for the most abundant particles separately (a) and the flux for all nuclei against the energy per particle. Data from a number of experiments is used [63]. The spectrum follows the power law refeq:crspectrum. Spectral index $\gamma$ differs for the several components of which the flux consists. The transitions marked here are the knee, second knee and the ankle.*

the knee and the ankle. Above a few GeV the spectrum follows a simple power law,

$$\frac{d\phi}{dE} = \phi_0 E^{-\gamma}, \tag{2.1}$$

with

$$\phi_0 = 1.8 \cdot 10^4 m^{-2} s^{-1} sr^{-1} GeV^{\gamma-1}. \tag{2.2}$$

Up to the knee, marked in 2.1b, the spectral index $\gamma$ is equal to 2.7. At the knee the flux has decreased to 1 particle per $m^2$ per year. After the knee the spectral index steepens to 3.0. Assuming that the CRs with energies below $10^{18}$ eV are of galactic origin, the knee is associated with a maximum in energy reachable for most galactic accelerators [63].

A second steepening has been observed near $8 \times 10^{16}\,\mathrm{eV}$, which has been named the 'second knee'. This is supposed to be a transition from light to heavier primary particles [19]. At the next transition, called the ankle, at $\sim 10^{19}\,\mathrm{eV}$, the spectrum softens again to $\gamma \sim -2.7$. The ankle is theorized to be a transition from galactic to extra galactic origin of the primary particle. The spectrum falls off strongly above $10^{19}\,\mathrm{eV}$ due to interaction with he cosmic microwave background, this is the so called the GZK cutoff [41].

### 2.1.2 Air Showers

Primary CRs interact with the atmosphere, producing secondary particles, which in turn interact or decay. This effectively results in a set of cascades, which is called an

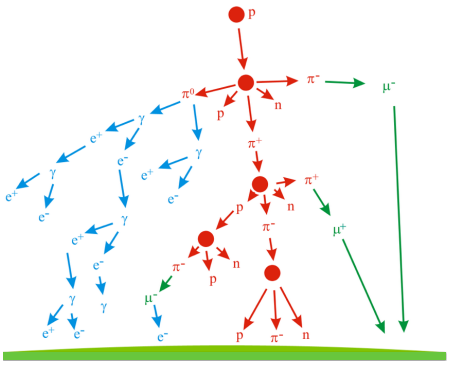


**Figure 2.2:** *Schemtic depiction of a cosmic-ray air shower with the electromagnetic component in blue, the hadronic component in red and the muonic component in green. Figure taken from [16].*

air shower, as illustrated in figure 2.2. An air shower can be subdivided into three parts. An electromagnetic component, consisting of electrons and photons, a hadronic component, consisting of primarily protons, neutrons, pions and kaons. The mesons in turn decay into muons and neutrinos, which is called the muonic component of the air shower, and the muonic component of air showers is the main source of atmospheric neutrinos [63].

Since the CR flux is close to isotropic over the earth's atmosphere and neutrinos traverse the earth, atmospheric neutrinos reach IceCube from all directions. This means that muons from air showers in the northern hemisphere do not reach the detector, as the Earth filters them. However, the atmospheric neutrinos from the northern hemisphere traverse the Earth and do reach the detector, with a flux of approximately $10^5$ per year. From the unshielded southern hemisphere, both atmospheric muons and neutrinos reach the detector, with a flux of about $10^{11}$ events per year [63].

For IceCube, these atmospheric muons are considered background to astrophysical neutrinos and studies are done for the sole purpose of proper filtering. PINGU, however, aims to detect atmospheric neutrinos precisely for their large abundance and wide energy spread.

## 2.2 Atmospheric Neutrino Flux

As discussed, the atmospheric neutrino flux is directly connected to the CR flux. Therefore, with a precise understanding of the CR spectrum and flux, the atmospheric neutrino flux can be estimated.

The flux of atmospheric neutrinos mainly consists of neutrinos resulting from the pion and kaon production in air showers. Pions decay to muons and neutrinos with branching ratios of $\sim$100%, the muons produce neutrinos in decays as well.

$$\pi^+ \rightarrow \mu^+ + \nu_\mu \tag{2.3}$$
$$\pi^- \rightarrow \mu^- + \bar{\nu}_\mu \tag{2.4}$$

After pions, kaons from CRs are the main contributor to the atmospheric neutrino flux. Kaon decay is similar to pion decay, but allows decays into electrons as well.

$$K^+ \rightarrow \mu^+ + \nu_\mu \tag{2.5}$$
$$K^- \rightarrow \mu^- + \bar{\nu}_\mu \tag{2.6}$$

The muons from these interactions consequently decay into electrons and neutrinos

$$\mu^+ \rightarrow e^+ + \bar{\nu}_\mu + \nu_e \tag{2.7}$$
$$\mu^- \rightarrow e^- + \bar{\nu}_e + \nu_\mu \tag{2.8}$$

At low energies, the neutrinos from the muon decays are the dominant contribution to the muon flux.

The decay length $\lambda$ of a particle with mean lifetime $\tau$ in the boosted lab frame with Lorentz factor $\gamma$ is

$$\lambda = \gamma c\tau = \frac{c\tau}{mc^2} E = h_0 \frac{E}{\epsilon}. \tag{2.9}$$

Here, $\epsilon$ is the characteristic energy. At energies higher than $\epsilon$, the decay length is longer than the atmospheric scale height $h_0$. Other interactions start to play a role for these energies and the muon and neutrino production in decays is suppressed.

The characteristic energy of muons is $\epsilon_\mu \sim 16\text{GeV}$. Therefore, at energies higher than this, the muons decay length $\lambda$ is so long that they generally reach sea level without decaying and contribute significantly to the flux of IceCube and PINGU. Therefore, they contribute to the neutrino flux at the few GeV level, but have no significant contribution to the flux at higher energies. At energies of more than a few GeV the neutrinos from pion decay (2.4) and kaon decay (2.6), called *conventional* neutrinos, form the main contribution to the atmospheric neutrino flux.

This flux can be approximated as

$$\phi_\nu(E_\nu) = \phi_N(E_\nu) \left( \frac{A_{\pi\nu}}{1 + B_{\pi\nu} cos\theta \, E_\nu/\epsilon_\pi} + \frac{A_{K\nu}}{1 + B_{K\nu} cos\theta \, E_\nu/\epsilon_K} \right). \tag{2.10}$$

This expresses the neutrino flux $\phi_\nu$ in neutrino energy $E_\nu$, relating it to the primary CR flux $\phi_N$ at $E_\nu$ [36]. The first term in the brackets describes the $\nu_\mu$ production from pions, the right term the production from kaons. Constants $A_{\pi\nu}$ and $A_{K\nu}$ contain the cross sections and branching ratios of the corresponding decay. Factors $\epsilon_\pi = 115\,\text{GeV}$ and $\epsilon_K = 850\,\text{GeV}$ are the characteristic energies of pions and kaons [36]. $B_{\pi\nu}$ and $B_{K\nu}$ depend on the hadronic attenuation length and the decay kinematics [37].

For high energies, neutrinos originating from the decays of heavier mesons containing charm quarks, such as the D-mesons, are the dominant contribution to the flux. Neutrinos from these decays are called *prompt* neutrinos. Additionally, at these energies

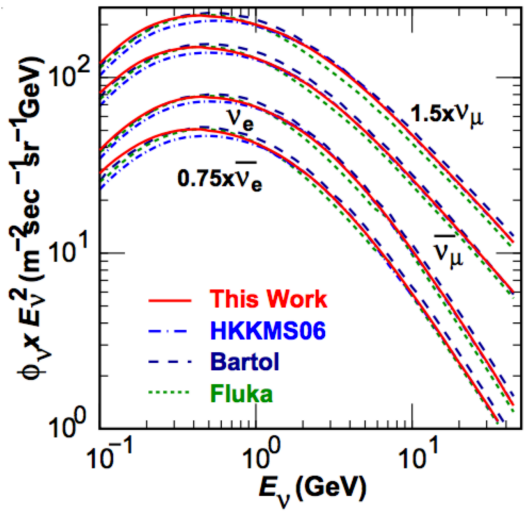


**Figure 2.3:** *The atmospheric neutrino flux per steradian, averaged over all directions. Compared are the fluxes according to [45], their previous work, and the work by the Bartol [45] [21] and the FLUKA group [22]. $\bar{\nu_\mu}$ is scaled with a factor 1.5, and $\bar{\nu_e}$ with a factor 0.75 for the sake of clarity.*

$\nu_\tau$ can contribute to the atmospheric neutrino flux. A prompt neutrino flux has been predicted, but has not yet been detected [36].

Understanding and measuring the atmospheric neutrino flux is an ongoing pursuit. In figure 2.3 a recent estimate of atmospheric neutrino flux is shown for energies from $0.1\,\mathrm{GeV}$ to $32\,\mathrm{GeV}$ averaged over all directions . Several models and measurements are incorporated to estimate the conventional flux for $\nu_\mu$, $\bar{\nu}_\mu$, $\nu_e$ and $\bar{\nu}_e$ [45].

## 2.3 Oscillation of Atmospheric Neutrinos

At low energies, the direction of the atmospheric neutrino flux is influenced by the geomagnetic field. For energies above a few GeV, this effect is not relevant [38]. Therefore, the production of high-energy atmospheric neutrinos is practically uniform over the atmosphere. Leaving out oscillations, this implies that at any possible detector location, the flux of each neutrino flavor arriving from opposite directions is the same.

However, due to effects as the MSW resonance (see section 1.1.2) neutrino oscillation are influenced in the Earth. The oscillation probability (1.12) depends on the neutrino energy and the path length through the Earth.

Prediction of matter effects of the Earth on the atmospheric neutrino flux can be made using Earth density models. Figure 2.4 shows an Earth model based on data from seismic measurements [32], additionaly, a neutrino path length $L$, i.e. the distance between the interaction vertex in the atmosphere and the point of detection in a detector, is specified. L can be expressed in the zenith angle $\theta$, the distance between the Earths center

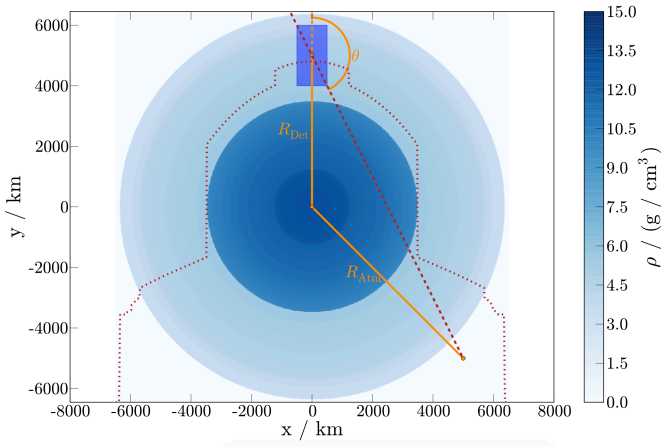


**Figure 2.4:** *An earth density profile [32], shown as a radial profile in a blue colorscale and red dotted with corresponding values. The zenith angle $\theta$, the distance from the centre of the earth to the detector $R_{Det}$ and the distance to the atmosphere $R_{Atm}$ are visualized. With these equation (2.11) can be derived. Figure taken from [29].*

and the detector $R_{\text{Det}}$ and the distance between the neutrino production vertex.

$$L = \sqrt{R_{\text{Atm}}^2 + R_{\text{Det}}^2 - 2R_{\text{Atm}}R_{\text{Det}}\cos\left(\pi - \arcsin\left(\frac{R_{\text{Det}}}{R_{\text{Atm}}}\sin(\pi - \theta)\right)\right)} \tag{2.11}$$

This shows that using Earth models and a range of baseline lengths and energies can be studied with an atmospheric neutrino detector such as PINGU.

The dominant oscillations in the atmospheric neutrino flux is due to the large mixing angle $\theta_{23}$, responsible for $\nu_\mu \to \nu_\tau$ oscillations.

A numerical calculation of survival probability for $\nu_e$ and $\nu_\mu$ neutrinos is visualized in figure 2.5. Here, the NMH is assumed to be Normal.

The survival probabilities $P(\nu_\mu \to \nu_\mu)$ and $P(\nu_e \to \nu_e)$ shown exhibit clear patterns of neutrino disappearance at certain $\theta$, $E$ regions.

For electron neutrinos with energies between $5\,\text{GeV}$ and $7\,\text{GeV}$ traversing the Earths mantle, where $\cos(\theta_\nu) \geq -0.84$, MSW resonance occurs, resulting in a minimum in survival probability. Electron neutrinos traversing the Earths core, with $\cos(\theta_\nu) < -0.84$ with energies above $3\,\text{GeV}$, have a minimum survival probability due to parametric enhancement [61]. Below $3\,\text{GeV}$ MSW resonance causes a minimum in survival probability for core-passing electron neutrinos. The regular pattern for $E_\nu < 5\,\text{GeV}$ and $\cos(\theta_\nu) > -0.84$ is expected for vacuum oscillations [18].

The muon neutrino oscillation is also influenced by matter due to mixing with electron neutrinos. The survival probability in 2.5a therefore also shows some distinct patterns. The most important being the general distortion at energies below $10\,\text{GeV}$, where the matter effect on electrons are the strongest [18].

The here described features of the survival probabilities variate with the oscillation parameters. A higher value for $\theta_{13}$ results in more distinct patterns. Furthermore, in

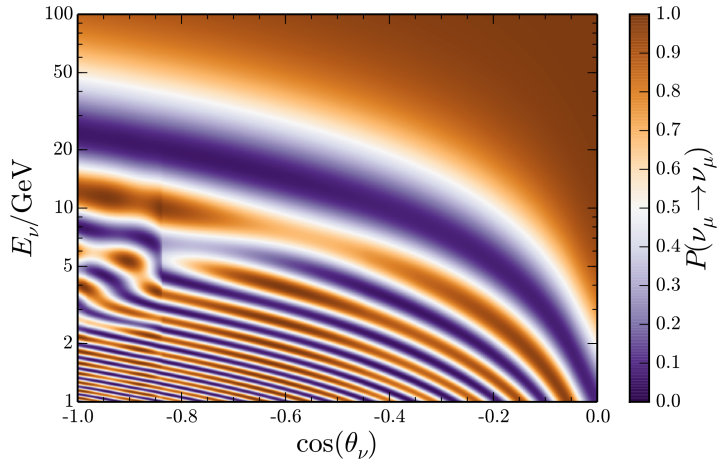


**(a)** *Muon neutrino survival probability.*

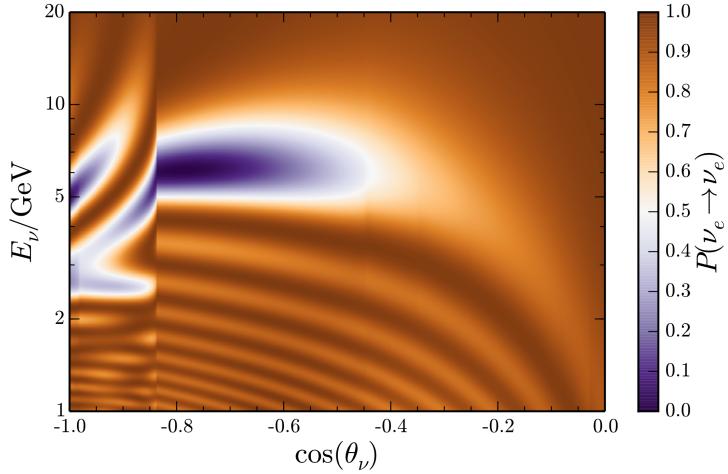


**(b)** *Electron neutrino survival probability.*

**Figure 2.5:** *Survival probabilities of the atmospheric $\nu_\mu$ (a) and $\nu_e$ flux. Shown is the neutrino energy against cosine of the neutrino zenith angle, with color coding for the probabilities. The survival probabilities are calculated with nuCraft [72] assuming NH. Figures taken from [57].*

the here assumed NH matter effects occur for neutrinos while they do not for anti-neutrinos, and for IH vice versa. Naturally, PINGU can not distinguish an neutrino from an anti-neutrino event. However, the cross section of neutrinos with nucleons is bigger than that of antineutrinos with nuclei, as is shown in figure 4.1. In the case of IH, the patterns caused by matter effects are less dominant for muon neutrinos, but more dominant for electron neutrinos. Therefore, PINGU is able to determine the NMH.

# Chapter 3

# IceCube Neutrino Observatory

The IceCube Neutrino Observatory is a cubic-kilometer detector built in the clear ice of the South Pole. In a broad spectrum of research goals, its main purpose is to detect high-energy neutrinos in the TeV and PeV range. Detection of neutrinos at these energies has opened a new window to study the cosmos. Recently, IceCube has in fact been the first to report a statistically significant flux of non-terrestrial neutrinos [2]. Furthermore, IceCube is competitive at low energies with Deepcore, pushing the energy threshold down to about $10\,\mathrm{GeV}$ [8]. A next generation IceCube detector is under study, consisting of a low energy extension, the Precision IceCube Next Generation Upgrade (PINGU) [3], and the High Energy Extension (HEX) [26].

For this thesis, a detailed understanding of the Precision IceCube Next Generation Upgrade (PINGU) is crucial for the design and proper implementation of the Precision Optical CAlibration Module (POCAM). To understand and properly introduce PINGU, a discussion of IceCube is given here. Therefore, this chapter will introduce the principles of neutrino detection, the geometry and experimental setup of IceCube and the calibration systematics in the current detector.

## 3.1 Neutrino Detection

Since neutrinos only interact through the weak interaction and generally have small cross-sections, their interaction probability with any medium is small. Detection in neutrino detectors is usually achieved indirectly through Cherenkov radiation induced by charged leptons. In order to reach reasonable statistics, large volume detectors are essential. IceCube therefore consists of a cubic-kilometer of instrumented ice. Optical modules in the ice measure Cherenkov photons, produced by charged leptons travelling through the ice with speeds greater than the speed of light in the ice. The process of neutrino interactions which indirectly produces Cherenkov light will be explored in this subsection.

### 3.1.1 Neutrino Interactions

There are several interactions mechanisms through which neutrinos interact with matter, which are all through the weak interaction. The interaction is either through charged

current interaction (CC), exchanging $W^{\pm}$ bosons, or through Neutral Current interaction (NC), exchanging $Z^0$ bosons. For high neutrino energies, $E_\nu > 10\,\mathrm{GeV}$, Deep Inelastic Scattering (DIS) is the dominant process. For energies lower then $10\,\mathrm{GeV}$ other processes like quasi-elastic (QE) scattering are dominant.

For IceCube, DIS is the important process. In these processes, a neutrino scatters on a Nucleon $N$ inelastically through either CC or NC, producing charged leptons $\ell^{\pm}$ and/or a hadron $X$, which in turn interacts, resulting in a hadronic cascade.

$$\nu_\ell + N \rightarrow \ell^- + X \qquad (CC) \tag{3.1}$$
$$\bar{\nu_\ell} + N \rightarrow \ell^+ + X \qquad (CC) \tag{3.2}$$
$$\nu_\ell + N \rightarrow \nu_\ell + X \qquad (NC) \tag{3.3}$$
$$\bar{\nu_\ell} + N \rightarrow \bar{\nu_\ell} + X \qquad (NC) \tag{3.4}$$

For PINGU, aimed at lower neutrino energies (few GeV), QE interactions are the dominant processes, which will be elaborated on in chapter 4.

The most relevant processes described here are those where charged leptons are created. When these travel at a speed higher then the speed of light in the ice (superluminal), they will produce Cherenkov radiation when propagating through optical transparent media such as air, water, or ice. These Cherenkov-photons are detected and used to reconstruct neutrinos travelling through the South Pole ice.

### 3.1.2 Cherenkov Effect

As described, IceCube detects neutrinos by gathering photons that are produced by superluminal charged particles. When such a particle travels through a dielectric medium, the electromagnetic field is shortly disturbed. The EM-field of the charged particle polarizes the local field in the medium. At non-superluminal velocities the field falls back to equilibrium shortly after the particle has passed through. However, when the speed of the particle is higher than the local speed of light in the ice, the response speed is lower than the travelling speed, resulting in a disturbance in the wake of the particle, creating a shockwave of Cerenkov photons [27], as visuallized in 3.1. The Cherenkov photons are emitted in a direction forming an angle $\theta$ with the path of the electron, determined by

$$\cos(\theta_{ch}) = \frac{1}{\beta n}, \tag{3.5}$$

where n is the refractive index of the medium, $\beta$ is the fraction of the particle's velocity and the speed of light. For ultra-relativistic particles travelling through ice the Cherenkov angle is approximately $\theta_{ch} = 41°$ [4]. The amount of Cherenkov photons $N_\gamma$ with a wavelength $\lambda$ emitted by a particle is described by the Frank-Tamm formula [63]

$$\frac{dN_\gamma}{dx} = \int_{\lambda_{min}}^{\lambda^{max}} d\lambda \frac{2\pi\alpha z^2}{\lambda^2}\left(1 - \frac{1}{\beta^2 n^2(\lambda)}\right). \tag{3.6}$$

Here, $\alpha$ is the fine-structure constant, the particles charge is $q = ze$ and $dx$ is the travelled distance. The Cherenkov spectrum is partly blue in the visible spectrum, but lies

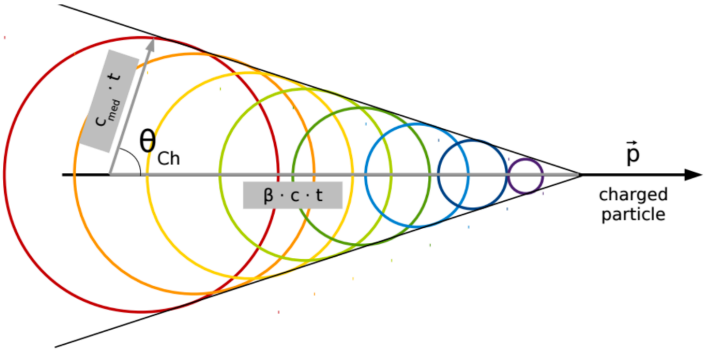


**Figure 3.1:** *Cherenkov light is emitted by a particle travelling at a velocity higher than the local speed of light. The electromagnetic field is perturbed and cherenkov radiation is emitted isotropically along the path of the particle. Resulting in bow-wave of photons at an angle* $\theta_{ch} = \frac{1}{\beta n}$ *[42]*

mostly in the ultraviolet band. IceCube's sensitivity is determined by the sensitivity of its Photomultipliers, which is in the spectral range of 300 to $650\,\mathrm{nm}$. The average quantum efficiency at $\lambda = 405\,\mathrm{nm}$ is ∼22% for IceCube phototubes and ∼29% for DeepCore phototubes [73].

## 3.2 IceCube Experimental Setup

The IceCube detector, as depicted in figure 3.2 consists of three conceptually distinct parts: The main detector, generally referred as IceCube, designed to detect high-energy neutrinos, IceTop, an array on the surface detecting air showers and Deepcore, designed to measure neutrinos of lower energies. The main IceCube detector is buried deep in the ice at a depth of 1450 to 2450 m. It comprises one cubic kilometer of instrumented ice with 86 strings each holding 60 Digital Optical Modules (DOMs), resulting in a total of 5160 DOMs. The DOMs, which will be discussed in more detail in the next subsection, are each equipped with a Photo Multiplier Tube (PMT), which is the main photon gathering component. The strings are evenly spaced with a horizontal distance of 125 m. The vertical distance between the DOMs on each string is 17 m. The PMTs are pointing down, i.e. in the northern direction, as to mainly detect light from upgoing neutrinos. This geometry results in an energy threshold of $100\,\mathrm{GeV}$ for neutrino detection.

IceCube was build during several seasons between 2005 and 2010, every season adding more strings whilst the instrumentation in place was able to run. Hole is the ice were drilled with a hot water jet. The strings with attached DOMS were lowered in the hole to the appropriate depth, after which water was let back in the and refrozen. The new hole-ice is not as dense and clear as the surrounding ice. This is of great importance for the ice models, which will be discussed in detail in 3.2.4.

Deepcore is at the centre of the detector and comprises a denser instrumented volume of ice. Consisting of 8 additional strings it lowers the energy threshold from $100\,\mathrm{GeV}$ to $10\,\mathrm{GeV}$, making it more adept to detect atmospherical neutrinos. The Deepcore array is divided by a notorious dust layer at a depth of 2000 to $2100\,\mathrm{m}$. The top 10 DOMs of each Deepcore string are located above the dust layer, the remaining 50 DOMs are located in

the exceptionally clear ice below the dust layer. The DOMs have an improved efficiency to the IceCube DOMs of approximately 35 % [8]. This, together with a vertical spacing of 7 m pushes the overall IceCube energy threshold below 10 GeV [8].

IceTop is a high-energy cosmic ray detector, consisting of 81 pairs of Cherenkov tanks, each of which is equipped with two optical modules. It serves multiple purposes. In conjunction with IceCube, IceTop enables the vetoing of in-ice events in combination with muon bundles produced by air-showers, and offers better understanding of the muon background in general. Individually, IceTop pursues its own scientific goals as a cosmic ray detector, sensitive to cosmic rays in the energy range of $500\,\mathrm{TeV}$ to 1 EeV [71].

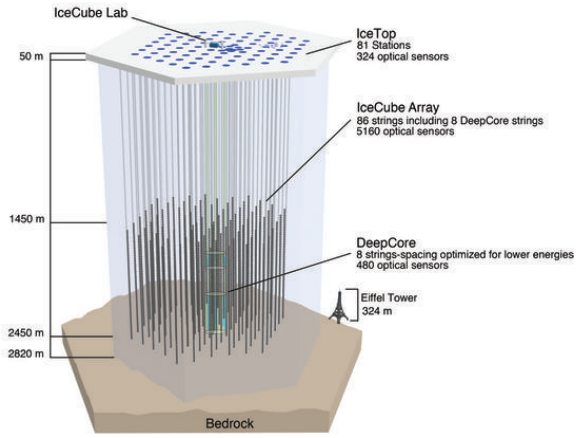


**Figure 3.2:** *Illustration of the IceCube detector in the South Pole ice, showing IceTop, the in-ice IceCube detector and Deepcore.*

### 3.2.1 The Digital Optical Module (DOM)

The actual detecting of photons in the ice is done by the DOMs. Figure 3.3 depicts the DOM and its components. This section will dissect the DOM and discuss the main components.

The hardware is protected from the Antarctic ice by a glass sphere. The housing, consisting of two hemispheres, is $1.25\,\mathrm{cm}$ thick, made of glass with a minimized number of radioactive isotopes. The outer diameter of the sphere is 13", i.e. $33\,\mathrm{cm}$. The two half spheres are glued together. An aluminium harness with an outer diameter of $18.5\,\mathrm{cm}$ is placed on the outside of the sphere. The purpose of the harness is to attach the DOMs to the main cable more than to keep the two hemispheres together. The penetrator connects the DOM's electronics to the main cable through an aperture in the glass. The DOM is attached to the main cable through the harness assembly as schematically shown in fig. 3.3b. In the ice, the waistband and the main cable actually touch, this information is important if one wants to consider the shadow of the cable.

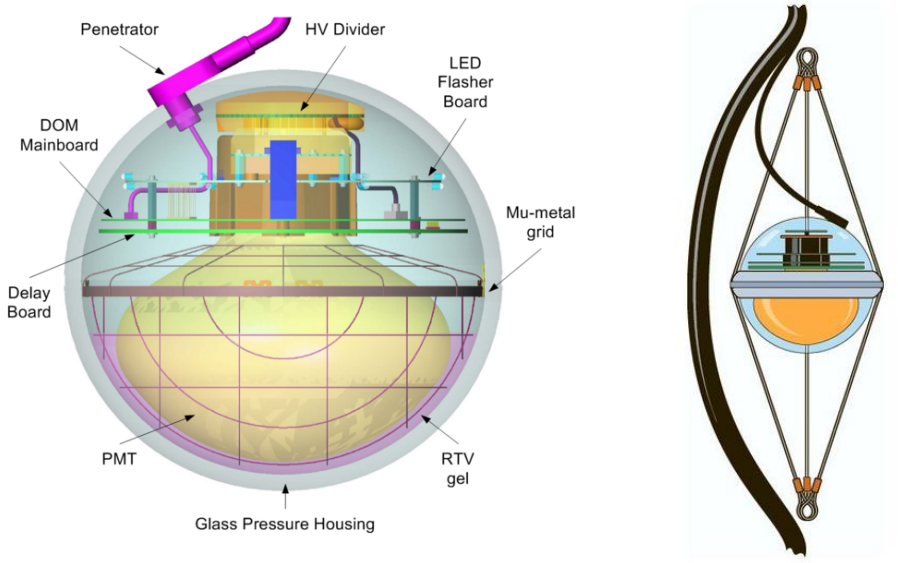


**(a)** *Schematic of a DOM*

**(b)** *Schematic of the DOM attached to the main cable*

**Figure 3.3:** *Illustration of the Digital Optical Module (DOM) used in IceCube. The downward facing PMT collets photons in the ice, which is read out and digitized by the main board, after which the data is sent to the surface through the main cable. [9]*

Every DOM is equipped with a $25.4\,\mathrm{cm}$ diameter PMT produced by Hamamatsu photonics, with a quantum efficiency of 25%. The mu-metal grid shields the PMT from the magnetic field of the earth. The DOM mainboard is a collection of electronics that digitizes the photoelectrons. The Analog Transient Waveform Digitizers (ATWD) can digitize waveforms in detail up to $422\,\mathrm{ns}$. The Fast Analog-to-Digitcal-Converter (FADC) can digitize waveforms up to $6.4\,\mu\mathrm{s}$. A waveform is digitized when the PMT signal reaches the trigger threshold of $0.25\,\mathrm{PE}$.

The LED flasher board is an important part of IceCube's calibration system. It consists of 12 LEDs placed in pairs around the flasher board. The beams are directed radially outward in six different azimuthal angles with an angular separation of $60°$. Of each pair, one is pointed horizontally, and the other upwards at an angle of $40°$. The total output from the LED ranges from approximately $10^6$ to $10^{10}$ photons. The angular spread of each beam is modelled with a gaussian profile with $\sigma = 10°$. By measuring LED flashes, the detector can be calibrated and the propagation of photons through the ice can be studied. This includes determining the detector geometry, verifying the calibration of time offsets and the time resolution, verifying the linearity of photon intensity measurement and the optical properties of the ice in the detector [4]. In section 3.3 and 3.2.3 the calibration and the Ice properties will be discussed in more detail.

When a signal triggers the DOM in at least 4 neighbouring DOMs within a time frame of $1\,\mu\mathrm{s}$, the signal is transmitted to the surface through the main cables. An event that complies to these conditions is called a Hard Local Conincidence (HLC). If these conditions are not fulfilled but the signal exceeds the threshold, the event is called a Soft Local Coincidence (SLC) and only part of the information is sent to the surface and saved.

### 3.2.2 Neutrino Detection in the Ice

The three generations of charged leptons, resulting from neutrino CC interactions (3.4), each have a typical pattern of radiation. The generation of a particle detected by IceCube is determined by this pattern, or signature. The signatures of $\nu_e$, $\nu_\mu$ and $\nu_\tau$ events as as observed by IceCube are depicted in figure 3.4.

Electrons lose all their energy in radiative losses in a short amount of time, these electromagnetic cascades, accompanied by hadronic cascades (see equation 3.4), result in an almost spherical light emission, as visualized in 3.4a. From this pattern the direction of the neutrino can be deduced to a resolution of 10° [1]. Since there is no track involved, the cascades are often completely contained in the detector, resulting in a fair energy reconstruction.

Interactions of muon neutrinos are characterized by a hadronic cascade, followed by Cherenkov emission along the path of the outgoing muon, as visualized in 3.4b. With a lifetime of $\tau_\mu$ = 2.197 µs, the muon track is relatively long, enabling a precise determination of the direction of the muon. The $\nu_\mu$ direction is strongly correlated to the direction of the muon and can therefore be reconstructed to a precision of $1\,^\circ$.

The charged current interaction of a $\nu_\tau$ results in a $\tau$ lepton and a hadronic cascade (3.4). The $\tau$ decays after textrm$\tau_\tau$ = $2.906 \times 10^{-13}\,\mathrm{s}$ [63] in a second hadronic cascade. The signature, as visualized in 3.4c, is therefore also referred to as the 'double bang', due to its double hadronic cascade, connected by the track of the $\tau$ lepton. Tau neutrinos are rare in air showers, making them clear astrophysical neutrino candidates. Neutrino oscillation greatly increases the probability of an astrophysical neutrino to be of $\tau$ flavor. However, a $\nu_\tau$ is yet to be detected by IceCube. The high-energy Extension planned for IceCube-Gen2 would greatly improve the sensitivity for these events by greatly increasing the detector volume [6].

### 3.2.3 The Antarctic Ice

IceCube has been placed in the ice on Antarctica close to the South Pole due to the quality of the ice. The $\sim 3\,\mathrm{km}$ sheet of ice has accumulated over 45.5 million years [33], resulting in exceptional transparency, especially at the wavelength range of 200-400 nm [11]. The detector ice can be divided in two types. The bulk ice between the strings, and the melted and refrozen hole ice in which the strings are deployed: the hole ice. In any medium, photons are subject to absorption and scattering. Even in the very transparent South Pole ice, these factors play an important role in reconstructing the paths of the charged leptons. Naturally, the $3\,\mathrm{km}$ thick layer of ice is not perfectly homogeneous. Understanding the inhomogeneities and general characteristics of the ice is essential for the precision of the detector. A factor of significant influence on the absorption and scattering length of the ice is dust. The over millions of years accumulated layers of ice contain various concentrations of dust, connected to geological and atmospheric conditions at certain times in history. During drilling the dust concentrations were measured, resulting in the dust densities as visualized in figure 3.5.The most significant dust layer is located between 1950 m and 2100 m. Three smaller dust layers are present between 1500 and 1900 m [24], which is visualized in Figure 3.5. These layers of higher dust densities have significantly lower the local absorption and scattering

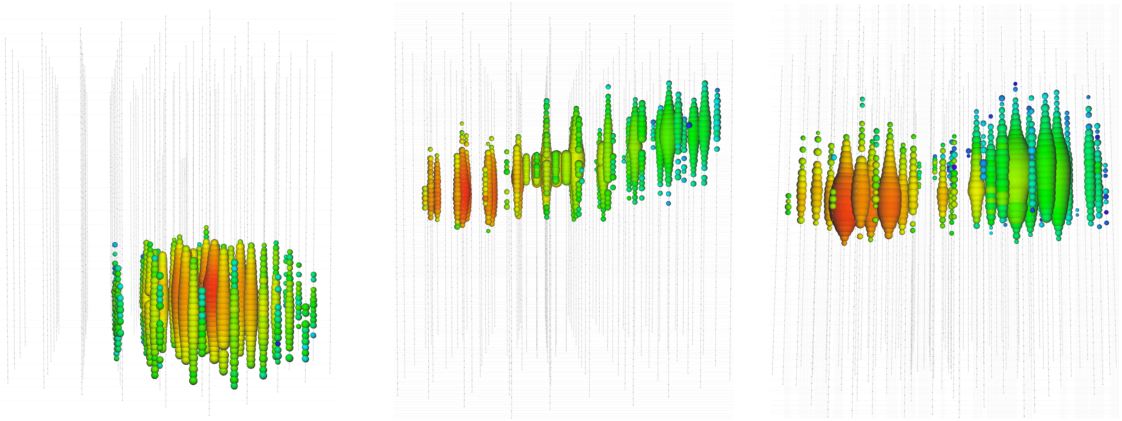

**(a)** *A $\nu_e$ event with an energy of $E_{\nu_e}$ =1.1 PeV inside IceCube.*

**(b)** *A $\nu_\mu$ event with an energy of $E_{\nu_\mu}$ = 3 PeV inside IceCube. A $\nu_\mu$ is characterized by a long track, clearly illustrated by this event.*

**(c)** *A $\nu_\tau$ event with an energy of $E_{\nu_\tau}$ = 4.7 PeV. This simulated event illustrates the double bang signature with the characteristic two cascades and a Cherenkov track. Such an event is still to be observed by IceCube [6]*

**Figure 3.4:** *Event signatures of simulated $\nu_e$, $\nu_\mu$ and $\nu_\tau$ neutrino events. The colored spheres represent IceCube DOMs that detect photons. The radius is proportional to the amount of measured photons. The color represents time of measurement, ranging from red to blue [42].*

length. In IceCube, the LED flashers offer a way to study the ice. This has resulted in more and more refined ice models. The POCAM could refine these further.

### 3.2.4 Ice Models

Ice models are essential for accurate reconstruction of neutrino events. Current ice models describe the ice by dividing it in a number of sheets of ice. For every sheet, the properties describing the ice are defined for a range of wavelengths. To determine these these parameters, measurements are performed. The LEDs in DOMs emit photons, which are measured by other DOMs. The measured charge and arrival times of the photons are fitted to find the scattering and absorption lengths that best describes the data [4].

dependent parameters are the scattering coefficient for a wavelength of $400\,\mathrm{nm}$ $b_e(400)$, the average distance before absorption at $\lambda = 400\,\mathrm{nm}$ $a_{dust}(400)$ and the depth dependent relative temperature $\delta T$ [4]. The geometrical scattering coefficient for other wavelengths is

$$b_e(\lambda) = b_e(400\mathrm{nm}) * \left(\frac{\lambda}{400\mathrm{nm}}\right)^{-\kappa}. \tag{3.7}$$

And the absorption coefficient for wavelength $\lambda$ is

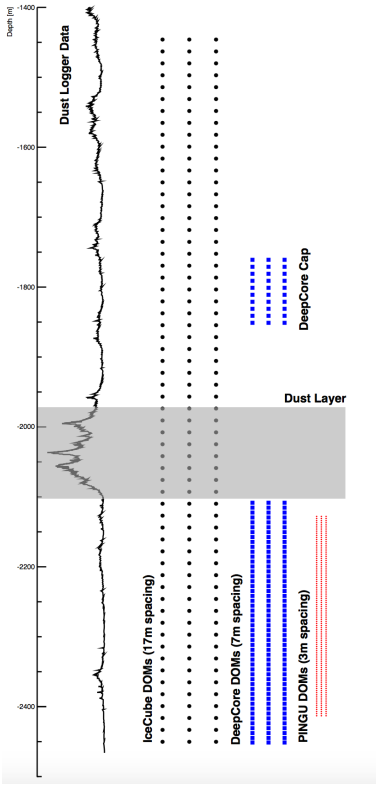


**Figure 3.5:** *Dust logger data gathered with laser dust loggers in the drilling holes during detector deployment [58].*

$$a(\lambda) = a_{dust}(\lambda) + Ae^{-B/\lambda}(1 + 0.01 \cdot \delta T) \tag{3.8}$$

$$\tag{3.9}$$

with

$$a_{dust}(\lambda) = a_{dust}(400\text{nm}) \left(\frac{\lambda}{400\text{nm}}\right)^{-\kappa}. \tag{3.10}$$

$$\tag{3.11}$$

The scattering and absorption lengths are the inverse of the respective coefficients. Here, $\kappa$ is the global fit parameter. A and B are two normalizing parameters, $\delta T = T(d) - T(1730\text{m})$ is the difference between the temperature at depth $d$ and the temperature at a depth of $1730\,\text{m}$, a value originating from the AMANDA detector, IceCubes predecessor [4]. in figure 3.6 the values of the effective scattering $b_e(400\text{nm})$ and absorption $a(400\text{nm})$ in the instrumented ice, as determined with the IceCube flasher data, are shown.

The effect of the several dust layers can clearly be seen in both parameters in figure 3.6. In the dust regions, the absorption length in these regions is only ∼20m and the effective scattering ∼5 m. The ice is clearest at depths of $2200\,\text{m}$ to $2500\,\text{m}$, where Deepcore is installed and PINGU is planned to be installed. The absorption length in this region goes up to $250\,\text{m}$ and the effective scattering up to $100\,\text{m}$. In figure 3.6, two different ice models can be distinguished, SPICE3 and SPICE-LEA, which are the two most recent

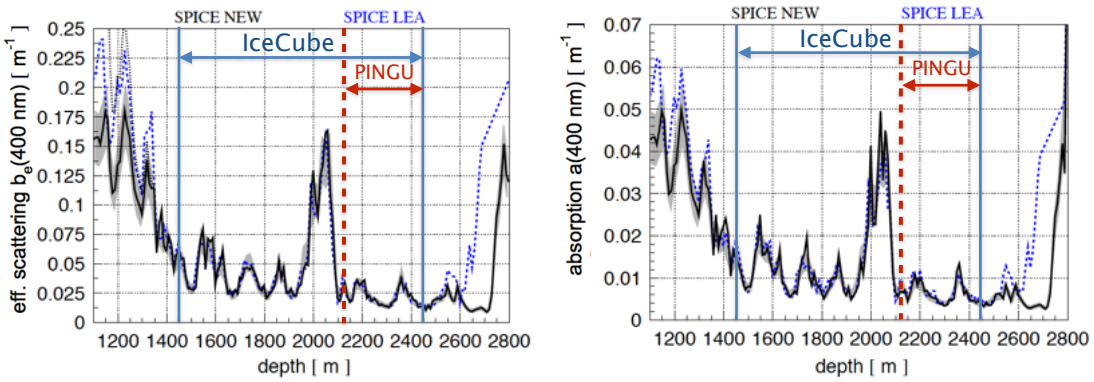


**(a)** *Values of the effective scattering length* $b_e(400)$ *vs depth.* **(b)** *Values of the effective absorption coefficient* $a(400)$ *vs. depth.*

**Figure 3.6:** *Results of a LED calibration study of the ice scattering (a) and absorption (b) for the most recent ice models SPICE3 (Blue) and SPICE-lea (black). The depths of PINGU and IceCube are indicated. The grey band around the line covers the estimated uncertainties [67].*

models.

The ice models date back to IceCube predecessor, AMANDA [11]. Since then the models have gotten more and more refined. The first South Pole ICE (SPICE) model dates back to 2009. In SPICE2, the propagation simulations were fitted better to the data by including a tilt in the dust layers. In the subsequent model, SPICE-MIE, a scattering function was fitted to the data. In SPICE-LEA, the model was complemented by a found anisotropy in scattering length over zenith angle. Whereas the previous version fitted to the flasher data of one string, SPICE3 fits across 7 strings. Furthermore the extrapolation based on dust profiles and ice tilt from the dust logger was improved [51]. The scattering and absorption coefficients of this latest model, SPICE3, can be found in figure 3.6.

As mentioned before the hole ice properties differ from those describing the bulk ice. Bubbles of air frozen in the ice significantly lower the scattering- and absorption length. In first approximation, this results in a bigger angular acceptance of the DOMs. Therefore, in simulations the hole ice is only implemented by modifying the angular acceptance.

## 3.3 Calibration in IceCube

Event reconstruction in IceCube uses the detected time, position and amount of measured light of an event to reconstruct the properties of charged leptons propagating through the detector. Accurate reconstruction relies heavily on proper calibration of the timing, geometry, photon detection and ice models. Uncertainty in any of these measurements comprise the detector based systematic uncertainties. Therefore, proper calibration is an essential part of IceCube. Moreover, for PINGU, even higher precision calibration is needed in order to push the energy threshold down to the target threshold. Therefore, understanding the calibration efforts are important for this study.

IceCube in-situ detector calibration employs reference electronics onboard the DOMs, LED flashers co-located with each DOM, in-ice calibration lasers and low energy muons in the ice for calibration. The main properties to understand and calibrate are geometry, timing, waveform and ice properties. Most of the calibration methods of IceCube will be applied to PINGU. This section discusses the geometry, timing and energy calibration in IceCube. What can be learned from the calibration efforts and how this can be used to improve IceCube-Gen2 will be discussed in 4.1.4.

### 3.3.1 Geometry Calibration

The geometry calibration is divided in three stages, which together lead to an estimate of every DOMs position with a precision of $1\,\mathrm{m}$ in every coordinate [58].

**Stage 1** The first step in determining the geometry mainly uses data gathered during the drilling and deployment of the strings and the DOMs, i.e. non-optical data. By monitoring the precise position of the drill during operation, together with the x-y drift versus the depth of the drill, the first x and y coordinate of the individual DOM positions is determined. The z coordinates are determined by pressure measurements of the lowest DOM. The vertical DOM spacings, which are monitored during deployment, are then subtracted from the depth until the top DOM is reached. This data is then converted to z-coordinates by normalization of the surveyed floor elevation to the origin of the coordinate system. Consequently, Stage 1 results in a set of three-dimensional coordinates for all DOMs.

**Stage 2** In stage 2 the flasher data is used to determine the relative depth offsets between the strings. Typically, the six horizontal LEDs are flashed at a predetermined amount of DOMs on a string, and the up to six adjacent strings are read out. This results in a travel time distribution. By fitting a partial gaussian the prompt time ($t_0 = \mu - \alpha \cdot \sigma$), i.e. the leading edge of the time distribution, is estimated. This consists of 'direct' photons, that have not been scattered. From this the distance between the DOMs, ($d = c_{ice} \cdot t_0$) is calculated. Plotting this against the vertical distance between flasher and receiver ($z' = z_{receiver} - z_{flasher}$) for all triggered DOMs on a string results in a hyperbole. This can be fitted to the hyperbole equation,

$$d = \sqrt{D^2 + (z' - \Delta z)^2}. \tag{3.12}$$

Here, D is the horizontal distance between the two strings, and $\Delta z$ is the string depth offset. Following this procedure iteratively results in a relative offset for every string, resulting in a better estimate of the DOM z-coordinates. This method does not result in an estimate for the horizontal (x,y)-coordinates.

**Stage 3** Stage 3 of the geometry calibration is done over time to track deformation of the DOM array due to ice-shear. The ice at the the surface moves with a velocity of $10\,\mathrm{m/year}$, whereas the velocity at bedrock is zero. The top $2000\,\mathrm{m}$ is estimated to move as a rigid body, and the deeper ice is subject to shear [47]. The shear could cause the deepest DOMs to move $1\,\mathrm{m}$ with respect to the shallowest DOMs. To monitor this, muon tomography is used to determine the coordinates of every DOM over time.

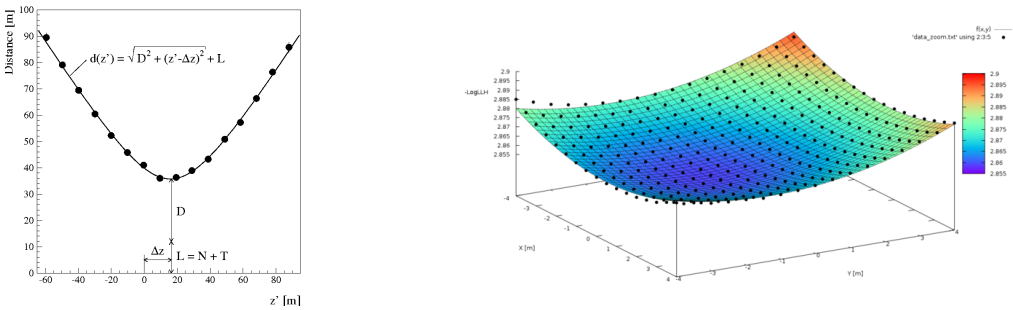


**(a)** *Schematic example of the hyperbola fitted to inter-string flasher measurements [49].* **(b)** *An example of a likelihood surface for DOM 66 on string 15 [48].*

**Figure 3.7:** *Reconstruction methods for stage 2 (a) and 3 (b) of the detector geometry calibration.*

Meaning that radiation from selected muon tracks is used to calibrate every DOM. Fir this purpose, high quality, down going muon tracks that involve a particular DOM are selected after reconstruction. Every DOM is calibrated by excluding measurement data from that specific DOM from the tracks likelihood function as a function of (x,y,z) coordinates. From the resulting track's likelihood a three-dimensional $(x, y, z)$-map is made of the DOMs position. Such a map, for DOM 15 on string 66 is shown in figure 3.7a. The point where the likelihood is at its maximum is the best fit position of the DOM.

An advantage of applying muon tracks over flasher data is that DOMs can be calibrated individually without making assumptions of the string position. A disadvantage of this method is that the calibration relies on the precision of the track reconstruction itself. Therefore, any uncertainty in the reconstruction method propagates to the uncertainty in the calibration.

### 3.3.2 Timing Calibrations

To calibrate the timing of the DOMs and the detector, a procedure called "reciprocal active pulsing" has been devised and implemented. It uses a free running clock, i.e. a free running local oscillator ($20\,\mathrm{MHz}$) and a GPS controlled oscillator at the surface. At known intervals, a fast bipolar pulse is transmitted from the surface to the DOM, which the DOM reciprocates and sends back to the surface after a known delay interval. The waveform arriving at the surface contains the needed information. The waveform is digitized and read out. By comparing the waveform initiated at the surface and the reciprocated, sent back, waveform, the desired information can be derived. This procedure has resulted in a time synchronisation of $3\,\mathrm{ns}$ or better [10].

### 3.3.3 Energy calibration

Energy calibration is essential in understanding and optimizing the reconstruction capabilities of the detector. The precision of the energy reconstruction practically depends on the calibration of the PMT sensitivity, understanding the light propagation in the ice, Poissonian fluctuation in the collected charge and the final energy scale calibration.

### Energy Scale

The energy scale of the detector is an offset in the detected and the actual charge. For IceCube, the final energy scale calibration is based on the detection and simulation of minimum ionizing muons as standard brightness candles. Minimum ionizing muons are suitable sources since the Cherenkov light yield is relatively well understood. A sample of appropriate events is selected based on the conditions:

- The events are low energy single muons, which is characterized by little energy deposition in the outer strings and the track stopping in the fiducial volume.
- The quality of the event reconstruction fit has to be high
- The track has an inclination of 45° to 70° in zenith direction, maximizing the amount of Cherenkov photons hitting the down-facing PMTs due to the typical Cherenkov angle of 41°.

Monte Carlo simulation shows that the sample with these requirements consists of over 95 % single muons, with an average energy of $82\,\mathrm{GeV}$. It has been shown that this agrees with the experimental data [1].

To establish the energy scale with this sample, the focus lies on DOMs in the part of the detector where the absorption length is$\sim$ 200 m or higher. For DOMs in this region, the muon track is reconstructed without including the data gathered by that specific DOM. This leads to a successful reconstruction of the muon within$\sim$ ° direction and the distance between the DOM and the event with$\sim 10\,\mathrm{m}$. By comparing the expected measured charge and the charge that the DOM actually detected, a charge excess is found, as illustrated in figure 3.8a. The average charge excess resulting from this analysis is 5 %, with deviations at some distances to 9 %.

To verify whether this energy scale can be extrapolated to the regime of photon counts at which IceCube operates, the two 337 nm nitrogen lasers are used. These two lasers emit light-pulses that are identical, except for the adjustable intensity in the 1-100 PeV range. Varying the laser amplitude yields waveforms in surrounding DOMs that are scaled copies of each other, as shown in fig. 3.8b. This implies that the energy scale can be extrapolated to the regime of photon counts at which IceCube operates. Any nonlinearity would have appeared as a distortion in this analysis [1].

The measured energy scale of 5% is consequently used to scale measured energies.

### Energy resolution

The energy resolution specifies to which precision the detector can reconstruct energy depositions. Cherenkov light, emerging from energy dispositions of particle interactions in the ice, are measured by the detector. The emitted Cherenkov light is proportional to the total energy that is deposited, from which the energy of neutrinos in CC interactions can be derived. The precision to which the deposited electromagnetic energy can be derived is defined by the energy resolution. In general the energy resolution is defined by:

$$\text{Energy Resolution} = \frac{E_{\text{reconstructed}} - E_{\text{true}}}{E_{\text{true}}} \tag{3.13}$$

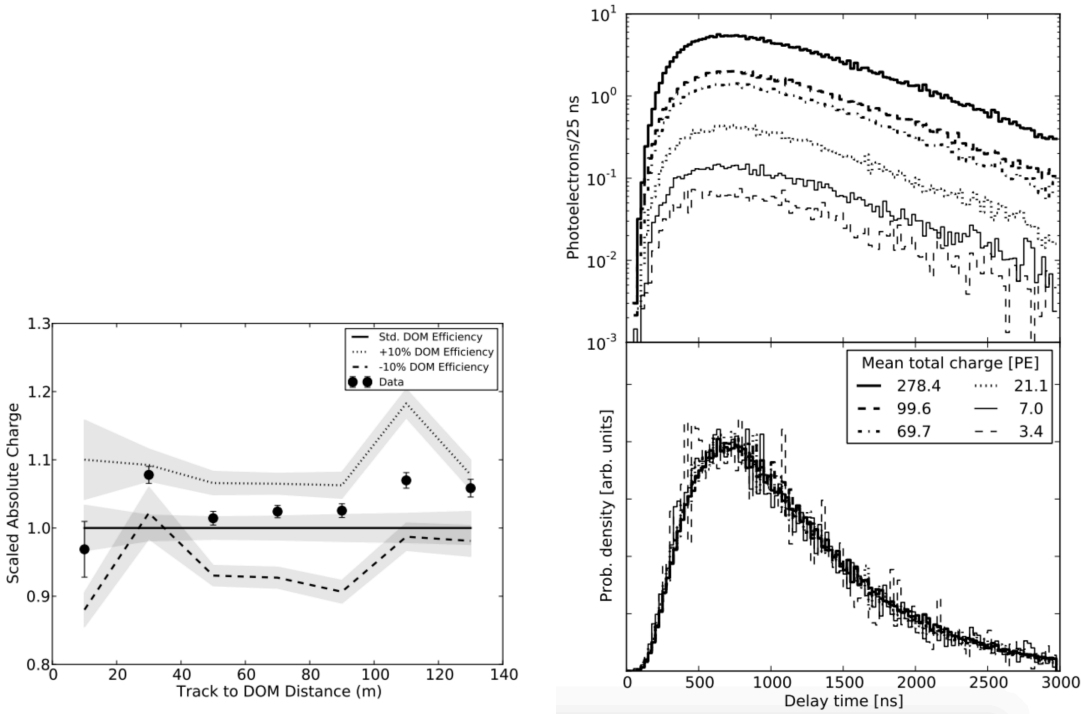


**(a)** *The average observed charge against the distance between the DOM and the minimum-ionizing-muon track, normalized to the charge expected from simulation. The standard DOM efficiency is the expected charge measurement from IceCube simulation. Simulation with an altered DOM efficiency of ±10% with error margins is shown for reference.*

**(b)** *Charge collected from the calibration laser. In the top the charge collected at 6 different laser intensities as a function of time at a distance of 246 m is shown. The bottom graph shows the same distributions, but normalized to the transmitted laser intensities. This verifies the linearity of the energy scales in the energy region at which IceCube operates.*

**Figure 3.8:** *Results of the two stages of energy scale calibration. in **(a)**, the minimum-ionizing-muon analysis. In **(b)**, the linearity verification using the two in-ice 337 nm lasers. [1]*

From the analysis of simulation and experimental data, an energy resolution of$\sim$ 15% has been derived for IceCube [1]. Some uncertainties contributing to this resolution are fundamental to the detector's performance. An example of this is the inherent variability of light yield from hadronic cascades. Such uncertainties can hardly be improved. Other uncertainties are due to the models describing the light propagation and shower development, on which the energy calibration is also based. These could be improved by introducing a calibration device such as the POCAM. An isotropic, self-calibrated energy deposition, would circumvent any cascade-inherent uncertainty and could therefore verify, if not improve, both the energy scale calibration and energy resolution.

# Chapter 4

# IceCube-Gen2

IceCube-Gen2 consists of the Precision IceCube Next Generation Upgrade (PINGU), and the High Energy Extension (HEX). The POCAM is originally intended for PINGU. This chapter will introduce the design, intention, physics potential and calibration systems of PINGU. Although not not included in this thesis, the principles of the POCAM could be implemented in HEX as well. Therefore, the chapter concludes with a short discussion of HEX.

## 4.1 Precision IceCube Next Generation Upgrade

PINGU is to be integrated with IceCube, lowering the energy threshold to a few GeV. PINGU will be the world's largest effective volume for neutrinos in this lower energy range. With this lower threshold, a set of new scientific goals can be pursued. The main purpose is to distinguish the nature of the NMH, a theoretical description of the NMH can be found in 1.1.2.

The design of PINGU is based on experience and knowledge gathered by designing, deploying and operating IceCube. Moreover, the software and hardware are to be closely integrated with that of IceCube. Consequently, the design is feasible with a short construction time and low financial cost. The focus on this section is on the differences or additions with respect to IceCube and on those components that are important for the POCAM design.

### 4.1.1 Neutrino detection and Event Reconstruction

PINGU is designed to detect large numbers of atmospheric neutrinos with an energy threshold as low as a few GeV. As can be deduced from the crosssections in figure 4.1, at energies below $10\,\mathrm{GeV}$ Quasielastic scattering (QE) and resonance production (RES) dominate.

For the detection of few GeV neutrinos the important processes are the QE interactions where a lepton $\ell^{\pm}$ is produced [38].

$$\nu_\ell + n \rightarrow p + \ell^- \qquad (CC) \tag{4.1}$$
$$\bar{\nu_\ell} + p \rightarrow n + \ell^+ \qquad (CC) \tag{4.2}$$

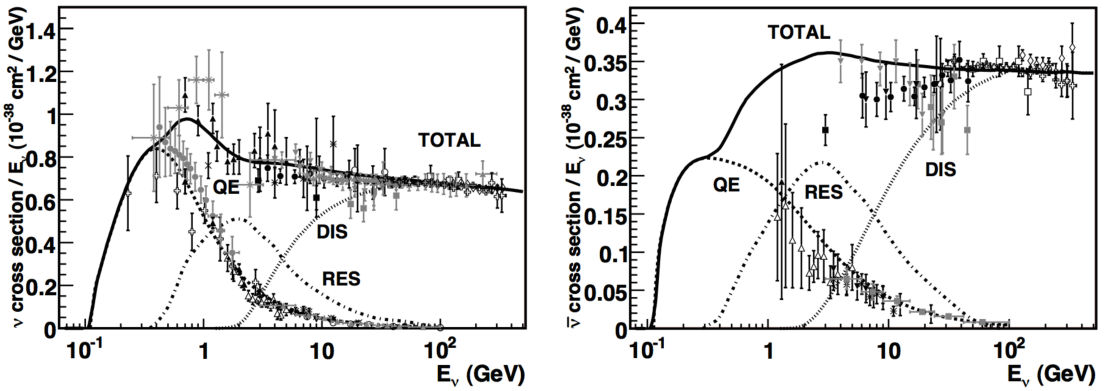


**(a)** *Neutrino cross sections divided by neutrino energy*

**(b)** *Antineutrino cross sections divided by neutrino energy*

**Figure 4.1:** *Neutrino CC cross sections divided by neutrino energy. QE and RES scattering are the dominant processes up to* 10 GeV. *For higher energies DIS processes dominate. Plots taken from [35]*

The resulting leptons induce radiation which can detected by PINGU .

Naturally, the event signatures characterizing the neutrino types ($\nu_e, \nu_\mu, \nu_\tau$), are the same as for IceCube. However, at this lower energy scale, most or all secondary particles induced by a neutrino event will be contained by the detector, whereas in IceCube the majority is only partly contained. Furthermore, at energies below $\sim 100\,\mathrm{GeV}$, the hadronic shower at the the vertex of the neutrino interaction contributes a significant fraction of the Cherenkov radiation which needs to be taken into account in event reconstruction [3].

As a consequence, the event reconstruction strategies will slightly differ from those used in IceCube. This results in different energy and direction reconstruction strategies, the details of which are beyond the scope of this thesis.

### 4.1.2 Physics Potential

With the here discussed geometry and improvements, PINGU will detect the atmospheric neutrino flux, as visualized in 2.3. With the resulting high frequency event detection, a number of scientific goals can be pursued, of which the main ones are:

- The primary goal of PINGU is to determine the nature of the NMH. Due to the MSW effect the earth influences the flavor composition of the atmospheric neutrinos. By gathering a large dataset of atmospheric neutrinos in a relatively short time, the alteration of the atmospheric neutrino flavor composition should show whether the NMH is normal or inverted. The current baseline geometry is intended to enable distinction at the level of 3 standard deviation with 3,5 years of data taking. [58].
- Studying the $\nu_\mu$ disappearance [57].
- Measure $\nu_\tau$ appearance with high precision [58].
- Exclude the maximal mixing of $\theta_{23}$ at the $5\sigma$ level. Additionally, the correct $\theta_{23}$ octant could be distinguished with more than $5\sigma$ when the NMH is normal.

- The earth's core can be probed with neutrino tomography [29].
- Test claims on dark matter annihilation in the Sun, such as the the anomalous annual modulation [23], explore new regions of parameter space that are intrinsically hard to probe [58] and test for dark matter annihilation near the Galactic Center.
- detecting and interpreting low energy neutrino bursts from supernovae [58].

### 4.1.3 Instrumentation

PINGU will instrument a volume of the clearest ice in IceCube, below the dust layer in the central DeepCore volume, as depicted schematically in figure 3.6. In this section the for this thesis most important additions to the IceCube systematics will be discussed.

#### Geometry

Several possible geometries have been investigated for PINGU, with string and DOM numbers ranging from 20 to 40 and 60 to 100, respectively. Simulation results and financial considerations have led to the current baseline geometry consisting of 40 strings with 96 optical modules on each string, as depicted by figure 4.2 .The corresponding vertical inter-DOM spacing is 3 m, with an inter-string spacing of 22 m. With this geometry the energy threshold for neutrinos is estimated to be $\sim 5$ GeV.

Extensive simulation with this geometry has shown that for a 10 GeV $\nu_\mu$ event, approximately 70 photons will be detected by the PINGU-DOMs, after extracting noise induced hits. The energy resolution of this geometry, as defined in equation (3.13) is estimated to be 20%. The angular resolution ($\theta_{\text{true}} - \theta_{\text{reconstructed}}$) is roughly 15% for $\nu_\mu$ CC events. These numbers are estimated with a reconstruction algorithm with an efficiency of 90% [58].

#### PDOMs

The DOMs in IceCube are part of the established, and well functioning, Data Acquisition System. By integrating the PDOMs with the existing infrastructure, effectivity and functionality is ensured. The PDOM will have a couple of improvements with respect to the conventional DOMs.

The outer topology of the PDOMs will be unchanged compared to the current DOMs, including the glass sphere, penetrator, harness and cabling, see figure 4.3. The reuse of these components ensures a cost effective deployment in the challenging South Pole environment. Inside the PDOM some components, such as the PMT, optical gel and mu-metal shield, which have proven to be reliable, remain exactly the same. The main board is slightly altered with respect to IceCube. Although the functionality will remain predominantly the same, the new design is simplified and optimized with up to date electronics. The LED flashers inside the PDOM will be updated, which will be further discussed in section 4.1.4.

Three alternative PDOM designs are under study:

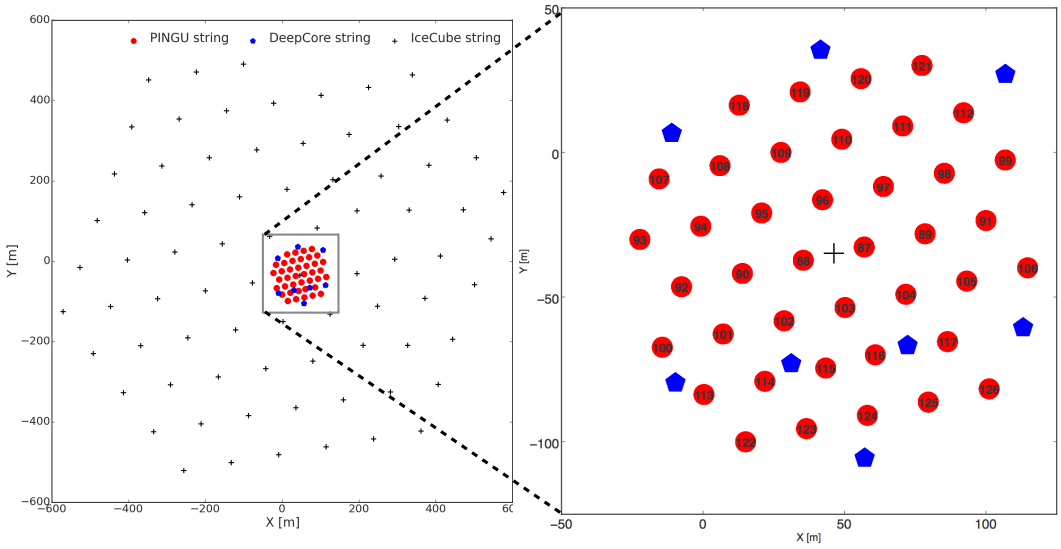


**Figure 4.2:** *Schematic top view of the current baseline geometry of PINGU, consisting of 40 strings with 96 PDOMs each. The strings are numbered from 87 to 127. As visible, the complete geometry is placed inside the Deepcore instrumented volume. The average inter-string spacing is 22 m and the inter DOM spacing is 3 m [58]. For future reference, the strings are numbered 27-126.*

- The multi-PMT Optical Modules (mDOM), which increases the photo-detection sensitivity, directional information, and precision timing by using 24 PMTs of 3" [28].
- Wavelength-Shifter Optical Modules (WOM), which increases the sensitive area of the PMT and improves the quantum efficiency among advantages as a smaller diameter and increased UV-sensitivity [44].
- A Dual PMT optical module (D-Egg) with two 8" PMTs, one facing down, one up, which enhances the angular acceptance accordingly [50]

These modules offer some interesting properties, but are, for now, not implemented in the baseline geometry.

### Cable

Due to improvement in the power design and data compression in the PDOMs, fewer wire pairs are necessary to connect the PDOM to the surface. Therefore, the main cable for the PINGU hardware will differ slightly from the IceCube main cable. This does not only result in significant savings on cost and risk, but also in a smaller diameter for the main cable. The PINGU main cable in the current baseline design has a diameter of 36 mm.

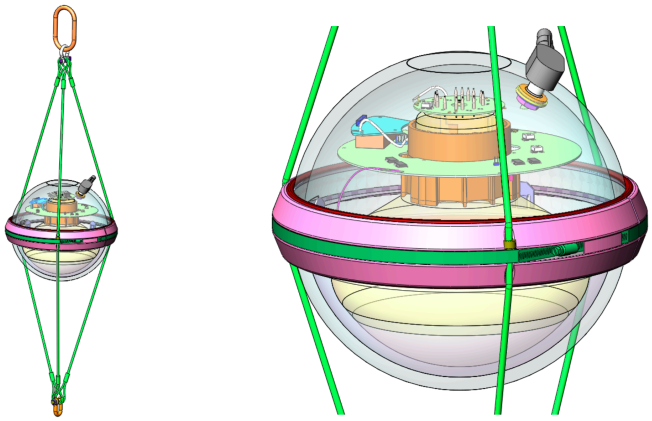

**Figure 4.3:** *Current design for the PDOM [58].*

#### Degassed Hole Ice

As discussed earlier in section 3.2.3, the column of refrozen ice around the strings and DOMs in IceCube has properties that differ from the bulk ice. Where the bulk ice is a slow accumulation of ice, the refreezing of water in the drilled holes takes place in 3 hours, causing dissolved gas to be frozen in the hole ice. These gas bubbles result in a shorter absorption and scattering length close to the DOMs.

For PINGU, a technique named Degassing has been devised. By bringing water to the surface and degassing it before letting it back in the hole, the water will contain 85 % less dissolved air at $1\,\mathrm{bar}$, i.e. $3\,\mathrm{mg/kg}$ in comparison with $20\,\mathrm{mg/kg}$ solubility of air in water. This will only slightly alter the drilling procedure [58]. The remaining effect of gas on the scattering and absorption in both the degassed hole ice as the bulk ice can be studied and calibrated with the LED flasher board, down-going muons and the POCAM.

### 4.1.4 PINGU Calibration Systematics

Event reconstruction with PINGU uses timing, location and amount of measured light to reconstruct the position, time, direction and energy of the detected particle and the neutrino that induced it. The accuracy of event reconstruction relies heavily on the calibration of the detector. The calibration system if PINGU employs the same techniques as IceCube, which is discussed in section 3.3. Naturally, building on the experience acquired with IceCube, improvements are planned. New and significantly improved devices are reviewed in this section.

#### Calibration Devices

**LED flashers** The LED flasher board in IceCube has been of great importance in measuring ice properties, timing, DOM sensitivity, location and orientation of the DOMs, see section 3.2.1. Therefore, the PDOMs will also be equipped with an upgraded LED flasher board.

- Monitoring of the LED light output should increase confidence in the in ice LED characteristics, increasing the control over brightness settings and reducing the uncertainty.
- Research efforts are being made to shorten the LED pulse timing profile. In IceCube the minimum pulse width is 7 ns. In PINGU, the goal is to have a minimum 1 ns pulse width with a Kapustinsky driver [52]. This would significantly improve the precision of LED measurements, since the time behaviour of received light is less dependent of the LED propeties, and more on the ice properties.
- The option to use variable LED wavelengths is under study. This could increase the precision of wavelength dependent studies of ice properties and in ice DOM response [58].

**Cameras** A camera similar to the Swedish camera in IceCube will be deployed with PINGU on at least one string. This camera will enable verification of the effectiveness of degassing the hole ice. Under investigation is the feasibility of deploying more cameras, i.e. a camera on every or a large fraction of the PDOMs. Apart from the main goal of investigating the hole ice, a more extensive camera system could add to the precision of Bulk-ice measurements and geometry calibration. It might, for instance, be possible to determine the azimuthal orientation of the DOMs [3].

**POCAM** As mentioned before, the POCAM is an innovative addition to the calibration systematics of PINGU. The design is discussed in detail in the chapter 5.

#### Geometry, Timing and Energy Calibration

**Geometry** PINGU will use data from the drilling process, pressure sensors on the strings and laser measurements during deployment to determine the position of the DOM. Using in-situ light sources, such as the LED-flashers and the POCAM, the position can be further corrected with triangulation. In IceCube the similar processes resulted in a precision of $1\,\mathrm{m}$ in every coordinate, see section 3.3.1. Studies to determine how much PINGU can improve on this are underway [58].

**Timing** PINGU will employ a system similar to that described in section 3.3.2, using reciprocal pulses between clocks on the surface and in each DOM. Furthermore, small offsets in each PMT will be measured with in-situ light sources, such as the LEDs and the POCAM, that have independent timing.

**Energy** The methods used in IceCube to determine the energy scale and the energy resolution will be employed for PINGU as well. These methods are mainly based on low energy muons, as described in section 3.3.3.

The POCAM is designed to verify the energy scale and energy resolution. As an isotropic, self-calibrated energy deposition any cascade-inherent uncertainty can be circumvented. Therefore with the POCAM, the the energy scale calibration and energy resolution can be verified, if not improved.

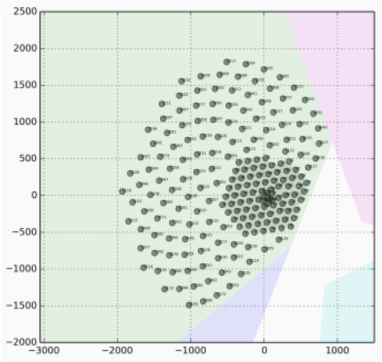


**(a)** *Top view of one of the possible HEX geometry under study. 120 strings are added to the "Dark Sector", where the absorption lengths are longest. In this figure, a string spacing of 240 m is shown.*

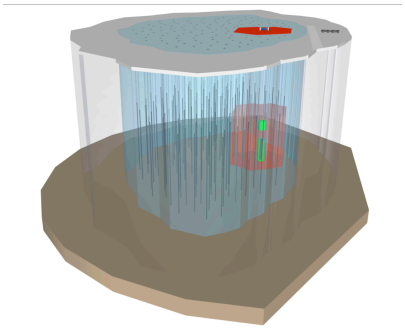

**(b)** *Schematic of IceCube-Gen2. IceCube is shown in red, DeepCore in green, PINGU as the low energy extension in grey.*

**Figure 4.4:** *The current design of the High Energy Extension of IceCube. in* ***(a)*** *is one of the geometrical designs currently under study. For this design, string spacings of 300 and 400 m are also under consideration. These strings would increase the instrumented volume to* $6.0\,\mathrm{km}$, $8.0\,\mathrm{km}$ *and* $11.9\,\mathrm{km}$, *respectively. In* ***(b)*** *the full IceCube-Gen2 geometry is shown.*

**Ice Properties** Measurements of bulk ice properties in IceCube have shown that absorption and scattering length of the ice depend heavily on dust concentrations. Therefore the properties are highly location dependent. At the depths where PINGU will be deployed, the scattering and absorption lengths are the longest in IceCube, with typical values over $25\,\mathrm{m}$ and $100\,\mathrm{m}$, respectively. The precision of the scattering and absorption lengths in the current ice models, based on LED flasher measurements as described in 3.2.4, is 10 %. Additionally, there is a 10 % uncertainty due to a difference in simulated and actually deposited charge by the LED flashers. The POCAM could circumvent this uncertainty, by being in-situ monitored. Therefore, the POCAM and improved LED flashers, could improve the precision of the bulk ice models.

The properties of the degassed hole ice around the PDOMs can be studied with the in-situ light sources and low energy muons [5].

## 4.2 The High Energy Extension

Apart from PINGU, IceCube-Gen2 consists of HEX. The basic idea for HEX is to increase the detector volume with an order of magnitude, from $1\,\mathrm{km}^3$ to $\sim 10\,\mathrm{km}^3$, by placing strings with large spacing around IceCube. Several geometries are currently under study, one of which is shown in figure 4.4. String spacings range from 200 to 300 m, with instrumented volumes ranging from $6.0\,\mathrm{km}^3$ to $11.9\,\mathrm{km}^3$.

With detector volumes of this scale, neutrinos with energies up to the PeV scale can be studied in detail. The point source sensitivity is estimated to increase by a factor 5. Apart from the sensitivity to even higher events, the sample of high energy neutrinos will increase significantly. The measurements on spectral and flavor compositions with a larger data-set can result in interesting insight in cosmic accelerators. Other scientific

goals that can be pursued with HEX are the soectral and flavor characterization of astrophysical neutrinos, Cosmic ray studies and searches for signatures of beyond the standard- model physics [7].

# Chapter 5

# Precision Optical CAlibration Module

The discussed calibration techniques and systematics in section 3.3 have shown to be sufficient for the detection of high energy neutrinos in IceCube. Nevertheless, to reach the desired threshold energy of a few GeV for PINGU, calibration uncertainties need to be improved with respect to the current detector. The current in-situ calibration is predominantly based on the flasher board in each DOM. This will also be implemented in PINGU, but could be complemented with a source that overcomes some of the current limitations. Two main uncertainties in the current flasher board systematics are 10 % uncertainty in the LED intensity output, and a $\sim$ 10% uncertainty in the LED position due to possible azimuthal rotation of the modules during deployment.

A way to circumvent the aforementioned limitations, is to add a self-monitored, isotropic light source to the calibration systems of PINGU, and to HEX as well (after re-opimization). Such a module would open the possibility to verify the energy scale and the energy resolution of atmospheric neutrinos detected in PINGU and could also add precision to the calibration and measure both the bulk and the hole ice properties to higher precision.

The here proposed module has been named the Precision Optical CAlibration Module (POCAM). This optical module applies the basic principles of an integrating sphere to isotropize the light from an internal light source. One, or several, of such modules should be placed on a central cable in the PINGU geometry.

In this chapter, the design goals of the POCAM are specified. Subsequently, the dedicated Geant4 simulation, with which the design has been optimized, will be introduced. This is the main contribution of my work to the POCAM design study. Therefore the results of these efforts are discussed in detail in chapter 6.

## 5.1 Design goals

The design study of the POCAM consists mainly of varying several parameters in a simple initial design to find an ideal balance in pulse and hardware characteristics. I have contributed to set up a dedicated Geant4 simulation to test and optimize the large amount of geometrical parameters. Altogether, the specific design goals of the POCAM can be summarized as follows.

• Homogeneous illumination of the instrumented ice volume. Homogeneous refers to the angular distribution of photons on a sphere. Homogeneity in azimuth angle takes precedence over homogeneity in zenith angle. The aim is to keep inhomogeneities in azimuth angle at the level of 1%.

• The emission of the POCAM has to illuminate at least the whole PINGU ice-volume, so that every DOM is able to measure at least one photoelectron.

• The POCAM light pulse has to be fast, with a rise time of a few ns, with an as low as possible decay time $\tau$ and a high peak. The rise time is mostly dependent of the internal light source, but could be influenced by the geometry. The decay time and the high peak will depend more strongly on the POCAM geometry.

• The module is self-monitoring. The emission and pulse characteristics needs to be in-situ monitored to great precision.

• The design should utilize techniques and material that are known to IceCube, as to build on experience acquired through IceCube. This ensures efficient design, implementation and deployment.

With the aforementioned characteristics the POCAM should be able to verify the energy scale calibration and energy resolution of PINGU, measure the absorption and scattering lengths of the Antarctic ice at a level better than 10 % and enable precise measurement of hole-ice properties.

## 5.2 POCAM Components

The initial design of the POCAM consists of a number of basic components, the properties of which are discussed in this section. Fig. 5.1 shows a visualization of the basic design with all components.

### 5.2.1 Outer Topology

Because the integrating sphere and the necessary electronics need to be separated from the Antarctic ice in order to protect it from the external pressure, a spherical housing shapes the outside topology. Building on the successful design of IceCube DOMs, we plan to use the exact outer topology as for the conventional DOMs.

The outer topology consists of a $0.5$” $(1.3\,\mathrm{cm})$ thick borosilicate glass pressure vessel, with a radius of $16.5\,\mathrm{cm}$, able to withstand a pressure of $70\,\mathrm{MPa}$. It transmits light with a wavelength longer than $350\,\mathrm{nm}$ [15]. This Vessel consists of 2 half spheres that are held together with optical coupling gel, a band of black tape and the Harness, which attaches the module to the main power cable.

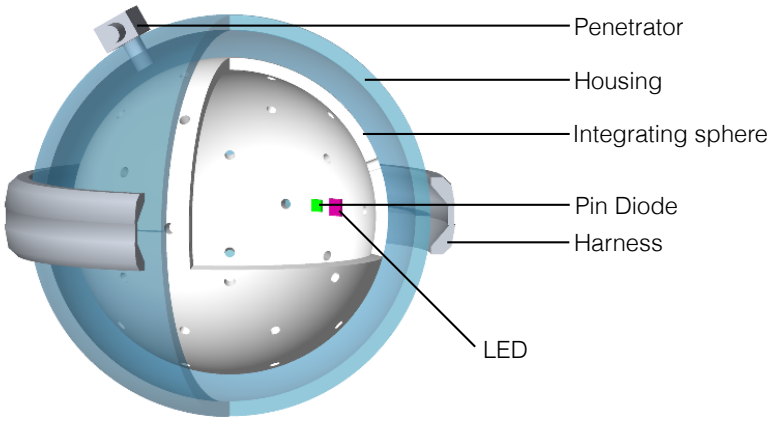


**Figure 5.1:** *Visualization of the Precision Optical CAlibration Module simulation with* $24\,\mathrm{cm}$ *diameter 48-port integrating sphere. The separate components are named.*

Additionaly, the penetrator leads the necessary cables from the main cable to the hardware inside the pressure vessel [15]. The penetrator and the harness assembly are necessary for the POCAM to function in the ice, but will cast a shadow in the POCAM's emission. This necessary perturbation should be minimized and is an important part of the design study.

### 5.2.2 Light Source

A possible realization of the light source is a matrix of LEDs with wavelengths ranging from 370 to 500 nm. The LEDs need to be able to emit short pulses, with an as short as possible rising time. The LEDs will therefore be driven by a Kapustinsky circuit, which can create pulses of few nanoseconds Full Width Half Maximum (FWHM) and up to $10^9$ photons per pulse. The Kapustinsky circuit is acclaimed and finds application in several astroparticle physics experiments [12, 65].

The position of the light source and its characteristics will be of major importance to the time - and emission profile of the POCAM. The position and emission profile of the LEDs influence the homogeneity of the emission. An ideal placement and emission profile of the LEDs minimizes this effect.

### 5.2.3 Integrating Sphere

Creating an isotropic light source is a non-trivial task.

The integrating sphere is responsible for creating an isotropic light emission. Integrating spheres are a common instrument in radiometry. Their conventional function is not to create an isotropic signal, but to spatially integrate incident flux. Where a conventional integrating sphere integrates a beam incident through an opening in the sphere, the integrating sphere of the POCAM diffuses the directional information of a beam from an internal light source.

To properly simulate and apply an integrating sphere, a fundamental understanding of the basic principles is needed. Photons, emitted from an internal light source, reflect

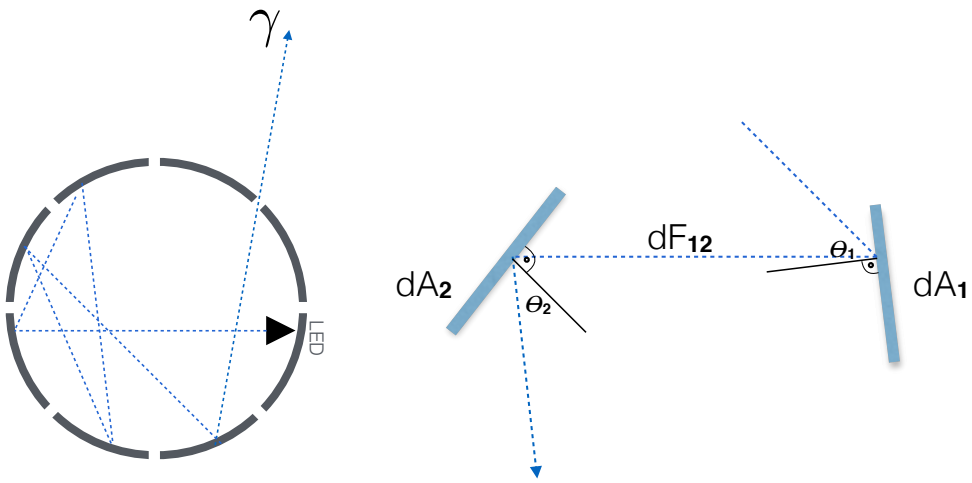


**(a)** *The principle of the integrating sphere relies on the lambertian reflection and the symmetrical properties of the sphere to isotropize the photon beam from the LED*

**(b)** *The radiation exchange $dF_{12}$ between two infinitesimal lambertian surfaces, as in equation 5.1. $\theta_1$ and $\theta_2$ are the angles of the radiation with the surface normals.*

**Figure 5.2:** *Schematics describing the principles of the integrating sphere*

several times on the lambertian reflecting inner surface of the sphere. After a number of reflections, the photon leaves the sphere. At this time, all original directional information of the photon is lost. This principle is visualized in 5.2a. A material commonly used as a diffusor is PTFE [74]. In the prototyping phase, this material needs to be tested, but for now we will assume perfect lambertian reflection, with a reflection coefficient of $\sim 99$ %. In the design of the POCAM, two types of integrating sphere have been tested. The sphere either has several ports in the sphere or is semi-transparent. The amount of ports and the transparency are parameters that will greatly influence the POCAM characteristics. Simulation and prototyping should optimize both options and show which one results in better characteristics.

Naturally a more precise description of the integrating sphere is necessary. Therefore, a step by step analytical description of the (reverse) integrating sphere is given in the following subsection.

### Analytical Description of the Inverse Integrating Sphere

Considering two infinitesimal lambertian surfaces $A_1$ and $A_2$, as in 5.2b, the radiation exchange between them is described by

$$\mathrm{d}F_{12} = \frac{\cos\theta_1 \cos\theta_2 \mathrm{d}A_2}{\pi S}. \tag{5.1}$$

Here, $S$ is the distance between the two surfaces, $\theta_1$ and $\theta_2$ are the angles of the beam with the surface normal.

Applying equation 5.1 to the internal surface of a sphere, the symmetry implies that $\theta_1 = \theta_2 = \theta$ and $S = 2R\cos\theta$, simplifying equation 5.1 to

$$\mathrm{d}F_{12} = \frac{\mathrm{d}A_2}{4\pi R^2}. \tag{5.2}$$

This shows that the radiant flux received by area $dA_2$ is independent of the photon beam's inclination. Therefore, $dA_2$ receives the same fraction of flux from every radiating point on the surface, which is the basis for the properties of the integrating sphere.

When the right hand side of equation 5.2 is integrated over the port surface $A_2$, it becomes

$$F_{12} = \frac{1}{4\pi R^2}\int_{A_2} \mathrm{d}A_2 = \frac{A_2}{A_s}, \tag{5.3}$$

where $A_s$ is the full inner sphere surface. Therefore, the radiant flux received by surface $A_2$ is simply the fraction of sphere area $A_s$ it occupies [69].

The multi-port configuration with $n$ ports, each consuming an area $A_{port}$ of the sphere surface $A_s$ made of PTFE has an effective transparency of

$$T = \frac{n \cdot A_{\text{port}}}{A_{\text{s}}}. \tag{5.4}$$

We now consider a light source inside the integrating sphere with a photon flux output $\phi_0$. Ideally, the beam from the light source does not illuminate a surface with ports, preventing photons being emitted from the sphere before reflecting. With reflectivity $\rho$ of the sphere, after the first reflection the reflected flux inside the sphere is $\phi_0\rho$, and the absorbed flux is $(1-\rho)\phi_0$. At the second reflection, $\rho\phi_0$ is split up in three fractions, $F_{1,\text{refl.}}$, which is reflected by area $(1-A)$, $F_{1,\text{abs.}}$ which is absorbed by area $(1-A)$, and $F_{1,\text{trans.}}$ leaves the integrating sphere through the ports with total area $A$;

$$F_{1,refl.} = \phi_0\rho(1-T) \tag{5.5}$$
$$F_{1,abs.} = \phi_0\rho(1-\rho)(1-T) \tag{5.6}$$
$$F_{1,trans.} = \phi_0\rho T. \tag{5.7}$$

At the third reflection $F_{1,refl.}$ is similarily split up in $F_{2,refl.}$, $F_{2,abs.}$ and $F_{2,trans.}$. Iterating this with $n$ reflections results in a total reflected flux of

$$\begin{aligned} F_{\text{refl.}} &= \phi_0\rho(1-T) \;+\; \phi_0\rho^2(1-T)^2 \;+\; \ldots \;+\; \phi_0\rho^n(1-T)^n \\ &= \phi_0\rho(1-T)(1 \;+\; \rho(1-T) \;+\; \rho^n(1-T)^n) \\ &\xrightarrow{n\to\infty} \frac{\phi_0\rho(1-T)}{1-(\rho(1-T))}, \end{aligned} \tag{5.8}$$

a total absorbed flux of

$$\begin{aligned} F_{\text{trans.}} &= \phi_0\rho(1-\rho)(1-T) + \phi_0\rho(1-\rho)(1-T)^2 + ... \\ &\quad + \phi_0\rho^{n-1}(1-\rho)(1-T)^n \\ &= \phi_0\rho(1-\rho)(1-T)(1 + \rho(1-T) + \rho^n(1-T)^n) \\ &\xrightarrow{n\to\infty} \phi_0\rho\frac{(1-\rho)(1-T)}{1-\rho(1-T)} \end{aligned} \tag{5.9}$$

and a total transmitted flux of

$$\begin{aligned} F_{\text{trans.}} &= \phi_0\rho T + \phi_0\rho(1-T)T + ...\phi_0\rho^n(1-T)^nT \\ &= \phi_0\rho T(1 + (1-T) + ... + \rho^n(1-T)^n) \\ &\xrightarrow{n\to\infty} \phi_0\rho\frac{T}{1-\rho(1-T)}. \end{aligned} \tag{5.10}$$

It should be noted that the total incident flux $F_{\text{refl.}}$ is the sum of the flux after each reflection. Therefore, this is higher than the initial flux $\phi_0$. The total flux $F_{\text{trans.}}$ is the flux emitted from the $n$ ports of the integrating sphere. Naturally, the emitted and absorbed flux together is the original flux.

$$F_{\text{trans.}} + F_{\text{abs.}} = \phi_0\rho \tag{5.11}$$

We can similarly derive these equations for a semi-transparent integrating sphere without holes. As will be shown later, for such an integrating sphere it is better to use a wide opening angle for the internal light source. The initial flux in this derivation is therefore $\phi_0$, instead of $\phi_0\rho$. Consequently the total fluxes differ only with a factor $\rho$ from 5.8, 5.9 and 5.10.

Another quantity that we can derive here is the radiance. In general, the radiance, $L$, of a diffuse surface $A$, illuminated by a flux $\phi$, is

$$L = \frac{\phi\rho}{\pi A} \qquad [Wm^{-2}sr^{-1}] \tag{5.12}$$

with $\pi$ the total projected solid angle of the surface.

We can similary express the radiance from a semi-transparent integrating sphere area as

$$L = \frac{\phi\rho T}{1-\rho+\rho T}\frac{1}{n\pi TA}. \tag{5.13}$$

For the multi-port integrating sphere, due to the geometry, the radiance from a single port results in more cosine-like profile.

For both a semi-transparent and a multi-port integrating sphere the photon output $N_\gamma$ will decay exponentially [69] from the peak $N_0$ at time $t_0$, which depends mainly on the LED pulse properties.

$$N_\gamma(t) = N_0 e^{-(t-t_0)\lambda}, \tag{5.14}$$

with $\lambda$ the decay constant and $\tau = \frac{1}{\lambda}$ the exponential time constant.

### 5.2.4 PIN Diode

For the POCAM to contribute to a higher precision calibration of PINGU, it is essential that its in-situ output is well understood. A fast solid state detector, such as a PIN diode [30] or a silicon photomultiplier is to be implemented in the POCAM. It is placed on the integrating sphere to monitor the radiance of a hole or surface with a precision of about 1 %. Ideally, every port of the multi-port integrating sphere, or every spherical element for the semi-transparent integrating sphere, will emit the same radiance (see equation 5.13). Simulation and prototyping will show an optimal placement of this element.

## 5.3 POCAM Simulation

### 5.3.1 Geant4 Simulation

To study the influence of the aforementioned fixed and variable parameters on the emission and time profile of the POCAM, a GEometry ANd Tracking (Geant4) [13] simulation has been implemented. Geant4 is a common and acclaimed toolkit in high energy physics and Cherenkov detectors. Geant4 consists of a set of functions in C++ code, which enables the user to define geometries and their specific optical properties. A photon or particle source can subsequently be implemented, from which it then simulates the propagation of particles through the defined geometry. In this section the Geant4 simulation of the POCAM will be introduced. In chapter 6 the simulation results will be discussed.

As introduced in the previous section, the POCAM is aimed to create an isotropic and fast light signal, which is monitored in-situ, inside the established outer topology of the conventional DOM. In Geant4 this translates to the following basic geometry components, also depicted in fig. 5.3:

- **World Volume** This is an obligatory definition in Geant4. It is the geometrical volume in which all other components are defined. This volume is a sphere with variable radius. The optical properties are those of clear ice with a refractive index of $n_{\text{ice}} = 1.32$ with a density of $0.9167\,\text{g/cm}^3$.
- **Detection Volume** The detection volume is a sphere with a radius of $40\,\text{cm}$, which is adjustable when necessary. The properties of photons hitting this reference sphere are saved in a HDF5 table, a hierarchal data format suited for storing large amounts of data [43].
- **Glass Pressure Sphere** The housing consists of a glass sphere, with an inner radius of $15.25\,\text{cm}$ and an outer radius of $16.5\,\text{cm}$. The refractive index is 1.48. The absorption length is wavelength dependent and is modelled on measurements [31], shown in fig. 5.4. Using Beer-lambert law the measured transmission fractions can be converted to absorption lengths, which is the quantity needed

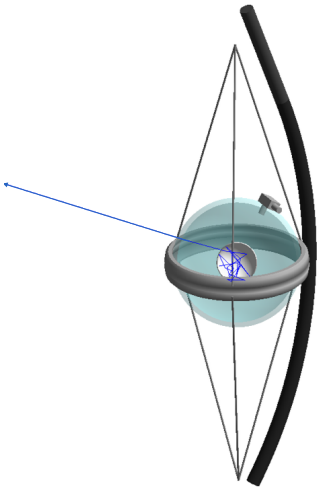

**Figure 5.3:** *Visualization of all components in the Geant4 simulation. Shown is a photon that is emitted from the LED, is reflected a number of times and then leaves the, in this case, semi-transparent integrating sphere.*

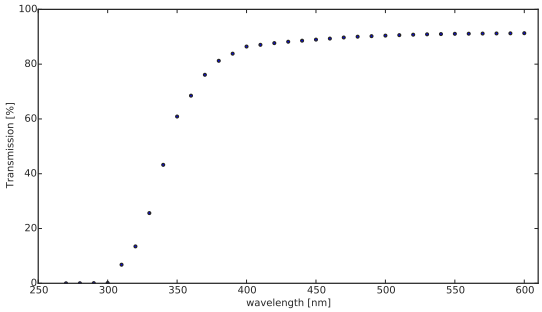


**Figure 5.4:** *Transmission lab measurements of the IceCube DOM glass housing. Data acquired from [46]. This data is used to define the absorption length of the glass sphere in the simulation.*

for the simulation input

$$P = \frac{I}{I_0} = e^{\frac{-z}{\lambda}}, \tag{5.15}$$

from which follows that we can calculate absorption length $\lambda$

$$\lambda = -\frac{z}{ln(P)}. \tag{5.16}$$

Here, z is the thickness of the glass sphere, $P$ is the fraction of measured light intensity $I$ and emitted light intensity $I_0$.

- **Harness** The Harness is modelled as a polygonal cone, fitting tightly around the glass housing. The maximum outer radius is $18.51\,\mathrm{cm}$. The harness is made of aluminium, which is programmed to absorb any photon hitting it.
- **Penetrator** The Penetrator guides the necessary cables through a hole in the glass sphere. It consists of a union of a ($2.7813\,\mathrm{cm} \times 1.524\,\mathrm{cm} \times 1.143\,\mathrm{cm}$) box and two cylinders, with radii $0.80\,\mathrm{cm}$ and $0.79\,\mathrm{cm}$, respecting the properties of the IceCube

penetrator. The material is aluminium, with 100% absorption.

- **Photon source** In the simulation, a standard $405\,\mathrm{nm}$ LED is simulated as a small box from which a beam is emitted. The beam has a Gaussian $405\,\mathrm{nm}$ wavelength, cosine law angular distribution and a rectangular 10 ns timing distribution. The matrix of LEDs with a wider range of wavelengths is to be implemented, but is not included in this study.
- **Monitoring pin diode** It is essential for the POCAM to be self-calibrated. i.e. the light output needs to be monitored in-situ. Therefore a PIN diode needs to be placed either over a port, or on the outside of the semi-transparent integrating sphere. At this point, the PIN diode is just a small geometry, not making a significant contribution to the simulation. Nevertheless, the diode is important and needs to be studied in more detailed at a later stage.
- **Hanging assembly and main cable** The hanging assembly attaches the POCAM to the main cable. It is connected to the harness. The geometrical properties are based on the DOM hanging assembly [53]. The main cable is an aluminium cable with a diameter of $36\,\mathrm{mm}$. The material of both is all absorbing aluminium. Including the hanging assembly and main cable in the simulation is optional, in order to study the simulation with and without the shadow of the hanging assembly.
- **Integrating sphere** For the integrating sphere there are two possible geometries. Both options apply the lambertian properties of PTFE. PTFE is widely used in radiometry for its nearly perfect diffusing property, its constant optical property over a wide range of wavelengths and its constant characteristics over a temperature range of $-50°\mathrm{C}$ to $250°\mathrm{C}$. The reflectivity of the material is $\sim$99%. The material is essentially a lambertian reflector due to a large density of randomly distributed small pores throughout the material. The standard pore size, as provided by [74], ranges from 1 to $20\,\mu\mathrm{m}$ with an average of $6\,\mu\mathrm{m}$. A thin sheet of PTFE ($<1\,\mathrm{cm}$) functions as a lambertian transmitter and reflector, i.e. both the transmitted and reflected light follow lambert's cosine law, the fraction transmitted and reflected is defined by the thickness of the sheet [74]. The two configurations are:
  - A multi-port integrating sphere, made of PTFE. With a thickness of $1.0\,\mathrm{cm}$ the PTFE layer reflects almost al photons, reflectivity is 0.995 %, the remaining 0.005 % of photons is absorbed. The ports are defined with the HEALPix [40] algorithm, which divides a sphere in exactly equal area quadrilaterals. The amount of pixels, i.e. the resolution of the grid is defined by the parameter $N_{side} = 1, 2, 4, 8$. The number of pixels is defined by $N_{pix} = 12 \cdot N_{side}^2$. The centers of these are all equidistant in zenith angle and placed on $4 \cdot N_{side} - 1$ rings of constant latitude. and have a variable radius, $R_{port}$. The ports have an opening angle $\alpha$. This variable strongly influences the emission characteristics in the simulation. The thickness of the integrating sphere is set to an idealized $1\,\mathrm{mm}$ when not declared otherwise.
  - A semi-transparent integrating sphere. A PTFE layer thinner than $1\,\mathrm{cm}$ is typically semi-transparent. Diffuse transmission is not available in GEANT4. By modifying the source code an option was created to make a material

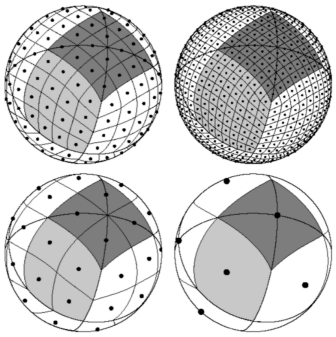

**Figure 5.5:** *Examplary HEALPix partitions of a sphere.* $N_{side} = 1, 2, 4, 8$, *resulting in* $N_{pix} = 12, 48, 192, 768$ *pixels. The pixel centers lie on* $4{*}nside-1$ *rings of equal zenith angle.*

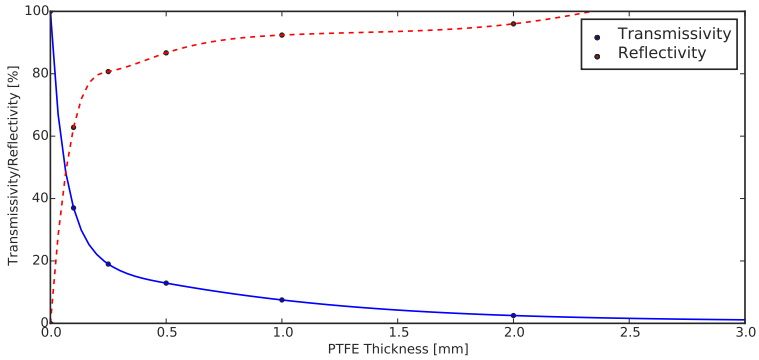


**Figure 5.6:** *Approximation of optical PTFE reflectivity and transmission values for* $405\,\mathrm{nm}$ *light. Based on measurement data provided by [69]. Only the 1 and 2 mm reflectivity data points are from measurement. To compensate for the small amount of Reflectivity measurements, linear progression of absorption values are assumed. More laboratory measurements are needed to increase the accuracy.*

semi-transparent. The reflectivity ($P_{\text{refl.}}$) and transmissivity ($P_{\text{trans.}}$) are defined with adjustable fractions, what remains defines the absorption ($P_{\text{abs.}}$).

$$P_{\text{abs.}} = 1 - P_{\text{trans.}} - P_{\text{refl.}} \tag{5.17}$$

Using measurement data provided by [74] realistic values can be approached to first approximation. In fig. 5.6, the provided data is shown, with a fitted curve for interpolation purposes.

PTFE is notoriously hard to simulate, because any irregularity in the surface will have consequences for the diffusive property. Therefore, it is essential to verify simulations of the semi-transparent PTFE with laboratory measurements which are ongoing.

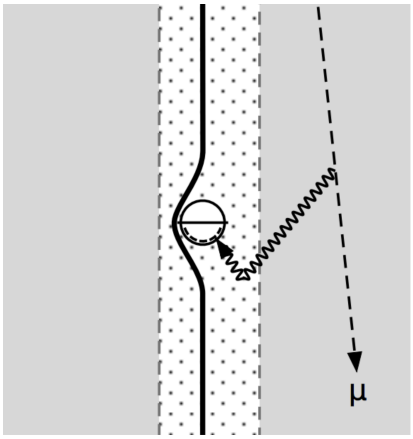


**Figure 5.7:** *The hole ice properties differ from those of the bulk ice. The shorter scattering length causes a number of downgoing photons to be detected, as illustrated. This is translated to a larger angular acceptance in simulation.*

### 5.3.2 CLsim

In order to test the functionality of the POCAM in the actual detector, the Geant4 simulation has been implemented in the photon propagation simulation specific for IceCube and Gen2, called CLsim [55].

CLsim is an open-CL based [70] photon tracking simulation. As discussed in sections 3.3 and 4.1.4 calibration of IceCube and PINGU relies heavily on simulation, of which CLsim is an important element.

Where conventional photon tracking software samples arrival time distributions of photons using look-up tables, relying on interpolation methods that have shown to have considerable drawbacks, CLsim is able to track every single photon individually. The time consuming nature of such processes is covered by using Graphic Processing Unit (GPU) - instead of Central Processing Unit (CPU) hardware.

CLSim generates and propagates photons from a source through the ice until they hit an optical module or leave the detector volume. Sources can be a particle track or a static artificial source, e.g. a flasher or the POCAM. The properties of the ice, i.e. the scattering and absorption lengths, are specified in ice models, as described in section 3.2.4. The hole ice is currently modelled by adjusting the angular acceptance of the DOMs. Figure 5.7 illustrates how the short scattering length of the hole ice effectively increases the angular acceptance.

Photons that hit the DOM surface are then converted into hits and photoelectrons using a dedicated module. The photoelectrons per DOM are then saved in the conventional IceCube data structures. The DOM hits as well as the photon paths can be visualized in an event viewer. Figure 6.13 shows a POCAM event in the event viewer.

### Ideal POCAM Approximation

As a first step, a perfectly isotropic point source has been placed in the simulation to investigate the potential of an ideal POCAM [56]. This simulates a light source on string 88 4.2, one of the central Strings in the current baseline PINGU geometry. For this 'ideal' POCAM, the wavelength spectrum is based on lab measurements of IceCube LED flashes, the direction is randomized over $4\pi$. The time profile is a delta-like pulse around $t = 0$. Typically, per pulse between $10^6$ and $10^8$ photons are emitted per pulse, corresponding to a deposited energy between $6\,\mathrm{GeV}$ and $6\,\mathrm{TeV}$ [56]. For now, a conservative saturation number of 35 photoelectrons, based on the limited dynamic range of the PINGU DOMs, has been set.

As a part of my thesis work, I expanded this to a more realistic simulation of the POCAM in CLSIM, by devising a method to propagate the photons from the hdf5 tables, i.e. from the Geant4 simulation output, through the detector.

### Realistic POCAM Implementation

To approach a realistic POCAM output, the Geant4 photon output can be used as input for an artificial source in CLsim.

The simplest way to implement this is to directly assign the wavelength, emission time, position at which the photon leaves the POCAM, and direction of momentum in the HDF5 table to a CLsim pulse individually.

However, this has shown to work for an amount of pulses up to $5 \times 10^7$ , when crossing this limit, the simulation runs into memory issues. Therefore, an alternative simulation method has been developed, circumventing the memory problem by generating less pulses consisting of more photons. Naturally, the hdf5 table can not be used as direct input in this approach. Instead, the photon data is divided in HEALpix-bins based on the direction of the photon. Consequently, the information in each bin is applied to generate a CLsim pulse. Each pulse consists exactly of the amount of photons in the corresponding bin. For the position, direction, timing and wavelength some approximations have to be made.

- **Position** The position where the pulse leaves the POCAM and enters the ice is the center of the associated HEALpix bin.
- **Direction** The direction of the pulse is modelled with a Gaussian in zenith and azimuth angle. The central direction is perpendicular to the surface of the POCAM at the position of that particular bin. The variance in both angles is calculated from the data in the bin.
- **Timing** The time of hitting the reference sphere in the HDF5 table is used to create a time profile per beam. The maximum of this profile and the FWHM are extracted and used to characterize the time profile of the CLsim pulse. This method was originally intended to generate a LED-flasher time profile. Therefore, the precision needs to be quantified and if necessary enhanced.
- **Wavelength** The wavelength of the pulse is for now sampled from measured profiles of $405\,\mathrm{nm}$ LEDs. In the prototyping phase of the POCAM, optionally new profiles from POCAM measurements can be implemented in the simulation.

The CLSim POCAM simulation consists of 2 parts. First, with the python file called 'generatePOCAMtest.py' the hdf5 Geant4 table is converted to the conventional IceCube software structure with the aforementioned properties per HEALPix bin.

In the second step, using 'applyPOCAMTest.py', the photons are propagated through the IceCube geometry, including PINGU and DeepCore. Two parameters need to be set in this step. The first parameter defines the ice model to be used. The second defines the number of runs, i.e. how many POCAM flashes are to be simulated. For every flash the with 'applyPOCAMtest' defined photon source is used, but the propagation is randomized, resulting in different photon paths. Additionally, an option can be set to save the photon paths. When a photon path intersects a DOM, the photon is saved as a measured photoelectron. This data is saved in the conventional IceCube data structure.

# Chapter 6

# POCAM Simulation Results

The simulation of the POCAM has enabled the optimization of most of the important parameters in the design. The directional and positional distributions of photons on the reference sphere and the corresponding time profiles are the main points of interest in the simulation output. In this section the relevant data is shown. Furthermore, this section describes the important aspects in the optimization of the initial design to which I contributed.

To conclude this chapter the results of the implementation of the current POCAM baseline geometry in the IceCube ray tracing simulation, CLsim, are presented.

## 6.1 Quantity Conventions

Here, the relevant quantities to discuss the results of my work are introduced.

The coordinate system referred to in text and figures is visualized in figure 6.1, with the origin in the center of the module. The zenith angle $\theta$ is always with respect to the z-axis and the azimuth angle $\phi$ with respect to the x axis.

The ports are equidistantly distributed over the integrating sphere as explained in 5.3.1. The ports have an opening angle $\alpha$.

The effective photon transparency is represented by:

$$T = n \cdot \frac{\Delta\Omega_{\text{port}}}{4\pi}, \tag{6.1}$$

with $n$ the number of ports and $\Delta\Omega_{port}$ the solid angle region of one port. For the semi-transparent integrating sphere $T$ is the transparency defined in the simulations.

The inhomogeneity in the shown photon distributions is defined as the ratio of the standard deviation $\sigma$ and the average number of photons in a bin $\bar{N}$,

$$\text{Inhomogeneity} = \frac{\sigma}{\bar{N}} \tag{6.2}$$

Here, the standard deviation is

$$\sigma = \sqrt{\frac{1}{n_k - 1} \sum_{k \in \Delta\Omega} (N_k - \bar{N})^2} \quad . \tag{6.3}$$

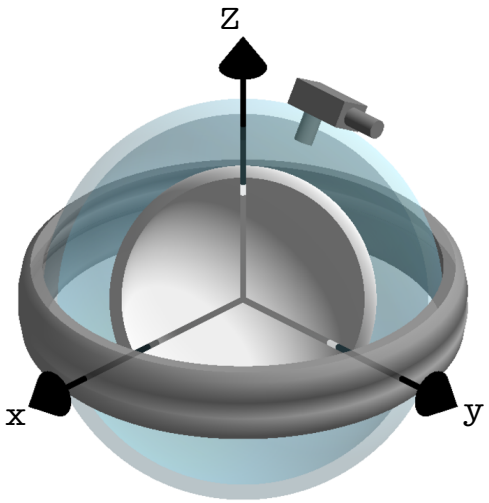


**Figure 6.1:** *Axes orientation as used in the simulation and in the results.*

The average number of photons in a bin is

$$\bar{N} = \frac{1}{n} \sum_{k \in \Delta\Omega} N_k \quad . \tag{6.4}$$

$N_k$ represents the photon count for each bin $k$ lying in the solid angle region $\Delta\Omega$.

This results in a quantity of inhomogeneity expressible as a fraction or a percentage, representing how much the photon count differs over all bins. The inhomogeneity can be expressed for separate solid angle regions, or over the complete sphere.

The absorption $A$ represents which fraction of the photons emitted by the internal light source $N_0$ is absorbed by the geometry.

$$A = 1 - \frac{N}{N_0} \quad . \tag{6.5}$$

Here, $N$ is the number of photons emitted from the POCAM. For now the internal light source is an idealized LED. In the results the internal light source will be referred to as a LED with opening angle $\alpha_{\text{LED}}$.

The time profile of the POCAM show a typical pattern. In the $10\,\text{ns}$ of LED emission, the number of photons increases steadily. After a peak slightly after the $10\,\text{ns}$ the profile shows an exponential decay described by

$$N_\gamma = N_{peak} e^{-\frac{t}{\tau}}, \tag{6.6}$$

where $\tau$ is the exponential time constant.

Unless mentioned otherwise, all simulations presented in this chapter are generated with $10^8$ initial photons.

In figures showing the probability density of photons, e.g. 6.2, the HEALPix algorithm is utilized to create bins of equal solid angle region. Unless mentioned otherwise the parameter defining the number of bins is $n_{\text{side}} = 32$. Figures showing a distribution of HEALPix bins use a 'hammer' projection, which conserves the bin area.

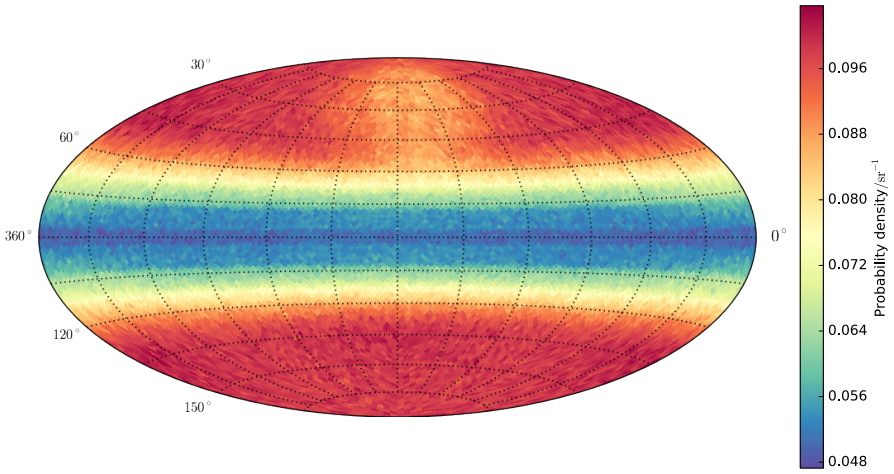


**Figure 6.2:** *Shadow identification in the directional probability density of photons from a* $D = 24\,\mathrm{cm}$*, 768 multi-port integrating sphere. The shadows cast by harness and penetrator are between* $60°$ *and* $120°$ *zenith angle and* $85° < \phi < 215°$ *and azimuth angles* $10° < \theta < 60°$*, respectively.*

## 6.2 Shadow Identification

### 6.2.1 Penetrator and Harness shadow

Figure 6.2 shows the photon emission direction of a $24\,\mathrm{cm}$ diameter multi-port integrating sphere configuration. Two deviating regions are clearly visible in figure 6.2. These are the shadows cast by the penetrator and the harness. The harness shadow region is roughly confined between $60°$ and $120°$ zenith angle. The Luminosity in this region gradually decrease to a minimum at $\theta = 180°$. For this configuration, the luminosity is $\sim$50 % with respect to the no-shadow regions. The penetrator shadow is confined in an area with zenith angle $85 < \phi < 215$ and azimuth angle$10 < \theta < 60$. For this configuration, the luminosity is $\sim$ 25 % lower in this shadow region with respect to no-shadow regions.

## 6.3 Cable and Hanging Assembly Shadow

In figure 6.3 the photon emission direction for a $D = 6\,\mathrm{cm}$ semi-transparent configuration is shown. Here, the cable and hanging assembly are taken into account as described in 5.3.1. The main cable shadow is clearly defined between $-10°$ and $10°$ azimuth angle. In addition the hanging assembly casts an extra shadow at azimuth angles $55° < \phi < 655°$ and $235° < \phi < 245°$, where the probability density is $\sim$25 % lower. With the current goal to use the DOM's outer topology, all shadowing effects are unavoidable. The effect these have on the functionality of the POCAM has to be studied with the ray-tracing simulation.

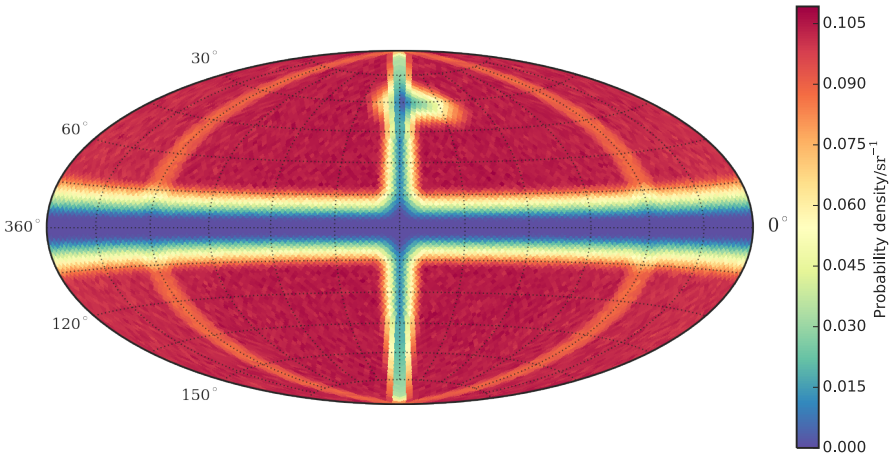


**Figure 6.3:** *Shadow identification in the directional probability density of photons from a* $6\,\mathrm{cm}$ *semi-transparent configuration with main cable and hanging assembly.*

## 6.4 Multi-port Configuration

The simulated configurations are split up in multi-port configurations, discussed in this section, and in semi-transparent configurations, discussed in section 6.5.

### 6.4.1 LED Placement and Profile

The bottom distribution in figure 6.4 shows the photon probability density of a configuration in which the LED is placed at position $(0, 0, R_{sphere})$, with the beam directed in $(0,\ 0,\ -1)$ direction. The beam is focused, not illuminating any ports directly. Here, a configuration with multi-port integrating sphere has a $D = 12\,\mathrm{cm}$ diameter and 192 ports, each with an opening angle of $\alpha = 2°$. Apart from the shadows cast by the outer topology, a pattern of inhomogeneities is distinguishable on the northern hemisphere. This pattern consists of photons that are reflected once on the southern hemisphere, and then leave the POCAM through a port on the opposite hemisphere. After one reflection the probability of hitting a hole on the opposite side of the integrating sphere is higher due to the geometry.

To test this, the pattern can be altered by changing the LED position and beam direction. The top distribution in figure 6.4 shows the photon probability distribution from the same configuration, but the photon source emits its beam from position $(R_{\text{sphere}}, 0, 0)$ in the $(-1, 0, 0)$ direction. There are no direct photons, since there are no ports in the illuminated area. Furthermore, the inhomogeneities caused by photons exiting after the first reflection is minimized.

In the following configuration and in all other results in this section, the LED is positioned at $(R_{sphere}, 0, 0)$ and emits in the $(-1, 0, 0)$ direction.

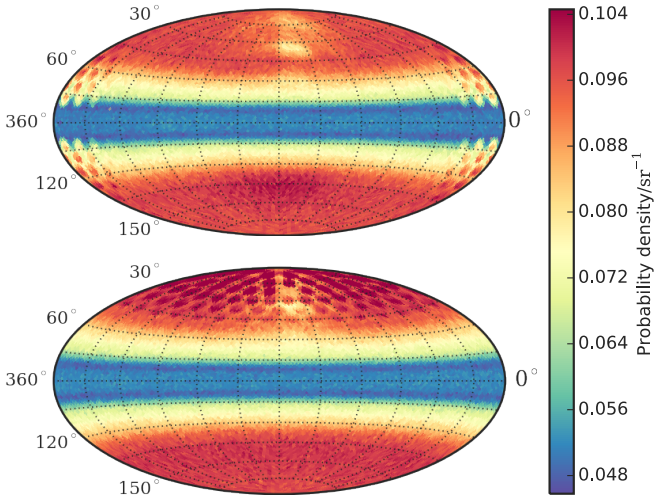


**Figure 6.4:** *This figure shows the influence of the LED placement and its emission direction. In the lower plot, the LED is placed on position* $(0, 0, R_{sphere})$*, with a beam direction of* $(0, 0, -1)^T$*, whereas in the upper plot, the LED is placed on position* $(R_{sphere}, 0, 0)$ *and emits in the* $(-1, 0, 0)$ *direction.*

### 6.4.2 Port Properties

The properties of the ports are of significant influence on both the timing and homogeneity of the POCAM output.

#### Port Exclusion

A consideration in the early design was to omit ports that are in the same zenith angle range as the harness, to reduce the fraction of photons that is absorbed by the harness. However, the simulation has shown that omitting ports in any region lowers the overall homogeneity. Spherical symmetry is of clear importance for the emission's isotropy. With omitted ports the transition from shadow to no shadow is more gradual. This essentially increases the angular area of the harness shadow, which is undesirable. Therefore, in all other shown configurations, ports are not omitted in any region.

#### Port Size and Number

In figure 6.5 the radiation directional distribution is shown for four configuration with varied port properties. The most important emission characteristics associated with these configurations are listed in table 6.1. In these configurations the number and size of the ports are varied. The port number is varied with HEALPix order 2, corresponding to 192 ports, and HEALpix order 3 with 768 ports. For both port orders the effective transmissivity is varied with 2.5 % and 1.46 %, corresponding to opening angles $\alpha$ as listed in table 6.1.

The shadows casted by the outer topology are clearly distinguishable for all configurations. Additionally, configuration 1 and 2 show a pattern of inhomogeneities corresponding to their respective port distribution, this effect decreases for smaller $\alpha$. Furthermore configurations 1, 2 and 3 show a clear inhomogeneity caused by the LED

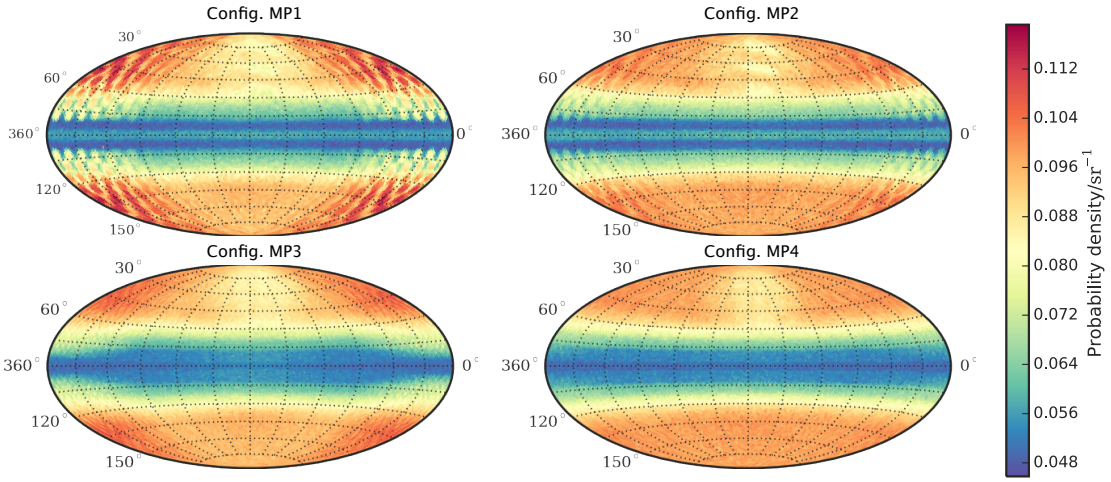


**Figure 6.5:** *The photon probability distributions of multi-port configurations 1-4, varying the number and size of the ports. The corresponding properties are listed in table 6.1*

.

emission profile as discussed in 6.4.1. This effect fades out for configuration 4, which has the lowest inhomogeneity with values of 11.9 for $\theta < 60°$, and 11.5 for $\theta > 120°$.

The time profile of configurations 1-4 are visualized in figure 6.6. Respective time constants $\tau$ are listed in table 6.1. A strong correlation between the transmission and $\tau$ is exhibited. Naturally, this is due to a lower amount of reflections, i.e. photons leaving the POCAM after less reflections. This is also visible as inhomogeneities in 6.5, resulting in higher inhomogeneity values, see table 6.1.

As visible in figure 6.5, a local maximum arises at $\theta = 90°$ for configurations with 192 ports (HEALPix order 2), whereas a minimum arises for configurations with 768 ports (HEALPix order 3). This effect is caused by the positioning of ports in the zenith angle region around the harness. The equidistantly spaced ports are dividable in rings of ports, as described in figure 5.5.

In figure 6.7 the directional distribution of configuration 2 and 4 are decomposed in the emission from ports on HEALPix rings with angles in the harness region. For configuration 2 (192 ports) rings 7, 8 and 9 lie in the harness region. For configuration 4 (768 ports), rings 15-21 lie in the harness region.

The harness shadow in the emission from the rings in the harness zenith region is larger for HEALPix order 2 than for order 3. This is due to the smaller distances between the rings for order 3. It can be concluded that configurations with orders $\leq$ 2 result in a local maximum, whereas configurations with order $\geq$ 3 result in a local minimum in the probability density at $\theta = 90°$.

### 6.4.3 Integrating Sphere Radius

Varying the radius of the of the integrating sphere has a significant impact on both the homogeneity and the time profile. As visible in figure 6.8, and 6.9b, a smaller integrating sphere results in a smaller shadow transition region. For both the penetrator and the harness shadow, the shadow gets stronger and the transition region smaller

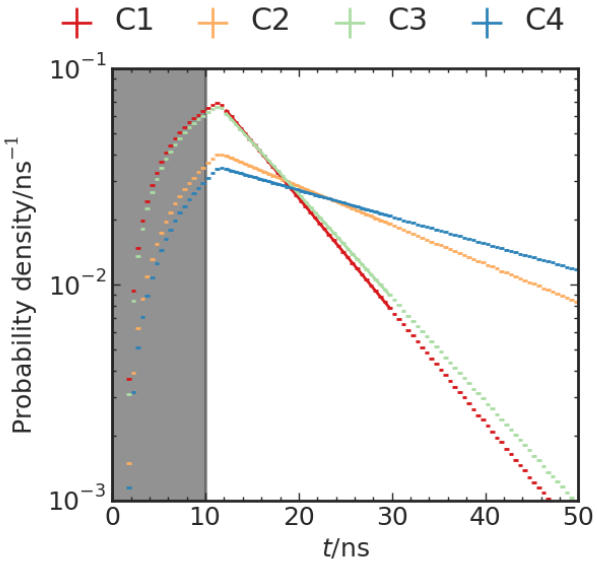


**Figure 6.6:** *Time profiles of multi-port configurations 1-4. The probability density is normalized to the number of emitted photons. The LED emission during the first 10 ns is marked grey. An exponential is fitted to the data between 25 and 45 ns, the resulting decay time can be found in 6.1.*

for smaller diameter. Moreover, the homogeneous region increases with decreasing transition zone.

As shown in figure 6.9a the time profile is influenced strongly by the radius as well. A smaller integrating sphere means a shorter path between reflections, implying a generally shorter time span before a photon leaves the integrating sphere. Decreasing the integrating sphere's diameter, $\tau$ decreases from 35.1 to 11.7 ns.

For configuration 7, the ports have a radius of 2 mm. Even though in the simulation a higher homogeneity could be reached by decreasing $\alpha$, a smaller port diameter is undesirable for construction reasons.

| Config. | $n$ | $D$ | $\alpha/°$ | $T$ | $A$ | $\tau/ns$ | Inhomogeneity | | |
|---|---|---|---|---|---|---|---|---|---|
| | | | | | | | $\theta < 60°$ | $60° \leq \theta \leq 120°$ | $\theta > 120°$ |
| MP 1 | 192 | 24 | 4 | 2.5 % | 37.1 % | 8.3 | 8.9 % | 19.2 % | 7.0 % |
| MP 2 | 192 | 24 | 2 | 1.46 % | 57.7 % | 24.2 | 5.8 % | 16.5 % | 4.2 % |
| MP 3 | 768 | 24 | 2 | 2.5 % | 37.1 % | 9.1 | 7.1 % | 17.7 % | 5.3 % |
| MP 4 | 768 | 24 | 0.5 | 1.46 % | 47.7 % | 35.1 | 5.0 % | 17.3 % | 3.8 % |
| MP 5 | 768 | 18 | 0.5 | 1.46 % | 62.9 % | 20.6 | 5.5 % | 32.3 % | 1.95 % |
| MP 6 | 768 | 12 | 0.5 | 1.46 % | 66.4 % | 14.7 | 7.5 % | 50.2 % | 1.8 % |
| MP 7 | 768 | 6 | 0.5 | 1.46 % | 61.8 % | 11.7 | 1.6 % | 66.3 : % | 1.6 % |

**Table 6.1:** *POCAM configurations: Influence of the integrating sphere diameter, number of ports $n$, diameter $D$, port opening angle $\alpha$, effective photon transparency $T$, photon absorption $A$, exponential time constant $\tau$ and inhomogeneity for three different zenith angle zones.*

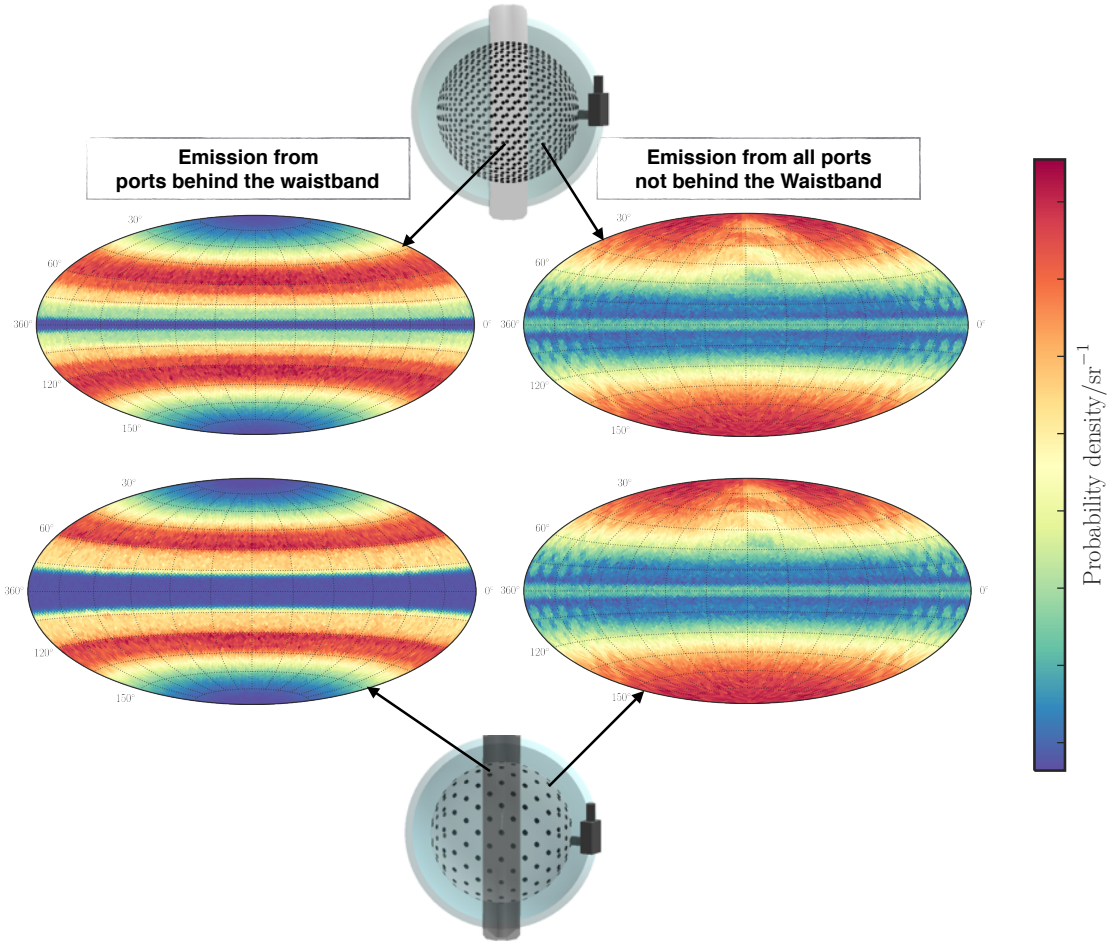


**Figure 6.7:** *This figure shows the decomposition of the directional emission probability density in the photons emitted from ports in the harness region and all other ports. This is shown for two different configurations, with order 2 (Bottom) and order 1 (top). This is a conceptual aid, the exact probability density is arbitrary.*

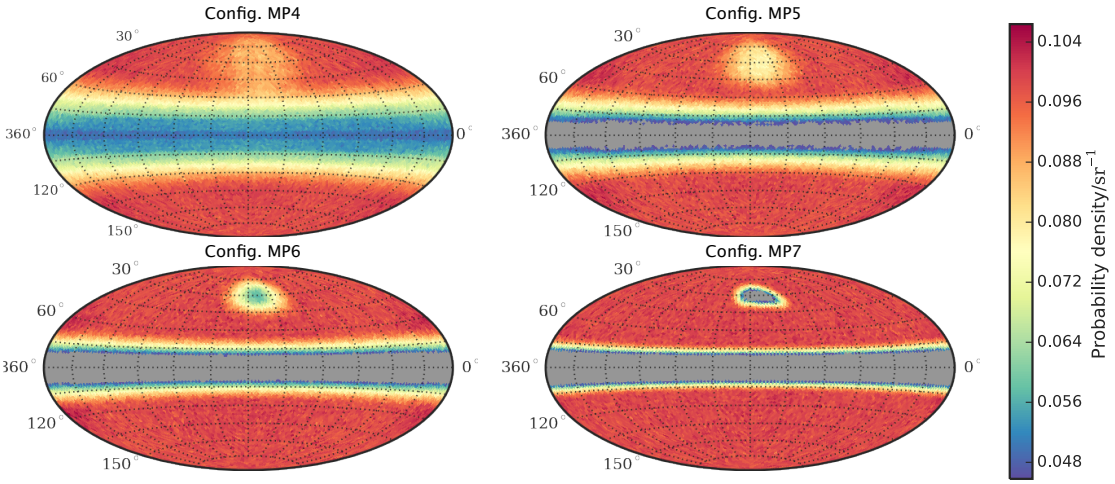


**Figure 6.8:** *The photon probability distributions of multi-port configurations 4-7, varying the diameters of the integrating sphere. The corresponding properties are listed in table 6.1*

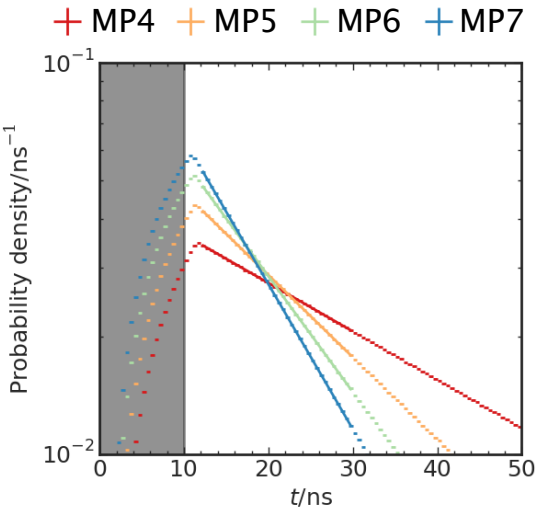


**(a)** *Time profiles of multi-port configurations 4, 5, 6 and 7. The time profile clearly gets shorter for smaller integrating sphere radii. The corresponding $\tau$ values are listed in table 6.1*

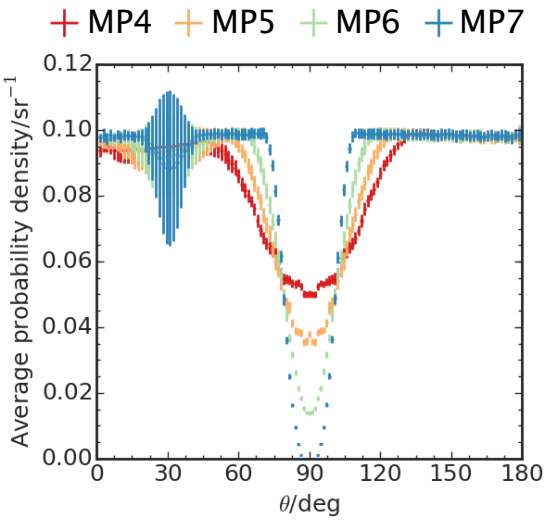


**(b)** *Probability density of photon emission averaged over zenith bands. The error bars show the standard deviation.*

**Figure 6.9:** *Time profile (left) and average probability density in a zenith band projection of configurations 4-7.*

Taking all the simulations into account, the best homogeneity is reached with 768 ports with small opening angle. The lowest $\tau$ values are reached with smaller integrating spheres. Therefore we can conclude that of all configurations presented here, multi-port configuration 7 is the most preferable, with a lowest inhomogeneity value of 1.6 % in the zenith angle region $\theta > 120°$.

## 6.5 Semi-transparent Configuration

This section describes the main results of the simulation with a semi-transparent PTFE integrating sphere. The setup is described in 5.3.1, transmission and reflection values are based on 5.6. Taking into account that the in the previous section uncovered relation between radius, time profile and homogeneity also applies to the semi-transparent integrating sphere, each configuration shown here has a diameter of $6\,\mathrm{cm}$. The opening angle of the LED is $60°$ for configurations 1-4, but is varied for configurations 5-7. The properties of the semi-transparent (ST) configurations 1-7 are listed in table 6.2.

### 6.5.1 Variation of Transmissivity

To investigate how strongly the thickness of the PTFE, and with it the transmissivity, reflectivity and absorptivity, (see equation 5.17) influence the properties of the emission, four exemplary configurations varying the $d$ from 1 to $6\,\mathrm{mm}$, ST 1-4, are presented here.

Figure 6.10a shows the directional probability distribution of configurations 1 and 3. For configuration 1, a higher probability density is distinguishable in the angular area

illuminated by the LED. This is indistinguishable for configurations 2-4, for this reason only the probability density distributions configurations 1 and 3 are shown.

The corresponding time profiles are visualized in figure 6.10b. The lowest $\tau$ is reached with configuration 1. However, this goes hand in hand with the inhomogeneity visible in figure 6.10a.

There is a strong reduction of $\tau$-values for the semi-transparent configurations with respect to the multi-port configurations. Furthermore, the corresponding inhomogeneity values are lower as well. This is due to the diffuse transmission. Where in a multi-port configuration the lambertian reflection is solely responsible for the diffuse emission from the ports, in a semi-transparent configuration the lambertian transmission adds to the diffusivity of the integrating sphere. Therefore, similar levels of homogeneity can be reached with the semi-transparent integrating sphere with generally less reflections and accordingly low $\tau$.

Considering both time profile and homogeneity, semi-transparent configuration 2 exhibits the best properties, with a inhomogeneity of 1.75 % in non-shadow regions and a $\tau$ of 3.1 ns.

The irregularity in the absorption values should be noted. This is due to the interpolation of reflectivity measurements on PTFE. More measurements are needed to increase the accuracy of the PTFE modelling. These results are a first approximation that needs to be confirmed with prototype measurements.

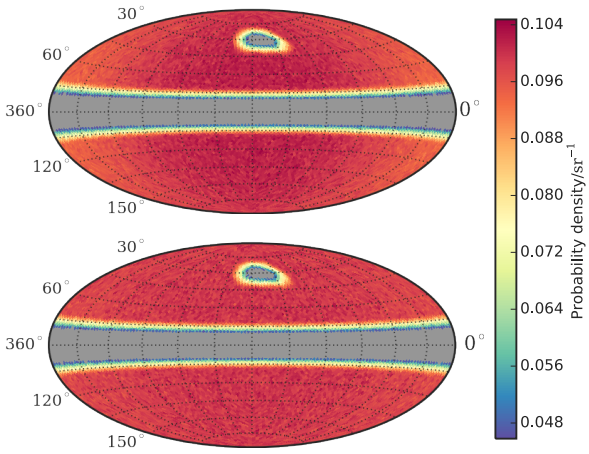


**(a)** *The directional distribution of emission from configurations ST1 (top) and ST3 (bottom). The lower transmissivity in ST1 results in more 'direct' photons.*

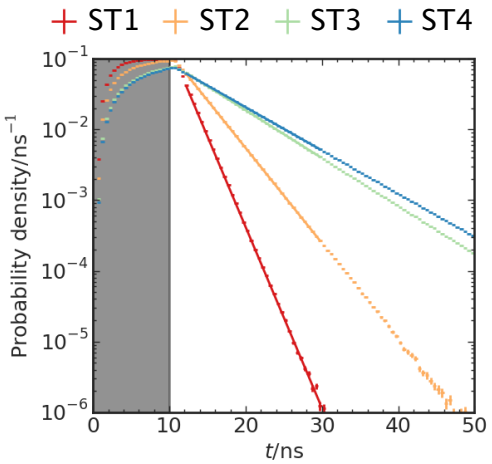


**(b)** *The time profile of configurations ST 1-4. An exponential is fitted to the probability density between 12 and* 30 ns.

**Figure 6.10:** *The Probability density of the emission direction of configurations ST1 and ST3 (a) and the time profiles of configurations ST 1-4 (b). The relevant corresponding values are listed in table 6.2. ST1 results in the lowest $\tau$, but this is partly due to a larger fraction of 'direct' photons, as is distinguishable in (a).*

### 6.5.2 Variation of LED Opening Angle

For the multi-port configurations the LED opening angle has been chosen to be small, in order to prevent direct photons, i.e. photons leaving the geometry before being reflected. For the semi-transparent configurations, this effect does not play a role. Therefore, based on semi-transparent configuration 2 with an $\alpha_{\mathrm{LED}}$ of 60°, three more configurations, ST 4-7, with $\alpha_{\mathrm{LED}}$ ranging from 30° to 120° are presented here.

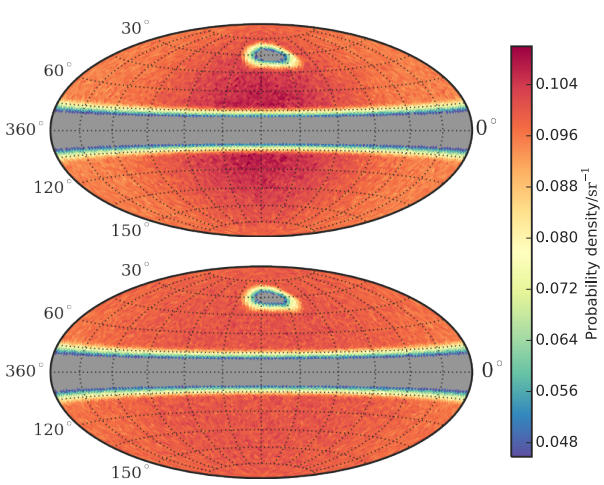


**(a)** *The directional distrubution of emission from Configurations ST 5 (Top) and 7 (Bottom).*

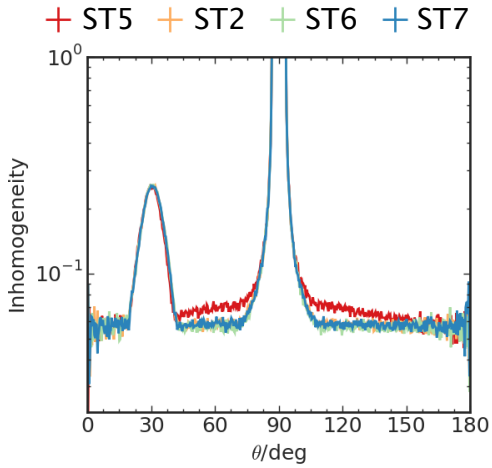


**(b)** *The inhomogeneity in zenith bands. Configuration ST5 with $\alpha_{LED} = 30°$ results in a less homogeneous emission.*

**Figure 6.11:** *Directional distribution (a) and inhomogeneity in zenith bands (b) of configurations varying $\alpha_{LED}$.*

In figure 6.11a the probability distributions of configurations ST5 and ST 7 are shown. For configuration ST5 the more concentrated beam is distinguishable in the probability density. A wider beam results in slightly lower inhomogeneity values. This is best visualized in the inhomogeneity for each zenith band of configurations 4-7. Configuration 5 has a higher inhomogeneity in almost all zenith bands, whereas differences for configurations 4,6 and 7 are indistinguishable, which is reflected in the inhomogeneity numbers in table 6.2 and in the the visualization of inhomogeneities over zenithangle in f 6.11. The time profile is not influenced by the opening angle of the LED, which is reflected in the values of $\tau$.

## 6.6 Baseline Configuration

A number of conclusions can be drawn on the presented configurations. For the multi-port configurations the best homogeneity is reached with 768 small ports. The lowest $\tau$ values are reached with smaller integrating spheres. Therefore multi-port configuration 7 is the most preferable.

For the semi-transparent configurations, the thickness of the semi-transparent layer is influencing both the time profile and the homogeneity of the emission. A thicker PTFE layer increases the homogeneity but decreases $\tau$. Widening the LED opening angle

| Config. | $d/mm$ | $\alpha_{\text{LED}}$ | $T$ | $R$ | $A$ | $\tau/ns$ | Inhomogeneity | | |
|---|---|---|---|---|---|---|---|---|---|
| | | | | | | | $\theta < 60°$ | $60° \leq \theta \leq 120°$ | $\theta > 120°$ |
| ST1 | 1 | 60° | 7.5 % | 92.4 % | 21.5 % | 2.7 | 10.3 % | 65.1 % | 3.20 % |
| ST2 | 2 | 60° | 2.5 % | 96.0 % | 50.7 % | 3.2 | 10.2 % | 64.7 % | 1.75 % |
| ST3 | 4 | 60° | 1.5 % | 98.0 % | 41.8 % | 6.4 | 10.2 % | 64.7 % | 1.43 % |
| ST4 | 6 | 60° | 1.2 % | 98.2 % | 48.5 % | 7.1 | 10.2 % | 64.7 % | 1.81 % |
| ST5 | 2 | 30° | 2.5 % | 96.0 % | 50.8 % | 3.2 | 10.1 % | 64.7 % | 2.22 % |
| ST6 | 2 | 90° | 2.5 % | 96.0 % | 50.7 % | 3.2 | 10.2 % | 64.7 % | 1.44 % |
| ST7 | 2 | 120° | 2.5 % | 96.0 % | 50.8 % | 3.2 | 10.2 % | 64.7 % | 1.47 % |

**Table 6.2:** *POCAM semi-transparent configurations: Influence of the integrating sphere diameter. number of ports $n$, port opening angle $\alpha$, effective photon transparency $T$, photon absorption $A$, exponential time constant $\tau$ and inhomogeneity for three different zenith angle zones.*

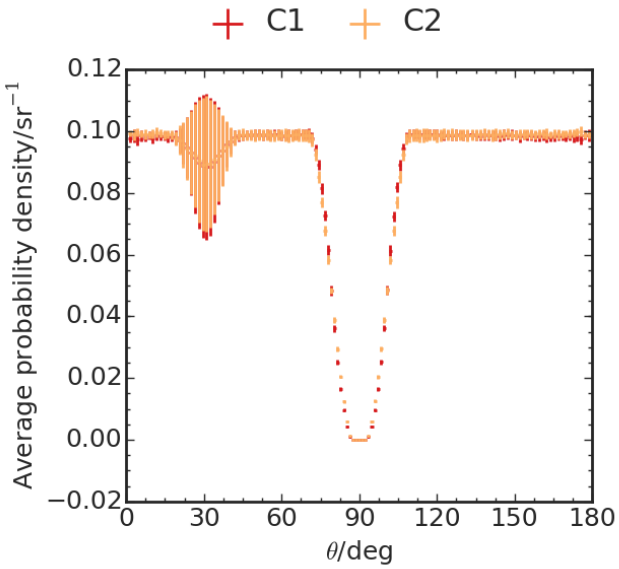


**Figure 6.12:** *Probability density averaged over zenith bands for configurations MP7 and ST2. The error bars show the standard error.*

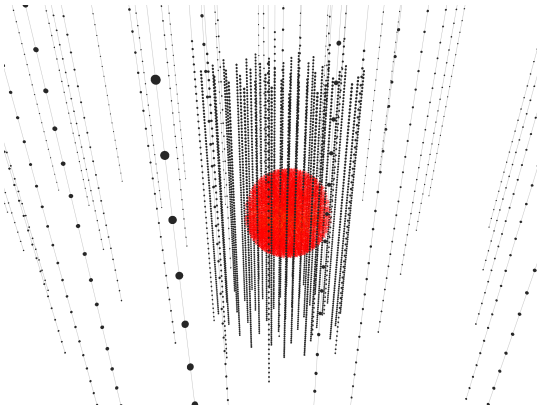

**(a)** *The photon-paths at an early stage after leaving the POCAM. The PINGU strings are clearly distinguishable from the surrounding IceCube strings due to the higher module density.*

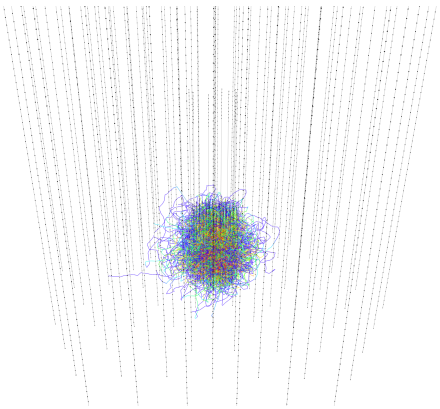

**(b)** *The photons paths from one POCAM flash. All IceCube and PINGU strings are visualized.*

**Figure 6.13:** *The photon-paths of a full POCAM flash at two stages: Zoomed in on PINGU At an early stage of the flash (a) and the entire detector with complete photon-paths (b). The red to blue color scale indicates the photon's arrival time. The used ice model is SPICE3*

increases the homogeneity and does not significantly influences the time profile. Taking all aspects into account, semi-transparent configuration 2 offers the most preferable combination of homogeneity and timing.

Comparing the properties of multi-port configuration 7 and semi-transparent configuration 2, it can be concluded that the semi-transparent integrating sphere results in significant better timing properties, with a $\tau$ of $3.7\,\mathrm{ns}$ compared to $11.7\,\mathrm{ns}$ for multi-port configuration 7.

Figure 6.12 shows the mean probability density per zenith band for configuration MP7 and ST2, with error bars showing the standard deviation. It can be concluded that the homogeneity is very similar for these two configurations. The inhomogeneity values are 1.6 % for multi-port configuration 7 and 1.75 % for semi-transparent configuration 2. Taking all this into account, we define semi-transparent configuration 2 as the current baseline geometry.

To summarize, this baseline consists of a $D = 6\,\mathrm{cm}$ integrating sphere of a $2\,\mathrm{mm}$ thickness, the LED is positioned at $(R_{sphere}, 0, 0)$, emitting a beam in the $(-1, 0, 0)$ direction with a $10\,\mathrm{ns}$ rectangular time profile and a $60°$ opening angle. The relevant emission properties are listed as ST2 in table 6.2.

## 6.7 CLsim Results

With the method described in section 5.3.2, the Geant4 output can be used to simulate POCAM flashes inside IceCube and PINGU.

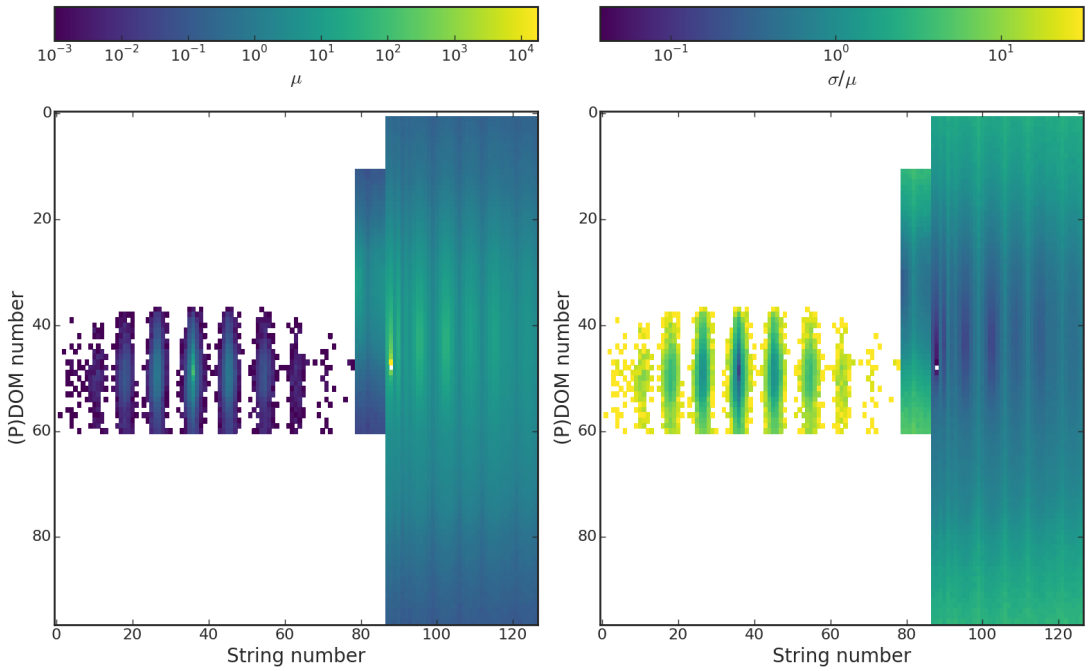


**Figure 6.14:** *The average $np$ (left) and the corresponding relative standard error (right) per (P)DOM, with the string number on the horizontal axes and DOM number on the vertical axes. The relative standard error is $\sigma/\mu$ with $\sigma$ the standard error and $\mu$ the average $np$. All strings and DOMs are shown.*

### 6.7.1 Propagation from the Baseline Configuration

A simulation of the baseline configuration in Geant4, with $10^8$ photons emitted from the LED, results in an emission spectrum as summarized in table 6.2. With the absorption of 50.7 % by the POCAM geometry, $5.07 \times 10^7$ photons enter the ice. In CLSim, The POCAM is placed on the position of DOM 48 on PINGU string 88. Applying the methed described in section 5.3.2, the photons are propagated through the detector.

Figure 6.13 is a visualization of the photon paths of one such POCAM flashes at two different time intervals. In 6.13b shows that the average photon path lengths cover the entire PINGU volume.

Figure 6.14 shows the average number of photons reaching an optical module $\mu$ (left), and the corresponding relative standard error (right) $\sigma/\mu$ for a simulation of a 1000 POCAM flashes. The 40 PINGU strings with 96 PDOMs each, the 8 DeepCore strings with 60 DOMs each and the 86 IceCube strings with 60 DOMs each are shown, with the string number on the horizontal axis and the DOM number on the vertical axis. The strings are ordered as in 4.2. From figure It can be seen that with 1000 simulated flashes all PDOMs are reached by at least one photon. Furthermore, the photons also reach all DeepCore DOMs under the dust layer (see figure 3.5) and a number of close IceCube DOMs. The standard error scales with the distance between the DOM and the POCAM. Figure 6.15 shows the average number of $np$ and the corresponding relative standard error of only the PDOMs.

The pattern of npe's in PINGU shows a relatively isotropic propagation from the POCAM. Naturally, the scattering and averaging over multiple flashes enhances the isotropy

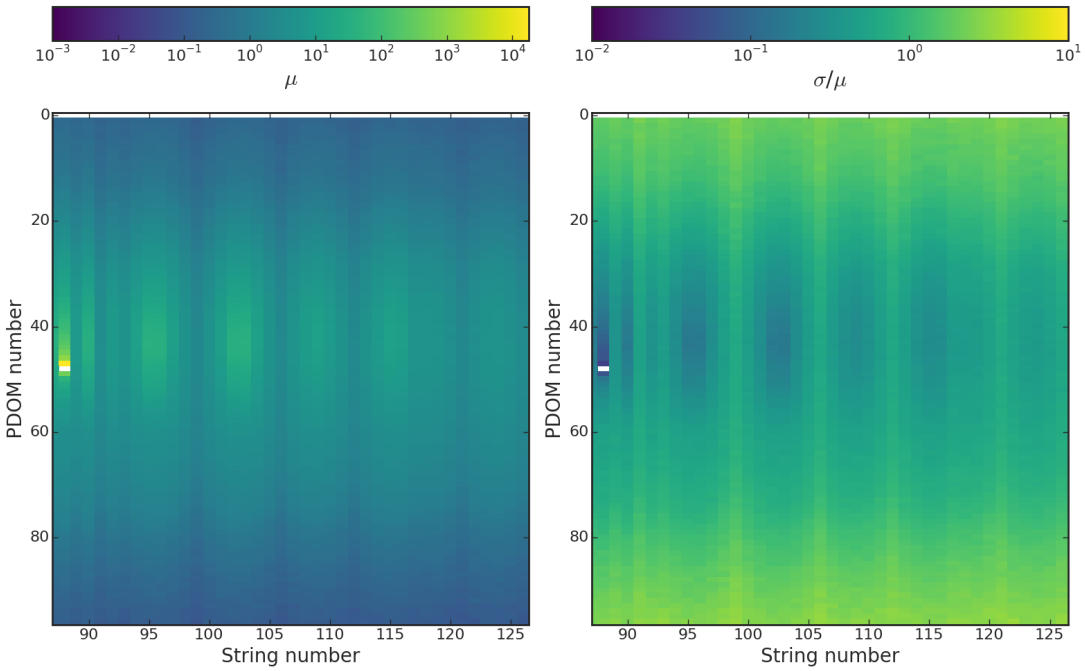


**Figure 6.15:** *The average $np$ (left) and the corresponding relative standard error (right) per (P)DOM, with the string number on the horizontal axes and DOM number on the vertical axes. The relative standard error is $\sigma/\mu$ with $\sigma$, with the standard error and $\mu$ the average $np$.*

of the POCAM emission by fading out any inhomogeneities. However, it should be noted that the method applied here is a first approximation. The method utilizing the HEALPix bins, as described in section 5.3.2, already partly fades the shadows of the outer topology. Therefore, any conclusive statements on shadow effects would be preliminary.

However, it can be concluded that the level of homogeneity reached in the non-shadow areas, i.e. an inhomogeneity of $\sim$10 % in zenith and $\sim$1 % in azimuth, in combination with the scattering in the ice, seems to create a sufficiently isotropic signal that illuminates all the PDOMs.

### 6.7.2 Sensitivity to Ice Models

To test the sensitivity of the POCAM to Simulations were run with several ice models, propagating 1000 POCAM flashes from the baseline geometry, to test the sensitivity of the POCAM to ice models. Figure 6.16 shows the relative difference in average $np$ between the simulations with the SPICE3 and SPICE-Lea ice models (left), and the corresponding standard error (right). The scattering and absorption lengths defined in SPICE3 are shown in 3.6.

Some interesting differences between the simulations with these two ice models can be noted. With SPICE-LEA, an average of 33593 photons reach a DOM, whereas 33677 photons reach a DOM with SPICE3. Furthermore, in figure 6.16, we can see that the DOMs above the POCAM are generally reached by more photons with the SPICE3 ice

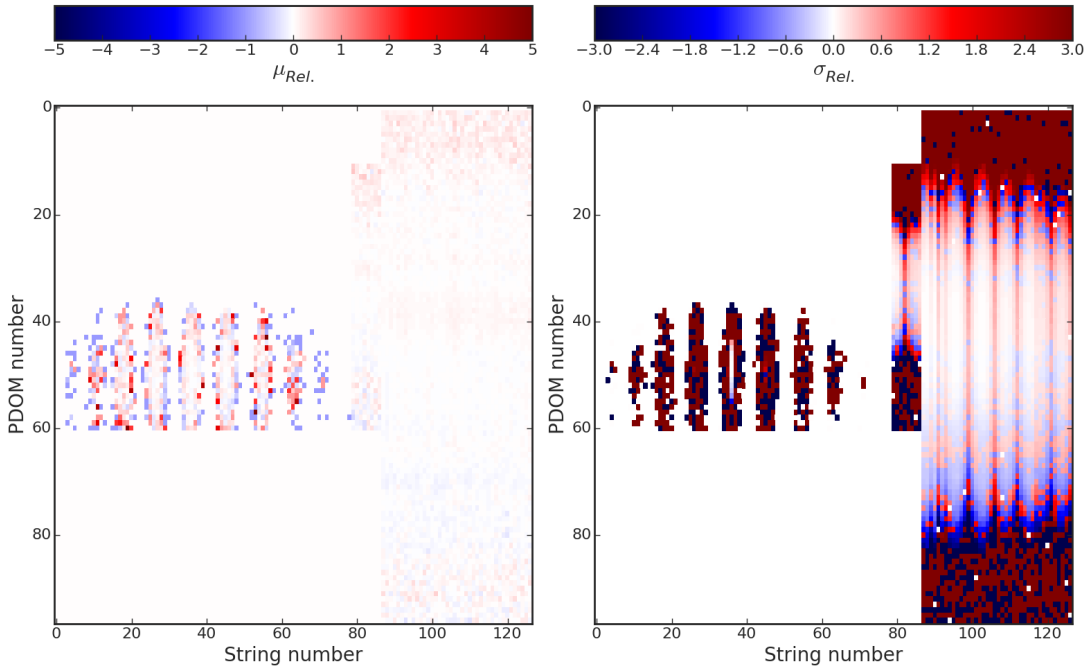


**Figure 6.16:** *Left: The relative difference in average $np$ reaching each (P)DOM for ice models SPICE3 and SPICE-LEA. Right: The corresponding relative standard error per (P)DOM, with the string number on the horizontal axes and DOM number on the vertical axes. The relative standard error is* $\mu_{Rel.} = \frac{\mu_{SP3} - \mu_{LEA}}{\mu_{LEA}}$ *with corresponding standard error* $\sigma_{Rel.} = \sqrt{\frac{\sigma^2_{SP3}}{\mu^2_{LEA}} + \frac{\mu^2_{SP3}\sigma^2_{LEA}}{\mu^4_{LEA}}}$. *The standard error has been multiplied with the sign of* $\mu_{Rel.}$. *The maximum value of sigma has been set to 3.0, in order to show the development of* $\sigma_{Rel.}$ *for PDOMs close to the POCAM.*

model than in the SPICE-LEA ice model. The propagated standard error $\sigma_{Rel.}$ shows that the differences could be significant.

It is important to emphasize that these are photons that reach a DOM volume in the simulation, and does not take PMT efficiency or energy scale into account. Furthermore, this simulation is a first approximation, which needs to be investigated further. Therefore, conclusive statements on these results would be preliminary. Nevertheless, we can say that the results from this first approximation indicate a promising sensitivity of the POCAM to ice models.

# Chapter 7

# Conclusions and Outlook

## 7.1 Conclusion

This thesis presents the design study of the POCAM, which is intended to be implemented in the low energy extension of the IceCube neutrino detector, PINGU. The POCAM is a calibration module which emits an isotropic and 'fast' light pulse from a central position in the instrumented ice of PINGU. The light propagates through the ice, and is detected by the PDOMs in PINGU, and the DOMs of IceCube. With the isotropic signal, some aspects of the detector calibration can be verified or brought to a higher precision.

This precision is important for PINGU, which is designed to detect atmospheric neutrinos at a threshold of a few GeV. This low energy infill opens the door to a number of scientific goals that were not pursuable with IceCube. One aspect of neutrino physics that will be addressed with PINGU is neutrino oscillation. In contrast to the SM description of neutrinos, it has been proven that neutrinos oscillate and are, therefore, massive. A neutrino with energy $E$ oscillates over a distance $L$ with a probability described by equation 1.11. Each neutrino flavor eigenstate is a mix of at least three mass eigenstates. The mass differences between the eigenstates are known. However, the neutrino mass hierarchy is unknown. It is either normal or inverted.

Cosmic rays interact in the earths atmosphere, creating air showers. Mesons in the hadronic component of air showers decay to neutrinos, comprising the atmospheric neutrino flux. Due to their small cross-section, neutrinos traverse the earth without being absorbed. The oscillation of neutrinos, however, is affected by the earth due to the abundance of electrons. Electron neutrinos interact with the electrons in the earth, effecting the mixing with the other neutrino flavors. Assuming either NH or IH, different matter effects for neutrinos and antineutrinos are predicted. PINGU will utilize this to determine the NMH.

IceCube has a lower energy threshold of $100\,\mathrm{GeV}$ ($10\,\mathrm{GeV}$ with DeepCore) and is designed mainly to detect high energy astrophysical neutrinos. When high energy neutrinos undergo Deep Inelastic Scattering in the ice, energy is deposited in the ice in the shape of Cherenkov radiation. This radiation is measured by DOMs in the ice and neutrinos are identified on signature radiation patterns. Based on the detected Cherenkov radiation, the flavor, direction and energy of a detected neutrino can be derived. Naturally, calibration is an essential part of the detector systematics. Calibration of IceCube is based on LED flashers in the DOMs, in ice calibration lasers and appropriate low energy single muons. With these, the detector's geometry, timing and energy are calibrated.

IceCube-Gen2 consists of HEX and PINGU. PINGU is more relevant for this thesis. PINGU lowers the threshold to a few GeV. The DOMs in PINGU are distributed in a volume of ice in the center of IceCube that has been shown to be exceptionally clear. The density of strings and PDOMs is a lot higher than in IceCube. The design and planned deployment builds strongly on the experience gained by deploying and running IceCube. Many of PINGUs components are improved based on progressed technology and experience. The drill holes are to be degassed, which should increase the absorption and scattering length of the hole-ice. Since the energy threshold is to be as low as possible, proper calibration is an essential part of the PINGU design. Updated LED flashers are placed in the PDOMs. Cameras are planned to be deployed to measure hole ice properties. Furthermore the isotropic light source POCAM could enhance the geometry calibration, verify the energy scale and energy resolution.

The design goal of the POCAM are to create a homogeneous illumination of the PINGU ice volume with a fast light pulse. The module has to be self monitoring and the design should implement techniques and materials known to IceCube, to ensure effective construction and deployment. The design of the POCAM consist of an integrating sphere, which isotropizes the light emitted from one or more internal LEDs. The integrating sphere isotropizes the light by multiple lambertian reflections of each photon before it leaves the module. The sphere is either semitransparent or has multiple ports. A diode is placed on the sphere to monitor the emission. The integrating sphere and all necessary hardware is enveloped by a spherical pressure housing and harness just as the PDOMs. The POCAM is to be deployed just as the Optical Modules. A hanging assembly connects the POCAM to the main cable. The design is tested and optimized by simulation. A design of the module is build in Geant4, with which the POCAM components and its optical properties are defined and photon propagation through the module is simulated. Once the photon leaves the POCAM, the simulation of propagation through the PINGU geometry is done with CLSim, a for IceCube designed ray-tracing algorithm.

The contribution of my thesis work is mainly in the Geant4 and CLSim simulation and the application of the simulation to optimize the design of the POCAM. This is therefore discussed in detail.

The Geant4 simulation effort has given important insight in the design of the POCAM. Simulating configurations with a multi-port integrating sphere has shown that the most homogeneous illumination is achieved with 768 small ports. The lower limit of the port-diameter is $2\,\mathrm{mm}$, which is determined by construction limits. Decreasing the size of the integrating sphere results in a faster pulse. Therefore, the current best multi-port configuration utilizes an integrating sphere with a diameter of $6\,\mathrm{cm}$, 768 equidistant ports and an opening angle of $0.5°$, corresponding to a port-diameter of $2\,\mathrm{mm}$. The internal LED emits a concentrated beam on a port-less region in the harness zenith region. Simulations with this configurations result in an exponential time constant $\tau$ of $11.7\,\mathrm{ns}$ and a inhomogeneity in the non-shadow region of 1.6 %.

The relation between the radius of the sphere and the time profile is the same for configurations with the semitransparent integrating sphere. The best homogeneity is reached for a wider beam. The pulse from a semitransparent beam has shown to be generally faster than from a multi-port beam. Naturally, a thicker integrating sphere results in a slower pulse and higher absorption. The best properties have been achieved with a wide beam, an integrating sphere with a diameter of $6\,\mathrm{cm}$ and a PTFE thickness of $2\,\mathrm{mm}$. This results in an exponential time constant $\tau$ of $3.2\,\mathrm{ns}$ and a inhomogeneity in

the non-shadow region of 1.75 %, with an absorption of 50.7 %. Taking all design goals and simulations into account, mainly based on the significantly smaller exponential time constant, the current baseline of the POCAM is defined to be the aforementioned semitransparent configuration. The relevant properties of this configuration can be found in table 6.2.

Since the best emission properties are reached with the semitransparent configuration, the output of the baseline configuration is used to propagate photons through the PINGU and IceCube geometry. One POCAM flash is defined by the Geant4 hdf5 table output. Running 1000 POCAM flashes and averaging over these show a relatively homogeneous illumination of the ice. The scattering in the ice isotropizes the emission from the POCAM further and seems to fade out the shadows cast by the outer topology. All PINGU and DeepCore, and some IceCube DOMs are illuminated.. Varying several ice-models suggests a sensitivity of the POCAM to the ice properties. A basic energy resolution calculation suggests that the POCAM could play a role in this part of the calibration as well.

## 7.2 Outlook

An important next step in the simulation is to further investigate the propagation of the POCAM emission through PINGU. It needs to be investigated wether the binning of photons can be circumvented. In the current CLSim simulation the algorithm breaks down when every photon is propagated individually. When this capacity could be achieved, the precision of the calibration would greatly improve, which would enable more conclusive statements on for example the effect of the cable, harness and penetrator shadow.

An aspect that has not yet been studied with CLSim is the timing. The time profile of the Geant4 output has been taken into account for the CLSim propagation, but no tests on the timing have been done yet. Additionally the possible role of the POCAM in the geometry, timing and energy calibration needs to be investigated in more detail. Finally, the sensitivity to the ice properties can be shown in more detail by varying single ice properties as defined in the ice-tables.

Apart from the simulation, a prototyping effort has started. The Geant4 simulation is in a number of aspects idealized. The most important examples of which, are the $10\,\mathrm{ns}$ rectangular LED emission, perfect homogeneity in the thickness and density of the PTFE and corresponding perfect lambertian reflection and transmissivity of the PTFE. These properties need to be verified or corrected. Currently, first measurements of the diffusing properties of a PTFE semitransparent integrating sphere are underway. Additionaly, the properties of a basic Kapustinsky circuit are being measured.

Next steps in the prototyping phase involve constructing a full prototype, with which to measure the emission properties in water. Once a complete prototype is build, all emission characteristics from the Geant4 simulation need to be verified.

# Bibliography


[1] M. G. Aartsen et al.
"Energy Reconstruction Methods in the IceCube Neutrino Telescope".
In: *JINST* 9 (2014), P03009. arXiv: 1311.4767 [physics.ins-det]
(cit. on pp. 26, 32 sq.).

[2] M. G. Aartsen et al.
"Evidence for High-Energy Extraterrestrial Neutrinos at the IceCube Detector".
In: *Science* 342 (2013), p. 1242856. arXiv: 1311.5238 [astro-ph.HE]
(cit. on p. 21).

[3] M. G. Aartsen et al.
"Letter of Intent: The Precision IceCube Next Generation Upgrade (PINGU)".
In: (2014). arXiv: 1401.2046 [physics.ins-det] (cit. on pp. 21, 36, 40).

[4] M. G. Aartsen et al. "Measurement of South Pole ice transparency with the IceCube LED calibration system".
In: *Nucl. Instrum. Meth.* A711 (2013), pp. 73–89.
arXiv: 1301.5361 [astro-ph.IM] (cit. on pp. 22, 25, 27 sq.).

[5] M. G. Aartsen et al. "Measurement of South Pole ice transparency with the IceCube LED calibration system".
In: *Nucl. Instrum. Meth.* A711 (2013), pp. 73–89.
arXiv: 1301.5361 [astro-ph.IM] (cit. on p. 41).

[6] M. G. Aartsen et al.
"Search for Astrophysical Tau Neutrinos in Three Years of IceCube Data".
In: (2015). arXiv: 1509.06212 [astro-ph.HE] (cit. on pp. 26 sq.).

[7] M. Aartsen et al.
"IceCube-Gen2: A Vision for the Future of Neutrino Astronomy in Antartica".
In: (2014). eprint: astro-ph/1412.5106v2 (cit. on p. 42).

[8] R. Abbasi et al. "The Design and Performance of IceCube DeepCore".
In: *Astropart. Phys.* 35 (2012), pp. 615–624. arXiv: 1109.6096 [astro-ph.IM]
(cit. on pp. 21, 24).

[9] R. Abbasi et al. "The IceCube Data Acquisition System: Signal Capture, Digitization, and Timestamping".
In: *Nucl. Instrum. Meth.* A601 (2009), pp. 294–316.
arXiv: 0810.4930 [physics.ins-det] (cit. on p. 25).

[10] A. Achterberg et al.
"First Year Performance of The IceCube Neutrino Telescope".
In: *Astropart. Phys.* 26 (2006), pp. 155–173.
arXiv: astro-ph/0604450 [astro-ph] (cit. on p. 31).

[11] M. Ackermann et al. "Optical properties of deep glacial ice at the South Pole".
In: *J. Geophys. Res.* 111.D13 (2006), p. D13203 (cit. on pp. 26, 29).

[12] M. Ageron et al. "The ANTARES Optical Beacon System".
In: *Nucl. Instrum. Meth.* A578 (2007), pp. 498–509.
arXiv: astro-ph/0703355 [ASTRO-PH] (cit. on p. 45).

[13] S. Agostinelli et al. "GEANT4: A Simulation toolkit".
In: *Nuclear Instruments and Methods* A506 (2003), pp. 250–303 (cit. on p. 49).
[14] Q. R. Ahmad et al. "Measurement of the rate of $\nu_e + d \rightarrow p + p + e^-$ interactions produced by $^8B$ solar neutrinos at the Sudbury Neutrino Observatory".
In: *Phys. Rev. Lett.* 87 (2001), p. 071301. arXiv: nucl-ex/0106015 [nucl-ex]
(cit. on pp. 4 sq.).
[15] J. Ahrens et al. "IceCube Preliminary Design Document". In: (2001)
(cit. on pp. 44 sq.).
[16] *Air Shower wikipedia page*.
https://en.wikipedia.org/wiki/Air_shower. Accessed: 2015-11-05
(cit. on p. 15).
[17] E. K. Akhmedov. "Neutrino physics".
In: *Particle physics. Proceedings, Summer School, Trieste, Italy, June 21-July 9, 1999*.
1999, pp. 103–164. arXiv: hep-ph/0001264 [hep-ph] (cit. on pp. 8 sqq.).
[18] E. K. Akhmedov, M. Maltoni, and A. Yu. Smirnov.
"1-3 leptonic mixing and the neutrino oscillograms of the Earth".
In: *JHEP* 05 (2007), p. 077. arXiv: hep-ph/0612285 [hep-ph] (cit. on p. 18).
[19] W. D. Apel et al. "Kneelike structure in the spectrum of the heavy component of cosmic rays observed with KASCADE-Grande".
In: *Phys. Rev. Lett.* 107 (2011), p. 171104. arXiv: 1107.5885 [astro-ph.HE]
(cit. on p. 14).
[20] R. Barbieri, P. Creminelli, and A. Strumia.
"Neutrino oscillations from large extra dimensions".
In: *Nucl. Phys.* B585 (2000), pp. 28–44. arXiv: hep-ph/0002199 [hep-ph]
(cit. on p. 5).
[21] G. D. Barr et al. "A Three - dimensional calculation of atmospheric neutrinos".
In: *Phys. Rev.* D70 (2004), p. 023006. arXiv: astro-ph/0403630 [astro-ph]
(cit. on p. 17).
[22] G. Battistoni et al. "The FLUKA atmospheric neutrino flux calculation". In:
*Astropart. Phys.* 19 (2003). [Erratum: Astropart. Phys.19,291(2003)], pp. 269–290.
arXiv: hep-ph/0207035 [hep-ph] (cit. on p. 17).
[23] R. Bernabei et al. "New results from DAMA/LIBRA".
In: *Eur. Phys. J.* C67 (2010), pp. 39–49. arXiv: 1002.1028 [astro-ph.GA]
(cit. on p. 37).
[24] A. Bernhard. "Origin of IceCubes Astrophysical Neutrinos: Autocorrelation, Multi-Point-Source and Time-Structured Searches."
PhD thesis. Technische Universität München, 2015 (cit. on p. 26).
[25] M. Bishai et al. "Neutrino Oscillations in the Precision Era". In: (2012).
arXiv: 1203.4090 [hep-ex] (cit. on p. 8).
[26] *The IceCube-Gen2 High Energy Array*. 2015.
arXiv: 1510.05228 [astro-ph.IM] (cit. on p. 21).
[27] P. Cerenkov. "Visible Radiation Produced by Electrons Moving in a Medium with Velocities Exceeding that of Light". In: *Physical Review* 52, 378 (1973)
(cit. on p. 22).
[28] L. Classen and A. Kappes. "Multi-PMT optical modules for IceCube-Gen2". In:
2015. arXiv: 1510.05228 [astro-ph.IM] (cit. on p. 38).
[29] S. Coenders. "Capability of Earth Tomography Using Oscillations of Atmospheric Neutrinos with PINGU."
MA thesis. Rheinisch-Westfälischen Technischen Hochschule Aachen, 2013
(cit. on pp. 18, 37).

[30] B. Doherty. *PIN Diode Fundamentals*. 701st ed. Microsemi Watertown (cit. on p. 49).

[31] *DOM Acceptance Table for Photonics and Romeo*. `https://wiki.icecube.wisc.edu/index.php/File:Glass_transmit_compare.gif`. Accessed: 2015-02-19 (cit. on p. 49).

[32] A. M. Dziewonski and D. L. Anderson. "Preliminary reference earth model". In: *Phys. Earth Planet. Interiors* 25 (1981), pp. 297–356 (cit. on pp. 17 sq.).

[33] W. U. Ehrmann and A. Mackensen. "Sedimentological evidence for the formation of an East Antarctic ice sheet in Eocene-Oligocene time". In: *Palaeogeography, Palaeoclimatology, Palaeoecolog* 93 (1992), pp. 85–112 (cit. on p. 26).

[34] R. Foot et al. "Seesaw Neutrino Masses Induced by a Triplet of Leptons". In: *Z. Phys.* C44 (1989), p. 441 (cit. on p. 5).

[35] J. A. Formaggio and G. P. Zeller. "From eV to EeV: Neutrino Cross Sections Across Energy Scales". In: *Rev. Mod. Phys.* 84 (2012), p. 1307. arXiv: `1305.7513 [hep-ex]` (cit. on p. 36).

[36] T. K. Gaisser and M. Honda. "Flux of atmospheric neutrinos". In: *Ann. Rev. Nucl. Part. Sci.* 52 (2002), pp. 153–199. arXiv: `hep-ph/0203272 [hep-ph]` (cit. on pp. 16 sq.).

[37] T. K. Gaisser. "Spectrum of cosmic-ray nucleons, kaon production, and the atmospheric muon charge ratio". In: *Astropart. Phys.* 35 (2012), pp. 801–806. arXiv: `1111.6675 [astro-ph.HE]` (cit. on p. 16).

[38] C. Giunti and C. W. Kim. *Fundamentals of Neutrino Physics and Astrophysics*. 2007 (cit. on pp. 4, 7, 17, 35).

[39] M. C. Gonzalez-Garcia, M. Maltoni, and T. Schwetz. "Updated fit to three neutrino mixing: status of leptonic CP violation". In: *JHEP* 11 (2014), p. 052. arXiv: `1409.5439 [hep-ph]` (cit. on pp. 10 sq.).

[40] K. M. Gorski et al. "The healpix primer". In: (1999). arXiv: `astro-ph/9905275 [astro-ph]` (cit. on p. 51).

[41] K. Greisen. "End to the cosmic ray spectrum?" In: *Phys. Rev. Lett.* 16 (1966), pp. 748–750 (cit. on p. 14).

[42] P. Hallen. "On the Measurement of High-Energy Tau Neutrinos with IceCube". MA thesis. der Rheinisch-Westfälischen Technischen Hochschule Aachen, 2013 (cit. on pp. 23, 27).

[43] *HDF5DotNet - C++/CLI Wrapper of the HDF5 Library*. `http://hdf5.net`. accessed: 2015-10-30 (cit. on p. 49).

[44] D. Hebecker et al. "Progress on the Development of a Wavelength-shifting Optical Module". In: 2015. arXiv: `1510.05228 [astro-ph.IM]` (cit. on p. 38).

[45] M. Honda et al. "Improvement of low energy atmospheric neutrino flux calculation using the JAM nuclear interaction model". In: *Phys. Rev.* D83 (2011), p. 123001. arXiv: `1102.2688 [astro-ph.HE]` (cit. on p. 17).

[46] K. Hoshina. private communication. 2015 (cit. on p. 50).

[47] *IceCube Wiki: Ice shear measurement*. `https://wiki.icecube.wisc.edu/index.php/Ice_shear_measurement`. Accessed: 2015-10-25 (cit. on p. 30).

[48] *IceCube Wiki: Muon tomography*. https://wiki.icecube.wisc.edu/index.php/Muon_tomography. Accessed: 2015-10-15 (cit. on p. 31).
[49] *IceCube Wiki: Stage 2 geometry*. https://wiki.icecube.wisc.edu/index.php/Stage_2_Geometry. Accessed: 2015-10-15 (cit. on p. 31).
[50] *A dual-PMT optical module (D-Egg) for IceCube-Gen2*. 2015. arXiv: 1510.05228 [astro-ph.IM] (cit. on p. 38).
[51] *Internal documentation*. https://wiki.icecube.wisc.edu/index.php/Ice_models. Accessed: 2015-08-15 (cit. on p. 29).
[52] J. Kapustinsky et al. "A fast timing light pulser for scintillation detectors". In: *Nuclear Instruments and Methods* A241.2–3 (1985), pp. 612–613 (cit. on p. 40).
[53] A. Karle. "DOM subsystems: Harness and Penetrator assembl". In: Presented at the Integrated DOM Design Review, Lawrence Berkeley National Laboratory, May 2004 (cit. on p. 51).
[54] S. F. King and C. Luhn. "Neutrino Mass and Mixing with Discrete Symmetry". In: *Rept. Prog. Phys.* 76 (2013), p. 056201. arXiv: 1301.1340 [hep-ph] (cit. on p. 4).
[55] C. Kopper. *CLsim*. http://code.icecube.wisc.edu/projects/icecube/browser/IceCube/projects/clsim. Accessed: 2015-07-30 (cit. on p. 53).
[56] K. Krings et al. "A Precision Optical Calibration Module for IceCube-Gen2". In: 2015. arXiv: 1510.05228 [astro-ph.IM] (cit. on p. 54).
[57] K. Krings. "Studies on the Measurement of Atmospheric Neutrino Oscillations with the PINGU Detector." MA thesis. Rheinisch Westfälische Technischen Hochschule Aachen, 2013 (cit. on pp. 8, 19, 36).
[58] "Letter of Intent: The Precision IceCube Next Generation Upgrade". 2015 (cit. on pp. 28, 30, 36–40).
[59] E. Ma, A. Natale, and A. Rashed. "Scotogenic $A_4$ Neutrino Model for Nonzero $\theta_{13}$ and Large $\delta_{CP}$". In: *Int. J. Mod. Phys.* A27 (2012), p. 1250134. arXiv: 1206.1570 [hep-ph] (cit. on p. 5).
[60] E. Majorana. "Teoria simmetrica dell elettrone e del positrone". In: *Il Nuovo Cimento* 14.4 (1937), pp. 171–184 (cit. on p. 4).
[61] K. M. Merfeld and D. C. Latimer. "Parametric enhancement of flavor oscillation in a three-neutrino framework". In: *Phys. Rev.* C90.6 (2014), p. 065502. arXiv: 1412.2728 [hep-ph] (cit. on pp. 10, 18).
[62] R. N. Mohapatra and J. W. F. Valle. "Neutrino Mass and Baryon Number Nonconservation in Superstring Models". In: *Phys. Rev.* D34 (1986), p. 1642 (cit. on p. 5).
[63] K. A. Olive et al. "Review of Particle Physics". In: *Chin. Phys.* C38 (2014), p. 090001 (cit. on pp. 3 sq., 14 sq., 22, 26).
[64] E. Peinado and A. Vicente. "Neutrino Masses from R-Parity Violation with a $Z_3$ Symmetry". In: *Phys. Rev.* D86 (2012), p. 093024. arXiv: 1207.6641 [hep-ph] (cit. on p. 5).

[65] F. Ritter et al.
"The calibration system of the GERDA muon veto Cherenkov detector".
In: *Nucl. Instrum. Meth.* A617 (2010), pp. 420–421 (cit. on p. 45).

[66] M. D. Serio. "Observation of $\nu\mu \to \nu\tau$ oscillations in the CNGS beam with the OPERA experiment". In: *EPJ Web Conf.* 95 (2015), p. 03005 (cit. on p. 5).

[67] *SPICE3 ice model presentation*.
`https://docushare.icecube.wisc.edu/dsweb/Get/Document-69693/ice.ppt`. Accessed: 2015-12-01 (cit. on p. 29).

[68] *Standard Model wikipedia page*.
`https://en.wikipedia.org/wiki/Standard_Model`.
Accessed: 2015-11-01 (cit. on p. 4).

[69] *Technical Guide*. Tech. rep.
231 Shaker Street, North Sutton, NH 03260 USA: Labsphere
(cit. on pp. 47 sq., 52).

[70] *The OpenCL Specification*. 2.0. Khronos OpenCL Working Group. July 2015
(cit. on p. 53).

[71] T. Waldenmaier. "IceTop - Cosmic Ray Physics with IceCube".
In: *Nucl. Instrum. Meth.* A588 (2008), pp. 130–134.
arXiv: `0802.2540 [astro-ph]` (cit. on pp. 13, 24).

[72] M. Wallraff. *nuCraft*. `http://nucraft.hepforge.org/`.
Accessed: 2015-06-01. 2013 (cit. on p. 19).

[73] C. Wiebusch. "Physics Capabilities of the IceCube DeepCore Detector".
In: (2009). arXiv: `0907.2263 [astro-ph.IM]` (cit. on p. 23).

[74] *Zenith Polymer Diffuse Reflectance Standards, Targets and Materials*.
SphereOptics. 2015 (cit. on pp. 46, 51 sq.).

# *Acknowledgements*

I would like to thank everyone who supported me during the production of this thesis.

Foremost, I thank Elisa Resconi for giving me the opportunity to work in her well functioning and very enjoyable group. Furthermore, I would like to express my thanks for giving me the opportunity to visit several conferences around the world, where I had the opportunity to present my work and associate with fellow physicists.

I express my gratitude to Patrick Decowski for the always valuable feedback, the general support and long-distance, but accurate supervision.

I would like to thank Kai Krings for sharing his expertise, valuable feedback and general patience as my daily supervisor.

My residence in Munich and research at the Technische Universität München was partially support by the $DuitslandInstituutAmsterdam$, for which I would like to express my gratitude.

To conclude, I would like to thank Stefan Coenders, Matthias Huber, Kai Krings and Andrea Turcati for providing me with valuable feedback on my writing, all the needed coffee brakes and Kicker Matches.